SAPIENZA
UNIVERSITÀ DI ROMA

Design and Optimization of Radio-Frequency Pulse Compressor Systems for High Brightness Linacs

Università degli studi di Roma - La Sapienza

Dottorato di Ricerca in Fisica degli Accelerator – XXXIII Ciclo

Candidate

LEVAN KANKADZE

ID number 1827945

Thesis Advisor

Dr. Massimo Ferrario

Co-Advisor

Dr. David Alesini

2021

Thesis defended on 30 June 2021
in front of a Board of Examiners composed by:

Prof. Pasquale Arpaia (chairman)

Prof. James Rosenzweig

Prof. Giovanni Mettivier

Design and Optimization of Radio-Frequency Pulse Compressor Systems for High Brightness Linacs
Ph.D. thesis. Sapienza – University of Rome

This thesis has been typeset by LaTeX and the Sapthesis class.

Author's email: kankadze.1827945@studenti.uniroma1.it

Dedicated to
my family

Abstract

Linac driven free electron lasers (FELs) are useful devices for studying matter and the demand for new FEL facilities is increasing constantly. The main issues of such machines are the size and the costs. Active research is going to improve the performance of the devices, reduce building and operational costs, and make them more compact.

In this framework, the INFN project EURPRAXIA@SPARC_LAB, is a proposal to upgrade the SPARC_LAB test facility (at LNF, Frascati) to a soft X-ray user facility based on plasma acceleration and high-gradient X-band accelerating structures [71]. Also the European project CompactLight-XLS [57] aims to design a compactFEL for users, in the hard X-ray range using the X band technology with a new C-band high-brightness photoinjector and innovative short-period undulators.

The X band module layout is composed by one klystron feeding, in parallel, four X band accelerating structures through a pulse compressor. This thesis work is focused on the design of this last device. We have performed both the rf and thermo-mechanical design. For the realization of this device we have proposed to use the innovative brazing-free technology developed at LNF-INFN and based on the use of special gaskets with a strong reduction of the cost, realization time and risk of failure due to the brazing process itself.

In chapter 1, traveling wave structures are briefly introduced with their main parameters.

In chapter 2, the EURPRAXIA@SPARC_LAB and CompactLight-XLS projects are briefly described with their applications, goals, and main components.

In chapter 3, the use of the RF pulse compressor systems in LINAC is illustrated and the different adopted solutions are briefly summarized with particular details on the Barrel Open Cavity (BOC) solution.

In chapter 4, the advantages of the new brazeless technology recently developed at LNF-INFN, for the realization of rf guns are briefly summarized and the opportunities to fabricate BOC pulse compressors systems with this new approach are put in evidence.

Chapter 5, is the core chapter of the thesis in which I describe the work done to completely design the BOC cavity for the EURPRAXIA@SPARC_LAB X band LINAC. The work flow involves the following main steps:

- Analytical and numerical analysis and design of the BOC
- Electromagnetic design and simulations
- Sensitivity study to evaluate the tolerable mechanical errors and possible tuning
- Thermo-mechanical analysis and design of the cooling system.
- Final mechanical design of the structure

Chapter 6 is focused on the application of pulse compressors to feed standing wave structures such as RF guns. A brief introduction on RF-guns and it's common feeding scheme is reported. An alternative feeding scheme for the C-band gun

proposed for the CompactLight-XLS project has been proposed. The scheme foresees the use of a BOC pulse compressor and avoids the use of a circulator (or isolator). Parameters of the pulse compressor has been optimized, to reach desired gun's cathode peak field and it's optimal performance. The electromagnetic design of the C band BOC is then illustrated.

The conclusions and perspectives are reported in the last chapter 7.

Acknowledgments

First I would like to thank Dr. David Alesini, for suggesting this particular topic to work on. His constant guidance and advice helped me a lot. David has made me realise that anything is attainable with hard work. Without his support, this thesis would not be possible.

Thanks to Dr. Andrea Ghigo and Dr. Alessandro Gallo for their hospitality. They provided a conducive work space and equipment for me to write my thesis.

Thanks to Dr. Fabio Cardelli for teaching me the basics of ANSYS. I want to thank Gianluca Di Raddo for helping with the mechanical drawings and Marco diomede for his help with effective shunt impedance calculations. Thanks to Dr. Mikhail Zobov for letting me use his PC for simulations. Thanks to Oscar and Andrea for sharing a room with me. Many others have not been mentioned by name as there are too many to thank. Your support was greatly appreciated. Thank you.

Thanks to Dr. Maria Rita Ferrazza and Daniela Napoleoni for teaching me Italian, to overcome obstacles in a foreign country and for making my life much easier.

I would like to show my gratitude to the International Charity Foundation Cartu for granting me the scholarship.

Finally, I would like to thank my family for their constant support, especially to my girlfriend, Cait Manners-Wood for tolerating my exceptional grumpiness during this most stressful writing process.

Contents

List of Figures

List of Tables

Chapter 1

Introduction

This thesis describes the development of the X-band BOC type rf pulse compressor with the innovative brazeless technology developed at LNF-INFN, for the LINACs of the EuPRAXIA@SPARC_LAB and XLS Compact Light projects.

Accelerators play important role in science, industry, and medicine [37]. Particle accelerators can be divided into two main classes: linear and circular.

In the circular accelerator, charged particles move on closed orbit, so accelerating cavities can be used over and over until the desired energy is not reached. Due to the curvature of the particle's trajectory, light particles (as electrons) radiate synchrotron radiation, which makes it increasingly harder to accelerate electrons to extremely higher energies [122].

A linear accelerator (linac) is a device that generates and accelerates charged particles in a straight line. The main advantage of the linear accelerator is its capability to produce high-energy, high-intensity charged particle beams of excellent quality in terms of beam emittance and energy spread [138].

Particles are accelerated with constant or time-varying electric fields. In the last case, there are two types of linacs: radio frequency (rf) and induction. In particular, in rf linacs, the particle acceleration is obtained by electromagnetic (EM) fields confined in resonant cavities fed by periodically time-varying power sources.

In research field, rf electron linacs are mainly used as injectors for synchrotrons and storage rings (SPring-8 at RIKEN [19, 129], APS at Argonne National Laboratory [1, 124], PETRA III at DESY [16, 41], ESRF [10, 81], CHESS at Cornell University [3, 43]), free electron lasers (LCLS at SLAC [15, 39], European XFEL [23, 28], PAL-XFEL at Pohang University of Science and Technology [17, 91], SACLA at RIKEN [140, 148], SwissFEL at PSI [106, 141]) and $+e/-e$ colliders (SuperKEKB at KEK [20, 111], BEPC II at Institute of High Energy Physics, Chinese Academy of Sciences [2, 25], VEPP-4M at BINP [66, 90], DAΦNE at LNF-INFN [8, 104]).

In an rf linear accelerator for electrons, particles are generated and pre-accelerated in the injector, of which main components are the gun, that generates electrons by thermionic [128] or photoelectric [115, 116] effects, followed by accelerating structures and magnetic elements (most often solenoids) used to bunch and increase the beam energy, keeping under control the transverse beam dynamics in terms of emittance increase [69]. The injector is typically followed by the main linac, made up of several accelerating sections that accelerate the beam up to the desired energy, interleaved

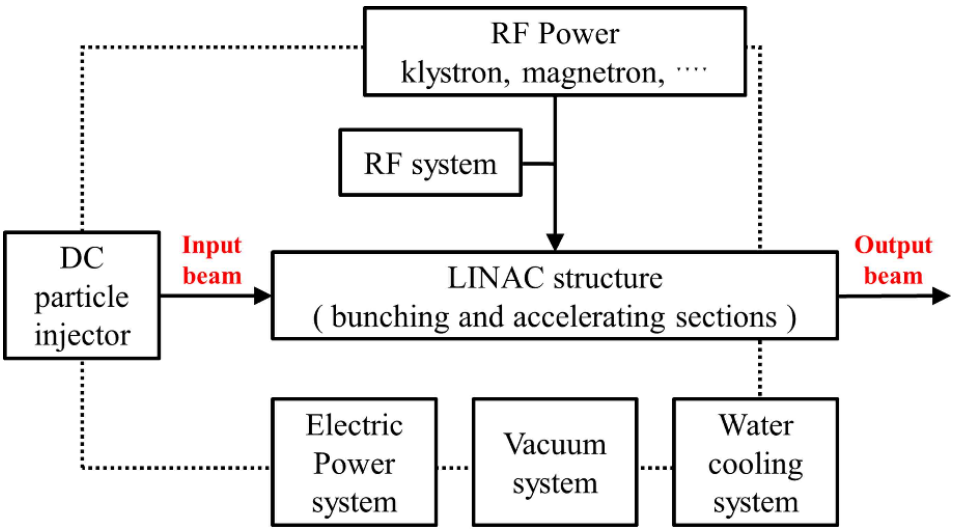

Figure 1.1. Simplified block diagram of a linac [125].

by magnetic elements, usually quadrupoles, which focus the beam. Beam trajectories and beam dimensions along the linac are measured by different types of diagnostic devices such as striplines or cavity beam position monitors or beam screens [92]. Control, cooling, vacuum, rf distribution, and power systems complete the basic scheme of a linear accelerator. A simplified block diagram of a linac is shown in Fig.1.1[125].

A strong impact on the size of an rf linac (especially in the case of high-energy linacs) is the frequency band of the accelerating sections. The higher is the operational frequency, the higher is the maximum accelerating gradient that can be sustained in the sections. The frequency dependence of rf breakdown level observed at low frequency continues to higher frequencies [147]. In user facilities S-band has been successfully adapted for guns [64, 120]. For the accelerating sections, the largest part of the facilities are based on S-band [24, 74, 82, 142], while the C-band has been successfully adopted for facilities like SACLA [86] and SwissFEL [151]. Through the years, the X-band frequency range (12 GHz) has been widely studied (see the following Section) especially in the framework of the linear collider proposals(CLIC [50], NLC/JLC [117]) but, up to now, there are no user facilities based on it [27].

My thesis work has been oriented to:

1) the rf and thermo-mechanical design and optimization of a rf pulse compressor in X-band for two different projects, EuPRAXIA@SPARC_LAB [71] and CompactLight-XLS [57], whose main goal, is the design of a compact FEL facility. Starting from the parameters of the proposed X-band accelerating structures [27], the BOC-type pulse compressor has been designed. For its realization the brazeless technology, recently successfully implemented at INFN-LNF [31], has been considered.

2) the rf design of a C band BOC-type pulse compressor system to feed the C band gun of the CompactLight-XLS Project. Starting from the C band gun a possible feeding scheme using a BOC has been proposed, optimized and designed. This scheme can be a possible alternative scheme for the feeding of Standing Wave

structures that foresees circulators or isolators.

Chapter 2

Traveling wave structures for electron linacs

A traveling wave (TW) accelerating structures are used to accelerate electrons. TW structures are disc loaded circular waveguides in which the propagating field is a TM_{01}-like mode with a phase velocity equal to the speed of light. The distance between the irises defines the phase advance per cell.

2.1 Main design parameters

The shunt impedance per unit length r is the parameter that quantify the rf efficiency of an accelerating cell. It is defined as [105]:

$$r = -\frac{E_z^2}{dP(z)/dz} = \frac{E_{acc}^2}{p_{diss}} \tag{2.1}$$

where E is the electric field amplitude, dP/dz is the rf power loss per unit length, E_{acc} is the average axial accelerating field and p_{diss} is the average dissipated power per unit length. It is defined as follows:

$$p_{diss} = \frac{P_{diss}}{d} \tag{2.2}$$

The quality factor (Q-factor) is defined as follows:

$$Q = -2\pi f_{rf} \frac{\omega_c}{dP/dz} = \omega_{rf} \frac{\omega_c}{p_{diss}} \tag{2.3}$$

where ω_c is the stored energy per unit length and ω_{rf} is the angular frequency of the rf power.

Geometrical parameter ρ is defined as:

$$\rho = \frac{r}{Q} = \frac{E^2}{\omega_{rf}\omega_c} \tag{2.4}$$

The phase velocity v_{ph} of a wave is the velocity at which phase of the wave propagates in time. it is defined as follows:

$$v_{ph} = \frac{\omega}{k_z} \tag{2.5}$$

where k_z is the waveguide propagation constant along z.

The group velocity v_g is the velocity at which rf energy flows through the accelerator. It is defined as:

$$v_g = \frac{d\omega}{dk_z} \tag{2.6}$$

It depends on phase advance per cell, iris thickness, iris tip shape.

The filling time t_f is the time necessary for energy to propagate at the group velocity from the input to the output end of the structure. It is defined as follows:

$$t_f = \int_0^{L_s} \frac{dz}{v_g(z)} \tag{2.7}$$

L_s is the length of the structure where energy propagates.

To derive analytical solutions of the gradient distribution in the TW accelerating structure with an arbitrary variation of parameters over the structure length for steady state we can use energy conservation. From Eqs. 2.1 - 2.6 we obtain the energy conservation including wall losses and the interaction with the beam [99]:

$$\frac{dP}{dz} = -\frac{\omega W}{Q} - GI \tag{2.8}$$

Basic equations for energy flow and for stored energy are as follows:

$$P = W v_g \qquad W = \frac{G^2}{\omega \rho} \tag{2.9}$$

P is the power flow through the structure cross section, I is beam current, ω is angular frequency, W is stored energy per unit length, Q is quality factor, G loaded accelerating gradient.

$\alpha(z)$ the attenuation in nepers per unit length and it is defined as:

$$\alpha(z) = \frac{1}{2}\frac{\omega}{v_g(z)Q(z)} \tag{2.10}$$

If we substitute equations 2.9 into equation 2.8 we will have:

$$\frac{dG}{dz} = -G(z)\alpha'(z) - \beta(z) \tag{2.11}$$

where $\alpha'(z) = \frac{1}{2}\left(\frac{1}{v_g}\frac{dv_g}{dz} - \frac{1}{\rho}\frac{d\rho}{dz} + \frac{\omega}{v_g Q}\right)$ and $\beta(z) = I\frac{\omega\rho}{2v_g}$.

If $\beta = 0$ (negligible beam loading, unloaded gradient) the solution of the Eq.2.10 is:

$$G(z) = G_0 g(z) \tag{2.12}$$

With G_0 is the value for $z = 0$ and is defined as follows:

$$G_0 = \sqrt{\frac{\omega\rho(0)P(0)}{v_g(0)}} \tag{2.13}$$

$g(z)$ is the accelerating gradient profile

$$g(z) = e^{-\int_0^z \alpha'(z')dz'} = \sqrt{\frac{v_g(0)}{v_g(z)}\frac{\rho(z)}{\rho(0)}}e^{-\frac{1}{2}\int_0^z \frac{\omega}{v_g(z')Q(z')}dz'} \tag{2.14}$$

From Eqs. 2.13 and 2.14 we will get:

$$G(z) = G_0 e^{-\int_0^z \alpha(z')dz'} \tag{2.15}$$

with

$$G_z = \sqrt{\frac{\omega\rho(z)P(0)}{v_g(z)}} \tag{2.16}$$

If we neglect the terms dv_g/dz and dp/dz in the equation for α', we obtain $\alpha'(z) = \alpha(z)$. Thus, the variation of the amplitude of the electric field along the structure is given by:

$$dG/dz = -\alpha G \tag{2.17}$$

while the rf power flow is given by

$$dP/dz = -2\alpha P \tag{2.18}$$

if we integrate equations 2.17 and 2.18 we will have:

$$G(z) = G_0 e^{-\int_0^z \alpha(z')dz'} \tag{2.19}$$

and

$$P(z) = P_0 e^{-2\int_0^z \alpha(z')dz'} \tag{2.20}$$

where G_0 and P_0 are values of the electric field and power at the section input (z = 0).

The section attenuation τ_s is defined as follows:

$$\tau_s = \int_0^{L_s} \alpha(z)dz \tag{2.21}$$

If we put Eq.2.20 in Eq.2.21:

$$P_{diss} = P_0 - P_{L_s} = P_0(1 - e^{-2\tau_s}) \tag{2.22}$$

with

$$\frac{P_{L_s}}{P_0} = \frac{P_{out}}{P_{in}} = e^{-2\tau_s} \tag{2.23}$$

2.2 Constant gradient structures

In a constant gradient (CG) structure, the profile of the accelerating electric field along the structure is constant, on the contrary, in a constant impedance structure, the field decays exponentially with z. A constant gradient structure can be realized by varying the iris holes in the disks to smaller and smaller apertures along the section [143].

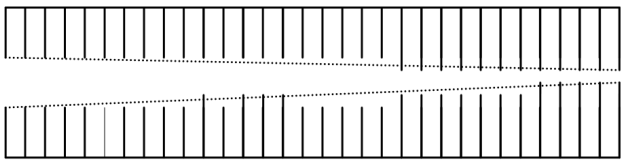

Figure 2.1. Sketch of the CG structure [22].

If we assume r and Q are constant along z we have that:

$$\alpha = \frac{1}{2}\frac{\omega}{v_g Q} \tag{2.24}$$

and

$$\tau_s = \alpha L_s = \frac{\omega L_s}{v_g Q} \tag{2.25}$$

From equation 2.1, to keep $G(z)$ constant, we must have:

$$dP/dz = const \tag{2.26}$$

The linear profile of $P(z)$ must be given:

$$P(z) = P_0 - (P_0 - P_{l_s})\frac{z}{L_s} = P_0\left(1 - \frac{z}{L_s}(1 - e^{-2\tau_s})\right) \tag{2.27}$$

Eq. 2.27 gives:

$$dP/dz = -P_0\left(1 - e^{-2\tau_s}\right) \tag{2.28}$$

Combining Eq. (2.27) with (2.28), (2.1) and (2.3), we will get:

$$v_g(z) = \frac{\omega L_s}{Q}\frac{1 - \frac{z}{L_s}(1 - e^{-2\tau_s})}{(1 - e^{-2\tau_s})} \tag{2.29}$$

From Eq.(2.7) we will have:

$$t_f = \frac{2Q\tau_s}{\omega} \tag{2.30}$$

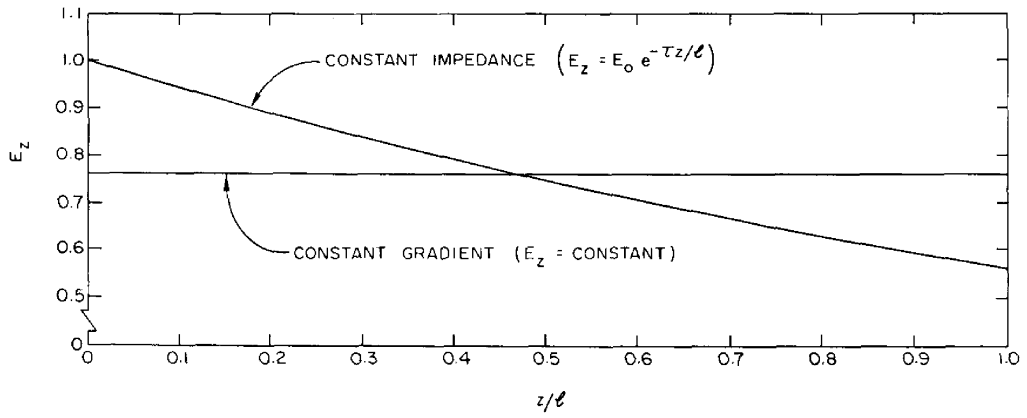

Figure 2.2. Shows electric field profile in constant impedance and constant gradient structures [94].

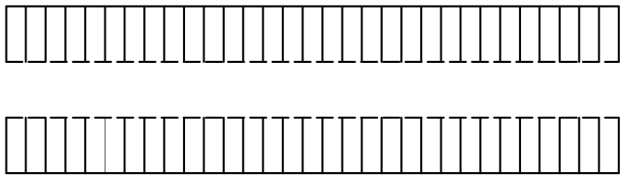

Figure 2.3. Sketch of the CI structure [22].

The axial fiedl strength can be obtained combining Eqs. (2.1) and (2.27):

$$G(z) = G_0 = \left(\frac{(1 - e^{-2\tau_s}) P_0 r_0}{L_s} \right)^{1/2} \tag{2.31}$$

Integrating above equation over the structure length will give:

$$V = G_0 L_s = \left((1 - e^{-2\tau_s}) P_0 r_0 L_s \right)^{1/2} \tag{2.32}$$

Comparing the energy gain of CI and CG structures as a function of the section attenuation, it can be observed that it is slightly higher for CG structures. An example is reported in Fig.2.2 [94].

2.3 Constant impedance structures

Constant impedance (CI) structures have all cells of the same dimensions, so the shunt impedance, group velocity and Q-factor are constant, Fig.2.3 [139].

Attenuation 2.10 in this case will be:

$$\alpha(z) = \frac{1}{2} \frac{\omega}{v_g Q} \tag{2.33}$$

Thus 2.18 will becomes:

$$dP/dz = -\frac{\omega P}{v_g Q} \tag{2.34}$$

With this conditions integration of equations 2.19 and 2.20:

$$G(z) = G_0 e^{-\frac{1}{2} \frac{\omega}{v_g Q} z} \tag{2.35}$$

and

$$P(z) = P_0 e^{-\frac{1}{2} \frac{\omega}{v_g Q} z} \tag{2.36}$$

After substituting Eq. 2.1 in Eq. 2.34 we have:

$$G_0 = \sqrt{r_0 \frac{\omega P}{v_g Q}} \tag{2.37}$$

The energy gained by an electron situated at phase ϕ with the respect to the crest of the traveling wave is:

$$W = eV = e\ cos\phi \int_0^{L_s} G(z)dz \tag{2.38}$$

where V is the voltage gain. For constant impedance structure it is equal to:

$$V = G_0 L_s((1 - e^{-\tau_s})/\tau_s)cos\phi = (2\tau_s)^{1/2}((1 - e^{-\tau_s})/\tau_s)(P_0 r_0 L_s)^{1/2} cos\phi \tag{2.39}$$

where

$$\tau_s = \alpha L_s = \frac{\omega L_s}{v_g Q} \tag{2.40}$$

is the total attenuation in nepers in the accelerating structure.

The condition for maximum energy gain is $\tau_s = \frac{1}{2}(e^{\tau_s} - 1)$, which is satisfied for $\tau_s = 1.26$. With this optimum value of τ_s, the maximum energy gain is $V_{max} \approx 0.903(P_0 r_0 L_s)^{1/2} \cos\phi$.

From Eq. (2.21), the filling time can be written as:

$$t_f = \frac{L_s}{v_g} = \frac{2Q\tau_s}{\omega} \tag{2.41}$$

For an accelerator optimized for the maximum energy gain, $\tau_f \approx 2.52Q/\omega$ [27].

Chapter 3

EuPRAXIA@SPARC_LAB & CompactLight-XLS Projects

3.1 EuPRAXIA@SPARC_LAB

EuPRAXIA@SPARC_LAB [71], is the proposal for the upgrade of the SPARC_LAB test facility [26] at INFN-LNF (Frascati, Italy). The goal is to design and build a new multi-disciplinary user-facility, equipped with a soft X-ray Free Electron Laser (FEL) driven by a ∼1 GeV high brightness linac based on plasma accelerator modules. EuPRAXIA@SPARC_LAB study is performed in synergy with the Horizon 2020 Design Study EuPRAXIA (European Plasma Research Accelerator with eXcellence In Applications) [136] [11] which goal is to demonstrate exploitation of plasma accelerators for users. The EuPRAXIA@SPARC_LAB project is intended to put forward the Laboratori Nazionali di Frascati (LNF) in Italy as host of the EuPRAXIA European Facility. which goal is to demonstrate the exploitation of plasma accelerators for users.

The EuPRAXIA@SPARC_LAB facility by itself will equip LNF with a unique combination of a high brightness GeV-range electron beam generated in a state-of-the-art linac, and a 0.5 PW-class laser system. Even in the case of LNF not being selected and/or of a failure of plasma acceleration technology, the infrastructure will be of top-class quality, user-oriented, and at the forefront of new acceleration technologies.

The new facility will cover approximately an area of 4000 m^2. The layout of the EuPRAXIA@SPARC_LAB infrastructure is schematically shown in Figure 3.1. From left to right one can see a 55 m long tunnel hosting a high brightness 150 MeV S-band RF photoinjector equipped with a hybrid compressor scheme based on both velocity bunching [70, 77, 123] and magnetic chicane. The energy boost from 150 MeV up to a maximum 1 GeV will be provided by a chain of high gradient X-band RF cavities [60, 131]. At the linac exit, a 5 m long plasma accelerator section will be installed, which includes the plasma module (∼0.5 m long) and the required matching [47, 52] and diagnostics sections [53, 103]. In the downstream tunnel, a 40 m long undulator hall is shown, where the undulator chain will be installed [114]. Further downstream after a 12 m long photon diagnostic section [135] the users hall is shown [42]. Additional radiation sources as THz and γ-ray Compton

Figure 3.1. The layout of the EuPRAXIA@SPARC_LAB infrastructure

sources are foreseen in the other shown beam lines. The upper room is dedicated to Klystrons and Modulators. In the lower light-blue room will be installed the existing 300 TW FLAME laser [44] eventually upgraded up to 500 TW. The plasma accelerator module can be driven in this layout either by an electron bunch driver (PWFA scheme) [102] or by the FLAME laser itself (LWFA scheme) [119].

The experimental activity will be initially focused on the realization of a plasma driven short wavelength FEL with one user beam line, according to the beam parameter reported in the Table 3.1. This goal is already quite challenging but it is affordable by the EuPRAXIA@SPARC_LAB collaboration and will provide an interesting FEL radiation spectrum in the so-called "water window". The first foreseen FEL operational mode is based on the Self Amplification of Spontaneous Radiation (SASE) mechanism [45] with tapered undulators. More advanced schemes like Seeded and Higher Harmonic Generation configurations will be also investigated. The user's end station, called EX-TRIM (Eupraxia X-ray Time Resolved coherent IMaging), will be designed and built to allow performing a wide class of experiments using the schematic apparatus discussed in [42, 52]. As a specific example of EuPRAXIA@SPARC_LAB applications, it is worth remarking that the FEL radiation in the soft X-ray spectrum opens possibilities for novel imaging methodologies and time-resolved studies in material science, biology and medicine, along with non-linear optics applications.

3.1.1 Layout and main parameters of the linac

Electron beam acceleration schematic is shown in fig. 3.2 [130] The EuPRAXIA@SPARC_LAB accelerator is about 50 meters. the electron beam is generated in a twelve meters long high brightness SPARC-like S-band photoinjector described in [30]: 1.6 cell S-band rf gun where a Cu photocathode is mounted and driven by a 50 μJ Ti:Sapphire laser with a four coils solenoid for the emittance compensation; three TW SLAC type S-band linac sections follow for a final energy ranging between $W = 100$–230 MeV depending on the applied rf compression factor as described in [30], [78]. The downstream X-band rf linac can increase the electron beam energy up to $W_{max} \approx 1$

Table 3.1. EuPRAXIA@SPARC_LAB's beam parameters for plasma and conventional rf linac driven FEL [71], [27].

Parameter	Units	Full rf	LWFA	PWFA
Electron Energy	GeV	1	1	1
Repetition Rate	Hz	10	10	10
RMS Energy Spread	%	0.05	2.3	1.1
Peak Current	kA	1.79	2.26	2.0
Bunch Charge	pC	200	30	200(D)-30(W)
RMS Bunch Length	μm (fs)	16.7 (55.6)	2.14 (7.1)	3.82 (12.7)
RMS Normalized Emittance	mm mrad	0.5	0.47	1.1
Slice Length	μm	1.66	0.5	1.2
Slice Charge	pC	6.67	18.7	8
Slice Energy Spread	%	0.02	0.015	0.034
Slice Normalized Emittance (x/y)	mm mrad	0.35/0.24	0.45/0.465	0.57/0.615
Undulator Period	mm	15	15	15
Undulator Strength $K(a_w)$		0.978 (0.7)	1.13 (0.8)	1.13 (0.8)
Undulator Length	m	30	30	30
ρ (1D/3D)	$\times 10^{-3}$	1.55/1.38	2/1.68	2.5/1.8
Radiation wavelength	nm (KeV)	2.87 (0.43)	2.8 (0.44)	2.98 (0.42)
Photon Energy	μJ	177	40	6.5
Photons per Pulse	$\times 10^{10}$	255	43	10
Photon Bandwidth	%	0.46	0.4	0.9
Photon RMS Transverse Size	μm	200	145	10
Photon Brilliance per shot	(s mm^2 mrad^2 bw(0.1%))$^{-1}$	1.4 $\times 10^{27}$	1.7 $\times 10^{27}$	0.8 $\times 10^{27}$

GeV; at the X-band linac exit, a Plasma Acceleration Structure (PLAS) is foreseen and after this two separate transfer lines deliver the electron beam to the Undulator and to the Compton Interaction point respectively. A four dipole magnetic chicane, 10 m long, is inserted in the X-band linac between the two sections Linac1 (L_1) and Linac2 (L_2), for longitudinal compression and phase space manipulation of the electron beam. In order to satisfy the requirements of the SASE FEL radiation source foreseen in the EuPRAXIA@SPARC_LAB project a FWHM bunch current of 2–3 kA must be delivered to the entrance of the undulator at the energy of 1 GeV, with a very good emittance in the 6D phase space. The 1 GeV energy can be achieved by means of a single stage of plasma acceleration, a few centimeters long, coupled with the rf linac operating at 500 MeV (PWFA and LWFA cases of Table 3.1), or with the conventional operation of the Linac at twice the accelerating gradient in the X-band sections (Full rf case). The goal of the project is to operate plasma acceleration at approximately 10^{16} cm^{-3}, a plasma density that can be used to produce electric fields of 1–2 GV/m and characterized by a plasma wavelength of $\lambda_p \approx 300$ μm that allows for realistic bunch separation with the use of a COMB technique [78], [51]. Such accelerating gradients are tailored for specific envisioned experiment [101], [118] where the foreseen parameters will allow for good beam loading compensation and lower quality depletion. This matches with the chosen plasma input energy of 500 MeV, highly rigid bunch, that limits transverse bunch evolution and the consequent transverse emittance dilution within the plasma.

The baseline chosen technology for the EuPRAXIA@SPARC_LAB booster is X-band. The X-band booster design has been driven by the need of a high accelerating

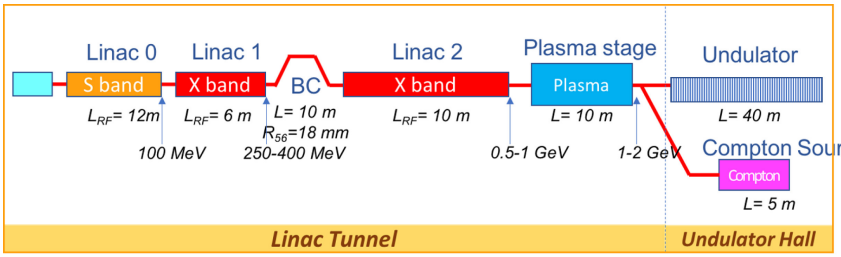

Figure 3.2. Shows EuPraxia@SPARC_LAB electrom beam acceleration layout [130].

Table 3.2. Main parameters of CPI VKX-8311A klystron.

Parameter	**Value**
Beam Voltage	410 kV
Beam Current	310 A
Frequency	11.994 GHz
peak Power	50 MW
Average Power	5 kW
Sat. Gain	48 dB
Efficiency	40 %
Duty	0.009 %

gradient required to achieve a high facility compactness, which is one of the main goals of the EuPRAXIA project. The total space allocated for the linac accelerating sections is $\sim$ 25 m, corresponding to an active length L_t of $\sim$16 m taking into account the space required to accommodate beam diagnostics, magnetic elements, vacuum equipment and flanges. The average accelerating gradient for the X-band linac is 60 MV/m The rf linac layout is based on klystrons with BOCs that feed four TW accelerating structures in parallel. The operating mode of the TW structures is the $2\pi/3$ mode at 11.9942 GHz. The rf power source is the CPI VKX-8311A klystron [14]. The main klystron parameters are summarized in Table 3.2.

The Full rf linac configuration is meant to provide a 200 pC electron beam able to drive SASE-FEL radiation and/or Compton interaction with the laser pulse. The high charge electron beam coming from the photoinjector is accelerated with the linac and the final longitudinal compression for the SASE-FEL operation occurs in the magnetic chicane, located between L1 and L2 linac sections, according to a hybrid scheme of longitudinal compression: velocity bunching in the photoinjector plus magnetic compression in the linac. The X-band linac mainly consists of two sections, L_1 and L_2, located before and after the magnetic chicane respectively. The maximum accelerating gradient applied is G = 60 MV/m through all L_1 and L_2, to reach the required energy and energy spread for the electron beam in the conventional rf operation scheme. Between L_1 and L_2, a 10 m long magnetic chicane is foreseen for phase space manipulation and/or longitudinal compression of the bunch; at the same time when the chicane dipoles are switched off, the straight beamline accommodates the middle energy diagnostic station for beam parameters measurement. The two linac sections L_1 and L_2 have been optimized to provide the required beam acceptance, from photo-injector and after the magnetic chicane, for

Table 3.3. EuPRAXIA@SPARC_LAB's main linac parameters.

Beam parameter	unit	L1			L2		
		PWFA	LWFA	Full rf	PWFA	LWFA	Full rf
Initial energy W_0	MeV	102	98	171	222	212	502
Final energy W_f	MeV	222	212	502	582	550	1052
Active Linac length	m		6.0			10.0	
Acc. Gradient <G>	MV/m	20.0	20.0	57.0	36.0	36.0	57.0
RF phase (0 crest)	deg	0	-20.0	-15.0	0	-19.5	+15.0
Initial energy spread	%	0.15	0.27	0.67	0.11	0.15	0.59
Final energy spread	%	0.11	0.15	0.59	0.07	0.07	0.14
Final bunch length σ_z	νm	6	5	112	7	5	16

Table 3.4. Main parameters of the EuPRAXIA@SPARC_LAB's X-band linac.

Parameter	**Units**	**Value**
Frequency	GHz	11.9942
Average gradient	MV/mm	60
Structure per module		4
Iris radius a	mm	3.8 - 3.2
Tapering angle	deg	0.04
Structure length L_s	m	0.9
Number of cells		109
Shunt impedance r	MΩ	94-107
Filling time t_f	ns	126
Klystron pulse length	μs	1.5
Klystron power	MeV	~ 50
Average iris radius	mm	3.5
Linac active length L_{act}	m	18
SLED Q_0		150000
SLED Q_e		18500
Peak modified poynting vector	W/μM^2	3.5

the considered working points.

3.1.2 Layout of the X band rf module

The X band RF module is made up of a group of 4 TW sections assembled on a single girder and fed by one klystron by means of one rf pulse compressor system and a low attenuation circular waveguide network that transports the rf power to the input hybrids of the sections Fig.3.3. The mechanical layout of the X band module is given in Fig.3.4. The main parameters of the X band structures are given in Table 3.4.

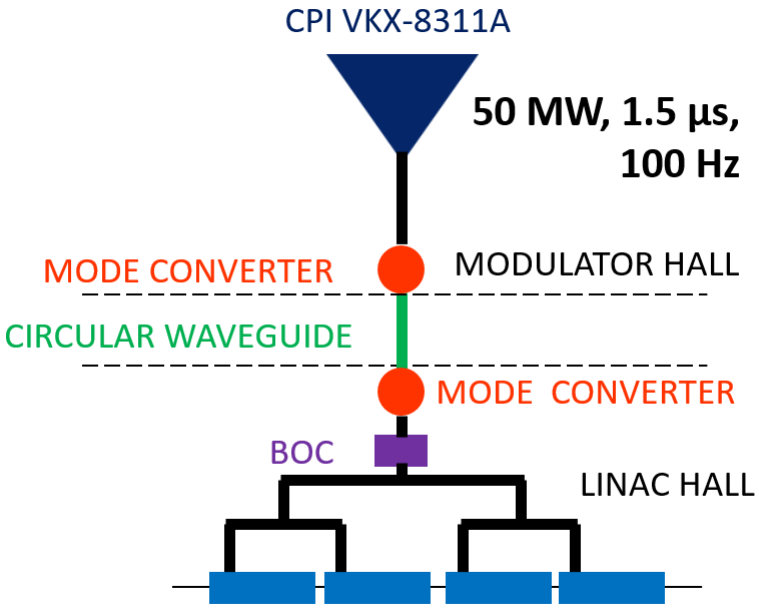

Figure 3.3. Sketch of the EuPRAXIA@SPARC_LAB's rf module.

3.2 CompactLight-XLS

CompactLight (XLS) is international Collaboration, funded by the European Union, including 24 partners and 5 Associated Countries, 1 international Organization and 2 Third Countries [57], [6]. The main goal of the collaboration is to facilitate the development of X-ray FEL facilities across Europe and beyond, by making them more affordable to construct and operate, through an optimum combination of emerging and innovative accelerator technologies. The three-year design study, funded in the framework of the Horizon 2020 Research and Innovation Programme 2014-2017, has been started in January 2018, and intends to design a hard X-ray FEL facility beyond the state of the art. Compared with existing facilities, the proposed facility will benefit from a lower electron beam energy, due to the enhanced undulator performance; be significantly more compact, as a consequence of the lower beam energy and the high gradient of the X-band structures; be more efficient (less power consumption), as a consequence of the lower energy and the use of high-frequency structures. These ambitious, but realistic aims, will make the design less expensive to build and operate when compared with the existing facilities, making X-ray FELs more affordable. Based on user-driven scientific requirements (i.e. wavelength range, beam structure, pulse duration, synchronisation to external laser, pulse energy, polarisation, etc.), the goal is to provide the design of an ideal X-band driven hard X-ray FEL, including, as well, options for soft X-ray operation.

The user requirements for CompactLight have been established interacting with existing and potential FEL users in a variety of formats. With regard to the tunability, there is a clear demand for photon energies as low as 0.2 keV and as high as 20 keV. The mean photon energy of the desired tunable range is about 4 keV. For

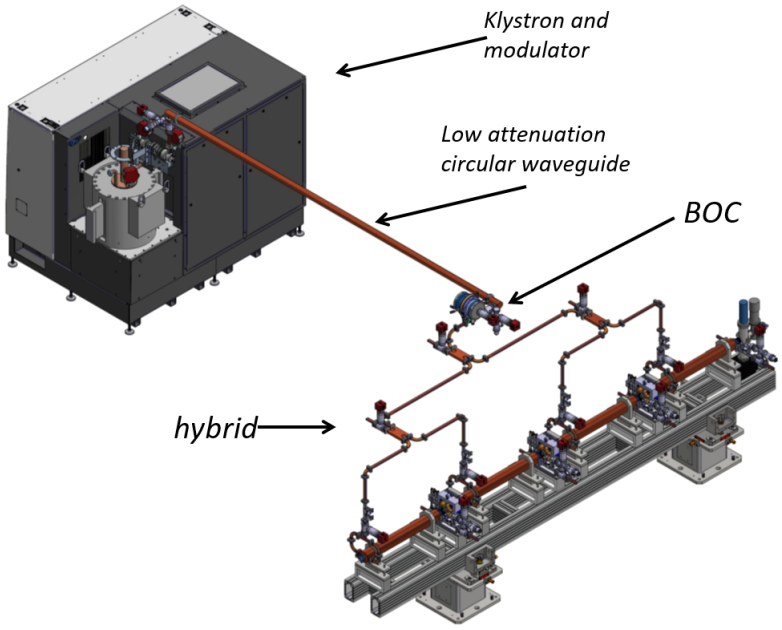

Figure 3.4. 3D model of the EuPRAXIA@SPARC_LAB's rf module.

Table 3.5. Main parameters of the CompactLight FEL. [57]

Parameter	Units	Soft X-ray	Hard X-ray
Photon energy	keV	0.25-2.0	2.0-16.0
Wavelength	mm	5.0-0.6	0.6-0.08
Repetition	Hz	1000	100
Pulse duration	fs	0.1-50	0.1-50
Two-pulse delay	fs	±100	±100
Two-color separation	%	20	10
Laser-FEL synchronization	fs	<10	<10

pump-probe experiments, most respondents want the synchronization between the FEL and the external laser to be in the order of 10 fs [100]. The photon output specification are summarized in Table 3.5.

3.2.1 Layout and main parameters of the linac

A preliminary layout of the CompactLight facility is shown in Fig. 3.5. Conventionally, only one fundamental resonance wavelength exists in the FEL because of the simple linear structure of the undulator. By operating the FEL using a two-section undulator each with different deflection parameters, K_1 and K_2, respectively, it is possible to achieve laser action at two different wavelengths simultaneously. This is the so-called two-colour mode [87]. A key request from the user community, which significantly affects the facility layout, is the requirement for large wavelength separation when operating in two-colour mode. This effectively means that two bunches must independently reach saturation in two different undulators. Normally,

it would be expected that this would happen in a very long undulator, tuned for two different wavelengths. However, it has been decided to operate in parallel (i.e. the two different wavelengths at the same time) rather than series (i.e. the two wavelength one after the other one), which means that there are two separated FEL lines. This has several additional advantages. First, the total undulator length is approximately the same and so the parallel option is more compact overall; second, the two independent wavelengths could be combined into a single experiment or, if that is not required, two experiments could take place at the same time, doubling the capacity of the facility. Furthermore, the two FEL lines are planned to operate

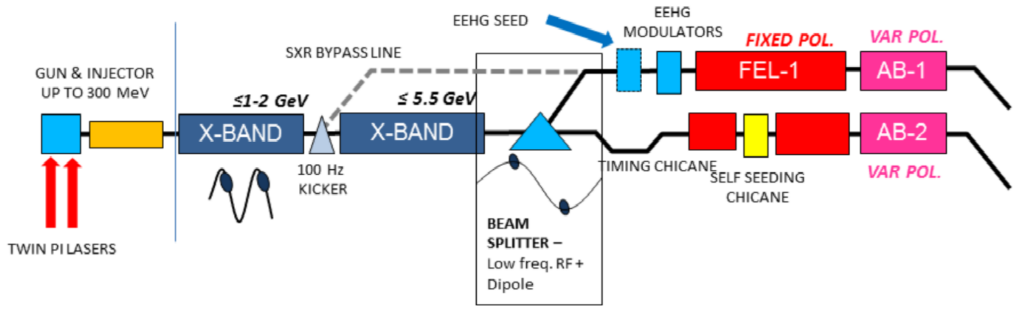

Figure 3.5. Shows the sketch of the entire CompactLight facility in a two-pulse, two-color scheme [57].

over the full wavelength range. When running in hard X-ray mode (named HXR) the electron energy will be up to 5.5 GeV at 100 Hz, in soft X-ray mode (named SXR) the energy will be up to 2 GeV and, since the linac gradient will be much reduced, the repetition rate will be able to be increased significantly. A repetition rate of 1000 Hz for the soft-X-ray FEL would be a unique and highly desirable feature of the facility.

As shown in Fig. 3.5, the linac layout consists of an injection section, up to 300 MeV, with a high-brightness electron source and a laser heater, to mitigate the micro-bunching instability. A two-stage magnetic compression scheme (BC1 + BC2) is adopted. The first magnetic bunch compressor (BC1) is located at 300 MeV. Two X-band linacs (named Linac1, upstream the kicker, and Linac2, downstream the kicker, respectively), separated with a second bunch compressor (BC2) at an energy between 1 GeV and 2 GeV, will boost the beam energy up to 5.5 GeV. At the exit, the beam is steered to different undulators with a spreader. For the electron source, the baseline design is the full C-band injector For the main linac different options have been studied and the present design foresees the use of a double RF source system for a rep. rate operation from 100 Hz up to 1 kHz. The scheme of the accelerating module is given in Fig. 3.6 and the main parameters of the accelerating structures are given in Table 3.7. These parameters are similar to the EUPRAXIA@SPARC_LAB ones except for the fact that, for XLS, it is foreseen also a tapering of the irises thickness to reduce the long-range wakefield and allow the two bunch operation.

In Table 3.8, the main parameters of the X-band linac are reported. Like EuPRAXIA@SPARC_LAB, the CPI VKX-8311A klystron has been chosen as the

Table 3.6. Main Electron Beam and FEL Parameters. [57]

Parameter	Value
Max energy	5.5 GeV@100 Hz
Peak current	5 kA
Normalised emittance	0.2 mm mrad
Bunch charge	<100 pC
RMS slice energy spread	10^{-4}
Max photon energy	16 keV
FEL energy tuning range at fixed energy	x2
Peak spectral brightness @16 keV	10^{33} ph/s/mm^2/$mrad^2$/0.1%bw

Table 3.7. Main Electron Beam and FEL Parameters. [57], [58]

Parameter	Units	Value
Frequency	GHz	11.994
Klystron pulse length	μs	1.5
Klystron power	MeV	$\sim$ 50
Average iris radius	mm	3.5
Iris radius a	mm	4.3 - 2.7
Iris thickness t	mm	2.0 - 2.4
Structure length L_s	m	0.9
SLED Q_0		180000
SLED Q_e		23200
Shunt impedance r	MΩ	90 - 125
Effective shunt impedance r_s	MΩ	378
Group velocity v_g/c	%	4.7 - 0.9
Filling time t_f	ns	146
Repetition rate [Hz]		100 250 1000
Pulse compressor		ON OFF ON
Net klystron power (w/loss)	MW	40 40 8
Avg. accelerating gradient	MV/m	65 30 30

Table 3.8. CompactLight's main linac parameters. [57]

Parameter	Units	Linac 1	Linac 2
Acc. Gradient	MV/m	65	65
Initial energy W_0	GeV	0.3	2
Final energy W_f	GeV	2	5.5
Energy gain W_{gain}	GeV	1.7	3.5
Active length	m	26.2	53.8

reference rf power source. The structures operate than at 11.9942 GHz with a phase advance per cell of $2\pi/3$. Also, in this case, SLED type (BOC or SLED) pulse compressor systems have been chosen as pulse compressors.

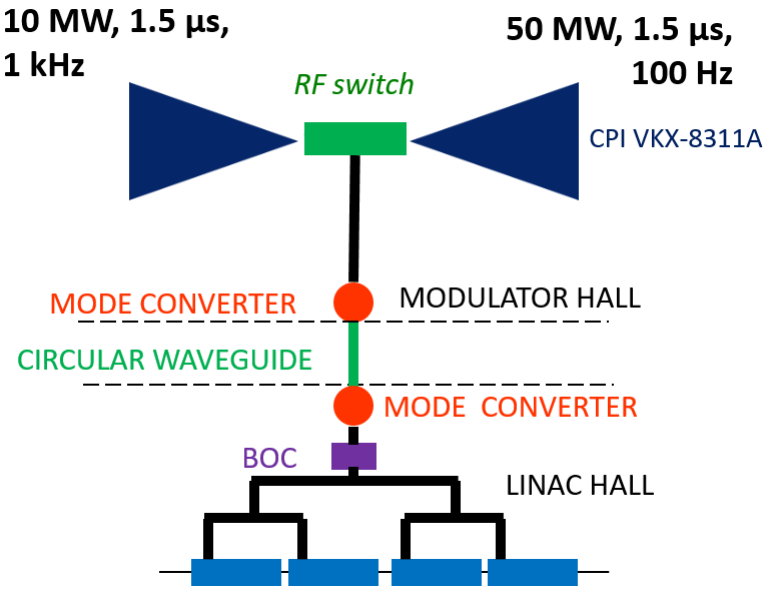

Figure 3.6. Sketch of the Compact-XLS rf module.

Chapter 4

RF pulse compressors

Rf pulse compressors are fundamental devices in linear accelerators, free electron lasers (FEL), and other large facilities that use normal-conducting, high-gradient TW accelerating structures [137]. Usually, power sources in linacs are klystrons. Normal-conducting accelerating structures are operated at low duty cycles ($< 10^{-4}$), a short ($\leq 1\mu$s) and high peak power (several tens MWs) rf pulses. An rf pulse compressor allows to compress relatively long rf pulses (few μs) of few tens of MW, generated by klystrons, to shorter ones with a higher peak power (hundreds of MWs).

Pulse compression can be achieved by either passive or active means [134]. Active compression usually provide higher power gains without much loss of efficiency. In the present thesis work we will focus on passive pulse compressors that do not contain elements with time-dependent electrodynamic parameters, but require fast phase modulation of the incident rf pulse. Passive pulse compressors were successfully implemented in several systems: the first and most common system was the SLED-I [67], followed by Barrel Open Cavity (BOC) [40], Binary Pulse Compression (BPC) [68], Super Compact Spherical Pulse compressor [96] and SLED-II [145]. Active compression makes it possible to achieve higher power gains while retaining high efficiency, as compared with passive compression. Active compression is based on the storage of energy in a high-Q microwave resonator and followed by the rapid increase of the coupling between the resonator and the load (Q switching) using the active element, a fast switch [134].

4.1 SLED - I

The SLED-I RF pulse compressor was invented at SLAC in 1973 [67], as a way to increase the performance of the accelerator in term of achievable electron energy. RF power from a klystron is stored in two high Q (Quality factor) cavities through a 3dB hybrid to avoid power reflection back to the klystron itself. Towards the end of the pulse, the cavities are emptied by reversing the phase of the input pulse from the klystron. Cavities are emptied in a shorter interval of time compared to the time in which cavities are filled. Due to the conservation of energy peak will be increased as the pulse is compressed in time.

To obtain an analytic description of the SLED mechanism, conservation of energy

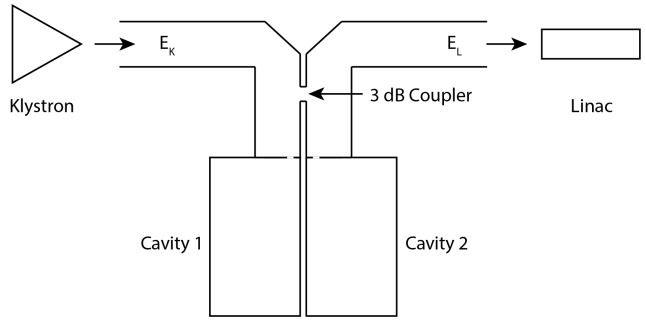

Figure 4.1. Shows a simplified schematic of a SLED-I pulse compressor.

is the most straight forward approach [109], [146]:

$$P_i = P_r + P_c + dW_c/dt \tag{4.1}$$

where P_i is the input power, P_r is the outgoing power from the cavities irises, P_c is the power dissipated in the cavities walls, W_c is the electromagnetic energy stored in the cavities at time t.

The stored energy in the cavity can be expressed in terms of the unloaded Q-factor Q_0, dissipated power P_c and angular frequency ω:

$$W_c = \frac{Q_0}{\omega} P_c \tag{4.2}$$

If V_c is the cavity field and R is the cavity shunt impedance we have that:

$$P_c = \frac{V_c^2}{R} \tag{4.3}$$

Let V_{in} be the voltage of the forward wave in transmission line with impedance Z then:

$$P_c = \frac{V_i^2}{Z} \tag{4.4}$$

Let V_{out} be the voltage of the forward wave in transmission line with impedance Z then:

$$P_c = \frac{V_r^2}{Z} \tag{4.5}$$

The backward wave V_r is equal to:

$$V_r = V_c - V_i \tag{4.6}$$

After we substitute equations 4.2 - 4.6 into 4.1, for V_c and V_i we will have:

$$\frac{V_i^2}{Z} = \frac{(V_c - V_i)^2}{Z} + \frac{V_c^2}{R} + 2\frac{Q_0 V_c}{\omega R}\frac{dV_c}{dt} \tag{4.7}$$

After simplifications:

$$2V_i = \left(1 + \frac{Z}{R}\right) V_c + 2\frac{Z}{R}\frac{Q_0}{\omega}\frac{dV_c}{dt} \tag{4.8}$$

The cavity coupling coefficient, can be defined as the ratio of power emitted from the coupling iris to that dissipated in the cavity walls:

$$\beta = \frac{P_r}{P_c} = \frac{Q_0}{Q_e} = \frac{R}{Z} \tag{4.9}$$

Therefore, equation 4.8 can be re-written as:

$$\frac{2\beta}{\beta+1}V_i = V_c + \frac{2Q_0}{\omega(\beta+1)}\frac{dV_c}{dt} \tag{4.10}$$

The definition of the loaded Q-factor Q_L is:

$$\frac{1}{Q_L} = \frac{1}{Q_0} + \frac{1}{Q_e} \tag{4.11}$$

Then from equation 4.9:

$$Q_l = \frac{Q_0}{1+\beta} \tag{4.12}$$

Introducing the new variables:

$$\alpha = \frac{2\beta}{1+\beta} \tag{4.13}$$

$$T_c = \frac{2Q_L}{\omega} = \frac{2Q_0}{(1+\beta)\omega} \tag{4.14}$$

Using equations 4.13 and 4.14, equation 4.10 can be rewritten as:

$$T_c\frac{dV_c}{dt} + V_c = \alpha V_i \tag{4.15}$$

This first-order nonhomogeneous differential equation 4.15 defines voltage in the cavity.

To simplify the calculation we can assume that input voltage is equal to:

$$V_i = \begin{cases} 1 & \text{if } 0 < t < t_f \\ -1 & \text{if } t_f \leqslant t \leqslant t_e \\ 0 & \text{if } t > t_e \end{cases} \tag{4.16}$$

t_f is time when pulse was flipped, t_e is the end of the pulse.

To find output compressed field, which is equal to $V_r = V_c - V_i$, we need to solve 4.15, with piece wise driven term 4.16 and with boundary conditions $E_e = 0$ when $t = 0$. Solution will be:

$$V_{out}(0 \leqslant t < t_f) = \alpha\left(1 - e^{-t/T_c}\right) - 1 \tag{4.17}$$

$$V_{out}(t_f \leqslant t \leqslant t_e) = \alpha[(2 - e^{-t_f/T_c})e^{-(t-t_f)/T_c} - 1] + 1 \tag{4.18}$$

$$V_{out}(t > t_e) = \alpha[(2 - e^{-t_f/T_c})e^{-(t_e-t_f)/T_c} - 1]e^{-(t-t_e)/T_c} \tag{4.19}$$

The waveforms of direct wave from the klystron V_1, emitted wave from the cavities V_{out}, as a function of time are shown in Fig.4.2.

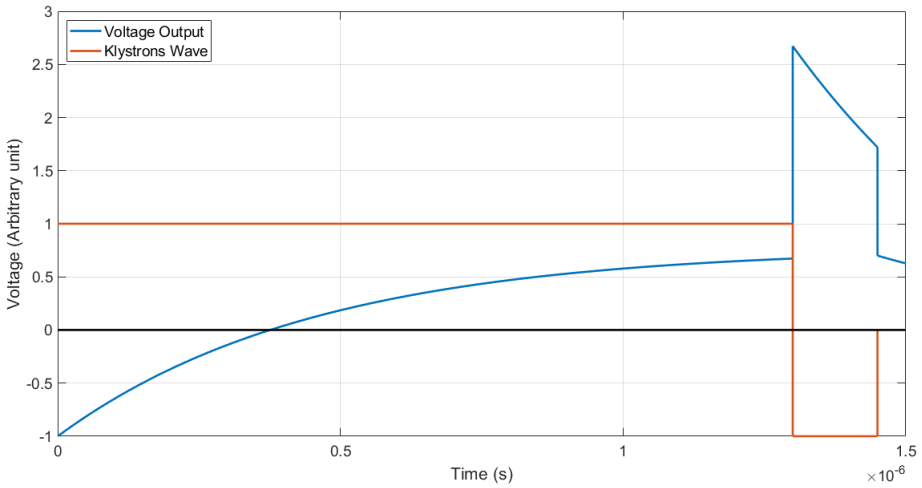

Figure 4.2. The output field from SLED and klystron input field

For a constant impedance TW structure, the maximum normalized energy gain, called energy multiplication factor M, is [49]:

$$M = \frac{V_{max}}{V_0} \tag{4.20}$$

where

$$V_{max} = (\alpha - 1)\frac{T_1}{T_a}\left(e^{-\frac{T_a}{T_1}} - 1\right) + \gamma\frac{T_2}{T_a}\left(e^{-\frac{T_a}{T_1}} - e^{-\frac{T_a}{T_c}}\right), \tag{4.21}$$

$$V_0 = \frac{T_1}{T_a}\left(1 - e^{-\frac{T_a}{T_1}}\right), \tag{4.22}$$

$$\gamma = \alpha(2 - e^{-\frac{t_f}{T_c}}) \tag{4.23}$$

$$\frac{1}{T_1} = \frac{\omega}{2Q}, \tag{4.24}$$

Q is the quality factor of the cells in the structure,

$$\frac{1}{T_2} = \frac{1}{T_c} - \frac{1}{T_1}, \tag{4.25}$$

$$T_a = \frac{L_s}{v_g} \tag{4.26}$$

is the filling time of the CI structure.

The multiplication factor for a constant gradient structure is given by the following formula [67]:

$$M = \gamma e^{-T_a/T_c}\frac{1 - (1-g)^{(1+\nu)}}{g(1+\nu)} - (\alpha - 1) \tag{4.27}$$

where

$$g = 1 - e^{-2t_s/T_c} \tag{4.28}$$

$$T_a = \frac{L_s}{g v_{g0}} ln\left(\frac{1}{1-g}\right) \tag{4.29}$$

is the filling time of the CG structure with v_{g0} the group velocity in the first accelerating cell and

$$\nu = T_a / \left(T_c ln(1-g)\right) \tag{4.30}$$

In both cases, the maximum energy gain is obtained for a compressed pulse length equal to the filling time of the structure.

4.2 Barrel Open Cavity

To achieve high Q quality factors spherical shapes are the most effective geometries, but spherical cavities suffer from the high number of competing resonant modes, problems of orientation, parasitic modes [72].

To overcome the above mentioned problems different schemes were developed. One of them is the Barrel Open Cavity (BOC), which initially was designed for a VLEPP project [40]. From that time much effort was made to improve performance and develop theory [56], some authors have proposed such compression schemes without coupling slots, but with mode launchers [85], [97].

The compression scheme using BOC was successfully realized at CERN in S-band [48]. More recently at SwissFEL in C-band [150] and at IHEP [126].

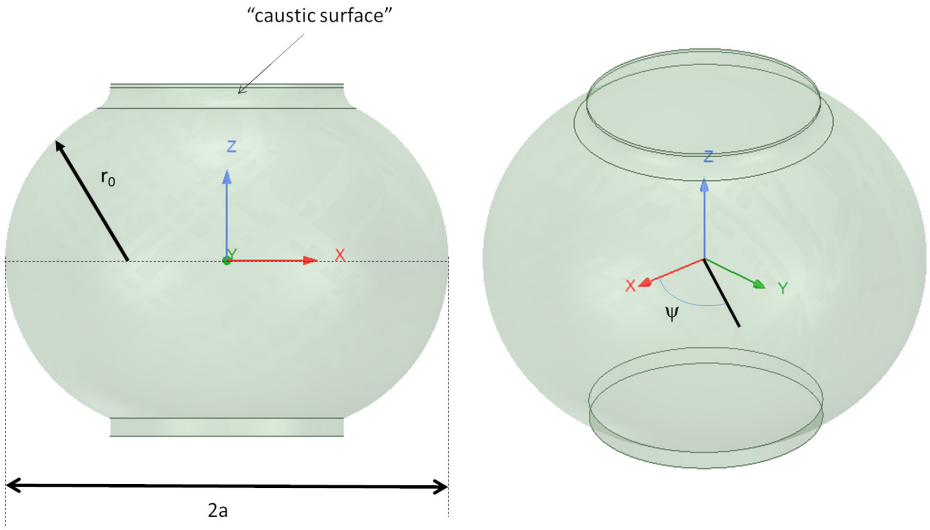

Figure 4.3. A sketch of BOC profile

The BOC cavity shape is sketched in Fig.4.3 and is chosen in order to excite resonant modes that have a spatial configuration similar to the transverse magnetic modes E_{mnq} of a cylindrical cavity with longitudinal axis z and radius $2a$, being, as usual, m, n, and q the azimuthal, radial and longitudinal indexes. As example the magnitude of the electric and magnetic field of the $TM_{16,1,1}$ cavity mode are given in Fig.4.4 and Fig.4.5, respectively. The electric and magnetic field lines are given in Fig.4.6. The electromagnetic field of such modes is concentrated in a relatively

small volume close to the cavity surface in the equatorial plane and does not radiate in outer space on the so-called "caustic" surfaces.

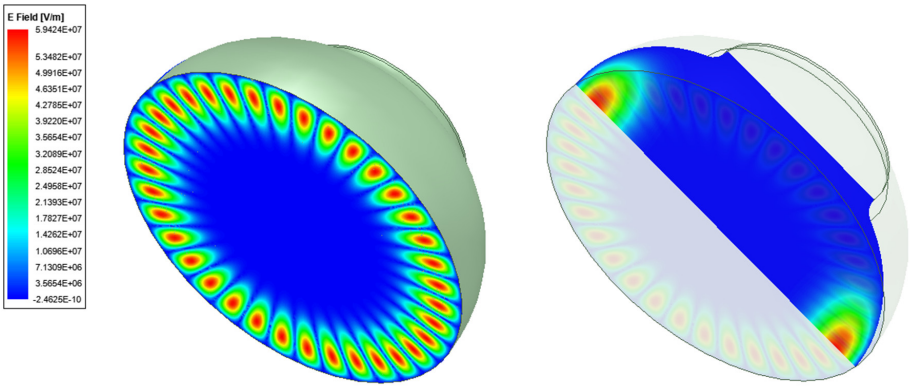

Figure 4.4. Electric field inside the cavity.

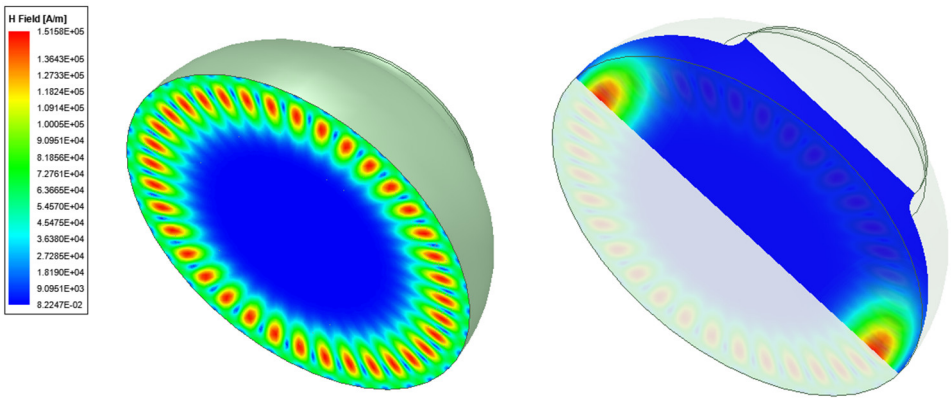

Figure 4.5. Magnetic field inside the cavity.

In theory the two plates on this surface can be completely opened and removed while the mode is still confined and resonating in the cavity. These modes are characterized by a very high quality factor, from hundreds to few hundreds thousand, depending on the working frequency and azimuthal number m, has illustrated in the following section 6.1. Typically these modes are called "whispering gallery" modes, because of their low attenuation in the equatorial region, similar to particular acoustic propagating waves.

The resonant frequencies of the BOC modes (that we will label with E_{mnq}) satisfy the following equations [132]:

$$ka = \nu_{mn} + \frac{(q - 1/2)\alpha}{sin\theta} \tag{4.31}$$

where k is the wavenumber in free space, a is the cavity radius, m is the azimuthal index, q is the longitudinal index of the mode, ν_{mn} is a root of the Bessel function order of m of the excited em mode E_{mnq}. Angle θ is equal to

$$\cos\theta = \frac{m}{\nu_{mn}} \tag{4.32}$$

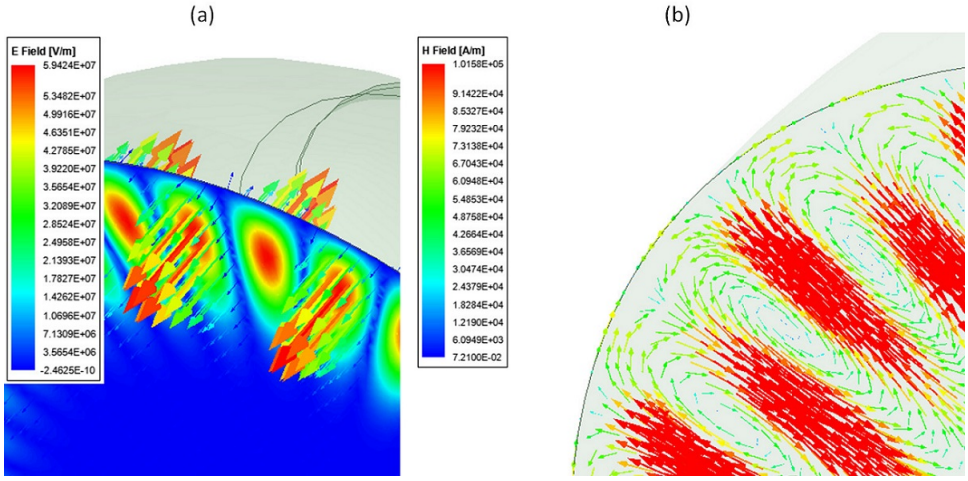

Figure 4.6. The electric *a*) and magnetic *b*) field lines inside the cavity.

the optimum cavity wall radius r_0 that allow to maximize the exponential decay toward the external caustic surface, is given by as $r_0 = 2a\sin^2\theta$, and the angle α is defined as

$$\sin\alpha = \sqrt{\frac{a}{r_0}}\sin\theta \tag{4.33}$$

The quality factor of the E_{mnq} modes, is given by:

$$Q = \frac{a}{\delta} \tag{4.34}$$

δ is the skin depth of the cavity wall material.

It is possible to demonstrate that for a given cavity geometry, the penetration of the modes towards the "caustics" surface, increases with the increase em field mode's radial - n and longitudinal - q indexes. This means that, if the caustics surface is not shielded, these modes can have large radiation losses in comparison with modes with n and q equal to 1 [127]. For this reason the mode's radial and longitudinal number are typically fixed to 1 while the azimuthal number m is fixed to reach the desired quality factor, as illustrated in detail in the chapter 4.2.1.

4.2.1 Working Principle

To correctly understand how the BOC pulse compressor system works, it is useful to compare it with the well know SLED system. As already put in evidence, in this last system, we have two modes (resonating at the same frequency) that are excited in two cavities through the hybrid. These modes are excited in quadrature and their reflections back to the source is canceled by the hybrid itself and combined to the 4-th port of the hybrid itself. The working principle of the BOC is similar. In the BOC two resonating modes are excited in quadrature in the same cavity through a particular configuration of the waveguide system and coupling holes, as illustrated in the following, and, thanks to this particular coupling system, their reflections back to the source are combined and canceled while they add on the propagating direction. For this reason from an electromagnetic point of view, the BOC system is

identical to the SLED [75], so we can apply equations derived in SLED - I section for the output power calculation.

More in detail, as for any resonator with azimuthal multi-polarity (m index), in the BOC cavity, we can excite two orthogonal standing wave modes which are proportional to $\sin m\psi$ and to $\cos m\psi$, ψ being the azimuthal angle of the spheroidal coordinate in the equatorial plane 4.7. The two cavity modes can be excited by

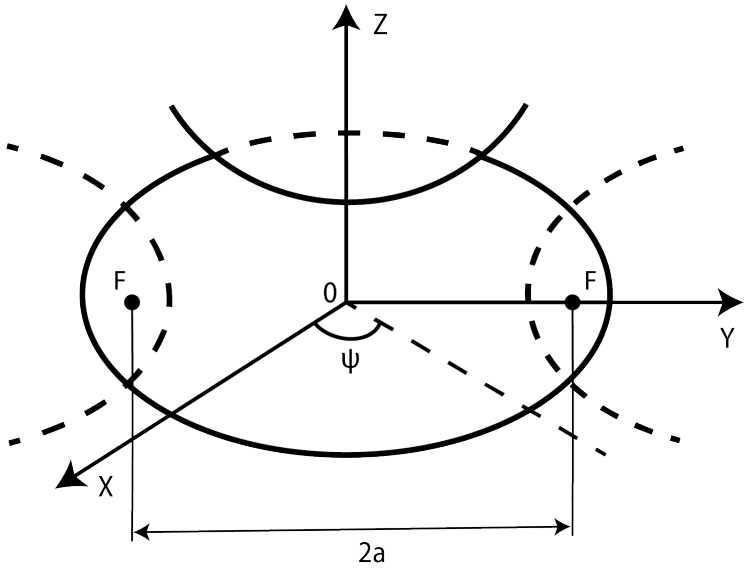

Figure 4.7. Simplified schematic of the BOC.[98]

means of multi-hole coupling slots through the common wall between the cavity and a waveguide, which surrounds the entire cavity at its median plane, as sketched in Fig.4.8. The coupling is magnetic. The wavelength in the waveguide is designed to be equal to the distance between the BOC mode lobes while the number of coupling holes to excite one mode polarity is typically chosen exactly equal to $2m$ in order to maximize the coupling effectiveness itself. To excite the two polarities, two sets of holes are opened in the common wall and the distance between this two sets of coupling holes is exactly $\lambda_g/4$. The total number of coupling holes is then $4m$. If, as already put in evidence, the wavelength in the waveguide is designed to be equal to the distance between the lobes of the single BOC mode, the propagating field in the waveguide excite the two orthogonal modes in quadrature [127].

For the two orthogonal SW modes in a cavity, in fact, the locus of maximum field strength of one mode coincides, locally, with the nodes of the other mode. Therefore, in a $\lambda_g/4$ multi-hole coupler, only half of the coupling holes (spaced by $\lambda_g/2$) drives the same SW resonance mode in the cavity. It is relatively easy to understand that this coupling system allow to cancel the reflections back to the source. As the field of the modes builds up in the cavity, the mode themselves start to radiate back into waveguide through the slots themselves. The field in the waveguide is radiated in both direction. The waves radiated in the forward direction by the two modes have all the same phase and they add up. On the contrary due to the $\lambda_g/4$ spacing between the holes, the waves emitted in the backward direction cancel each other in the waveguide because of the alternating phase delay between

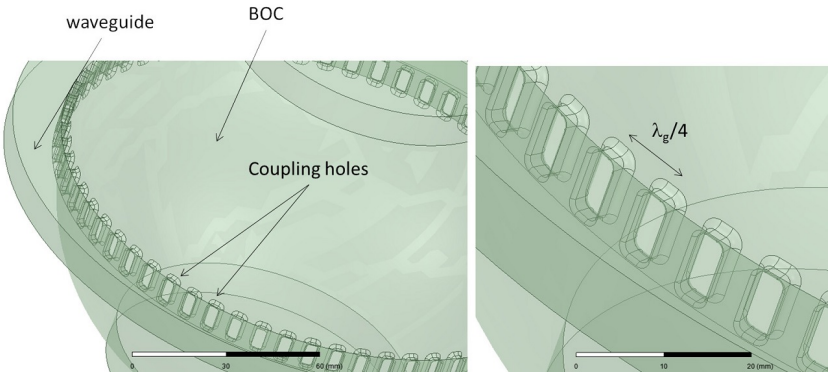

Figure 4.8. Coupling slots between the BOC and the waveguide.

even and odd numbered coupling holes. The principle is similar to that of the two holes directional coupler. Through this mechanism the reflections back to the power source are minimized.

The BOC pulse compressor system brings several advantages compared to the original SLED-I system. First of all such modes have a high intrinsic quality factor, there is no necessity to use a 3-dB hybrid to avoid reflections back to the source, the system require only one cavity instead of two that have to be tuned at exactly the same frequency with the same coupling and, moreover, the parasitic modes near the operating one are reduced because of the fact that the cavity can be opened and only the "whispering" modes, whose field is concentrated in the equatorial zone, can resonate [48].

4.3 SLED - II

SLED-II pulse compressor was also invented at SLAC in 1988 [73]. A block diagram of the SLED-II system used is shown in Fig.4.9. SLED-II pulse compressor is a modified SLED that gives a flat output pulse and higher intrinsic efficiency [145]. Here cavities are replaced by two high quality resonant delay lines. A resonant delay

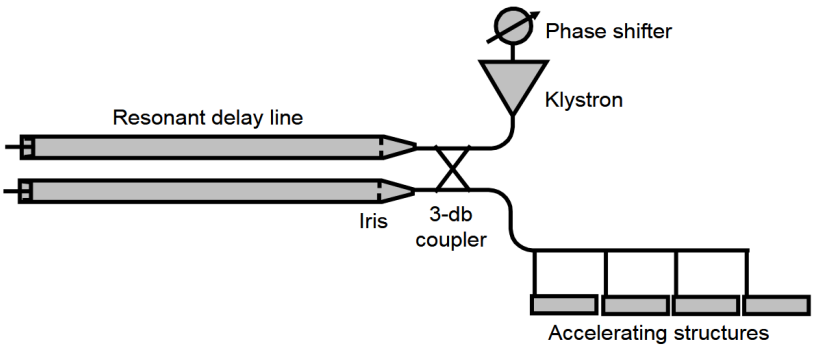

Figure 4.9. Schematic of SLED-II rf pulse compression system [133].

line is a transmission line terminated in a short circuit and connected to an input transmission line via a coupling iris. Because the speed of EM waves is finite, the

emitted field changes in discrete steps, with widths equal to the time it takes for a wave to transit down and back the length of the resonant line. Most importantly, this results in a flat top output pulse. Because of this, and because the use of long low loss TE_{01} mode lines reduces the losses, and because its reflections during charging are less, SLED-II is more efficient than SLED. But, SLED-II is impractical at low frequencies because the length and diameter of the required resonant delay line are large. It becomes practical at X-band frequencies.

The distance between the coupling iris and the short must be an integral multiple of half guide wavelengths, and the round-trip time delay T_j between the coupling network (iris) and the short equals the desired output pulse length. After turning on an incident field of amplitude E_i, the emitted field during the first round trip time is $E_e(0) = 0$. After nT_d time intervals it is given by:

$$E_e(n) = E_i \frac{(1-s^2)e^{-2\tau}}{1-se^{-2\tau}}(1-s^n e^{-2n\tau}) = Eef(1-s^n e^{-2n\tau}), \quad n = 1, 2, 3, ... \tag{4.35}$$

s is the reflection coefficient of the coupling network when the delay line is terminated in a matched load and τ is the attenuation of the delay line in nepers. Superposition with the iris reflection yields:

$$E_{out}(n) = E_e(n) - sE_i \tag{4.36}$$

At time $t = (C_r - 1)T_{cp}$, the phase of the input pulse is shifted by π so that the waves add and we get a compressed output of duration $T_{cp} = T_b$ with the amplitude:

$$E_{cp} = E_{ef}(1 - (se^{-2\tau})^{C_r - 1} + s)E_i \tag{4.37}$$

The compression ratio C_r is an integer. For a given C_r and τ, s can be chosen to maximize E_{cp}. The power gain and compression efficiency are

$$G = (E_k/E_r)^2 \quad \eta = G/G_r \tag{4.38}$$

The theoretical limit of G is nine.

Such a system has been successfully applied in operation of SLAC at a frequency of 2.856 GHz and has the following parameters: compression ratio $C = 6$, power gain $M = 4.1$, and efficiency $\eta = 68\%$ [133].

Chapter 5

Realization of accelerator components without brazing

The commonly used material for accelerating cavity fabrication is copper. This material is used for its very good conductivity, low secondary emission yield (SEY), that allows to avoid multipacting phenomena, reasonable cost, machinability at very good surface roughness (up to few nm), possibility to weld or braze it, and good performances at high electric field gradient [88], [144].

Accelerating cavities are usually made of many single cells welded together. The most common welding techniques, used worldwide, are: brazing, TIG (tungsten inert gas) welding, electron beam welding and diffusion bonding.

Brazing is a joining process in which a metal alloy is melted and distributed by capillarity between the two surfaces to be joined. No melting of the base metals occurs in brazing, but only the filler melts [79].

In TIG welding process the heat for welding is produced by striking an arc between two parts to be welded and an electrode, using a constant or pulsed voltage supply. This method uses a non-consumable tungsten electrode which, in the plasma process, has a high-speed gas flowing around it to produce a constriction for the arc. Argon or helium gases are used to shield the weld area from the normal oxidizing atmosphere [144].

Electron-beam welding (EBW) is a fusion-welding process in which the heat for welding is produced by a highly focused, high-intensity stream of electrons impinging against the work surface. Electron-beam welding is noted for high-quality welds with deep and/or narrow profiles, limited heat affected zone, and low thermal distortion. Welding speeds are high compared to other continuous welding operations. No filler metal is used, and no flux or shielding gases are needed. Disadvantages of EBW include: high equipment cost, need for precise joint preparation and alignment, and the limitations associated with performing the process in vacuum. In addition, there are safety concerns, because EBW generates X-rays that have to be shielded [79].

A diffusion bond is created between extremely smooth surfaces (optical finish at nm level) under high pressure ($> \ 10N/mm^2$) and temperature ($> \ 350°C$), in vacuum furnaces or controlled H_2 atmosphere [88]. In contrast to brazing, no melting takes place, as the name implies. It involves the interdiffusion of the atoms across the surfaces of the structure [89].

For high gradient accelerating structures in which both vacuum seal and rf contact have to be guarantee, the most used techniques are brazing and diffusion bonding. They are expensive solutions which require big vacuum furnaces or furnaces with a controlled atmosphere. Moreover, particular attention has to be paid to keep the parts well aligned during the thermal cycle.

The design of the interfaces to be brazed should be done according to precise rules taking into account the expansion of the materials to allow the brazing to flow through the gap. Hence these high-temperature processes require high-level skills and have a non-negligible probability of failure (as example, vacuum leaks or misalignment of the joined parts). Many are the risks of both brazing and diffusion bonding which could lead to either a failure of the process itself or damage to the structure or both. For example, if the brazing alloy is not properly placed, small pockets with air can remain around the filler regions causing virtual leaks [21] which are sources of trapped gas into the ultra-high vacuum volume.

Another effect of high-temperature brazing or bonding processes is the fact that copper is annealed. Recent experiments have demonstrated that structures made out of hard copper can achieve higher accelerating gradients with lower RF breakdown rates (BDR) with respect to the high-temperature treated ones [62]. Also, the mechanical properties of the annealed copper, in terms of hardness and mechanical strength, are strongly reduced with respect to the hard copper one. Brazing and diffusion bonding are quite expensive processes since they require big furnaces.

The possibility to use hard copper motivates scientists to develop new brazing free technologies. In particular recent developments [34, 35], [38], [61], have opened new perspectives on the realization of complex accelerating structures without brazing.

There is also an important technology transfer outcome related to the potential realization of brazing free accelerating structures. Large vacuum furnaces, in fact, are available only in large laboratories or relatively big private companies. The possibility to fabricate structure without brazing can open the accelerator market, in principle, to all small and medium enterprises that work in the mechanical precision field. This can strongly enlarge the market possibility with a potential strong reduction in the cost of the components.

The brazing free method developed at LNF [34, 35] is based on the use of special rf-vacuum gaskets that simultaneously guarantees the vacuum seal and the rf contact avoiding sharp edges and gaps.

The mechanism of gasket compression is illustrated in Fig.5.1.

So far two rf-guns (for SPARC_LAB [26] and ELI-NP [9] projects) in S-band have been successfully designed and tested on high power [32, 33], and two more RF guns for the CLEAR [4] and SPARC_LAB [18] projects are now under construction. On Fig.5.2, as example, the mechanical design of the ELI-NP rf gun is reported and, on Fig.5.3, the fabricated gun with gaskets.

In conclusion the main characteristics and advantages of this fabrication technology are summarized in the following. It allows to avoid expensive brazing or bonding process in large vacuum furnaces with a reduction of the cost and required realization time. The bolts and screws, well separated from the vacuum region, allow to re-open the structure and substitute the rf gasket several times. The realization of devices using hard copper allows to reach, in principle, higher surface fields. It is, in principle, possible to fabricate a particular device using different metallic materials

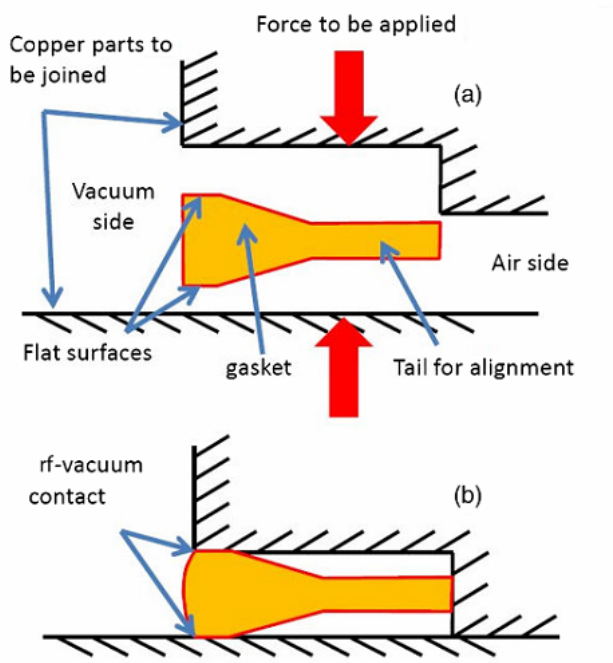

Figure 5.1. Geometry of the gasket and mechanism of gasket compression: (a) uncompressed gasket; (b) compressed gasket [33].

joined with gaskets. The rf and mechanical designs of a structure have to be adapted to fabricate a given structure with this new technology.

Due to all mentioned advantages we proposed to adopt this fabrication technology also for the realization of BOC pulse compressors and the present thesis work is focused on the design of the first BOC brazed free device in X band.

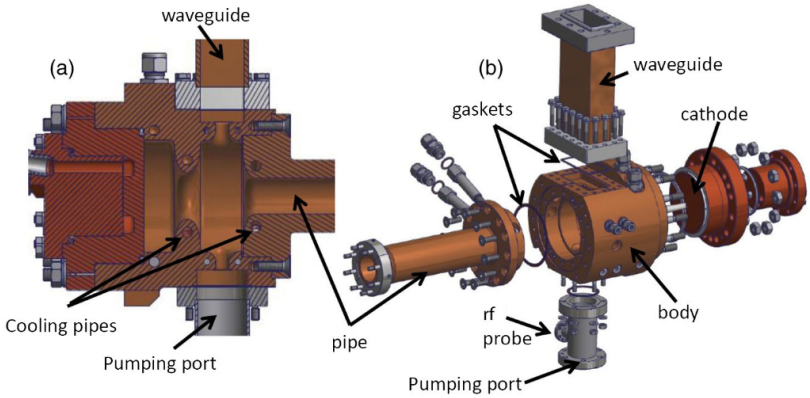

Figure 5.2. Detail of the ELI-NP gun mechanical drawing [33].

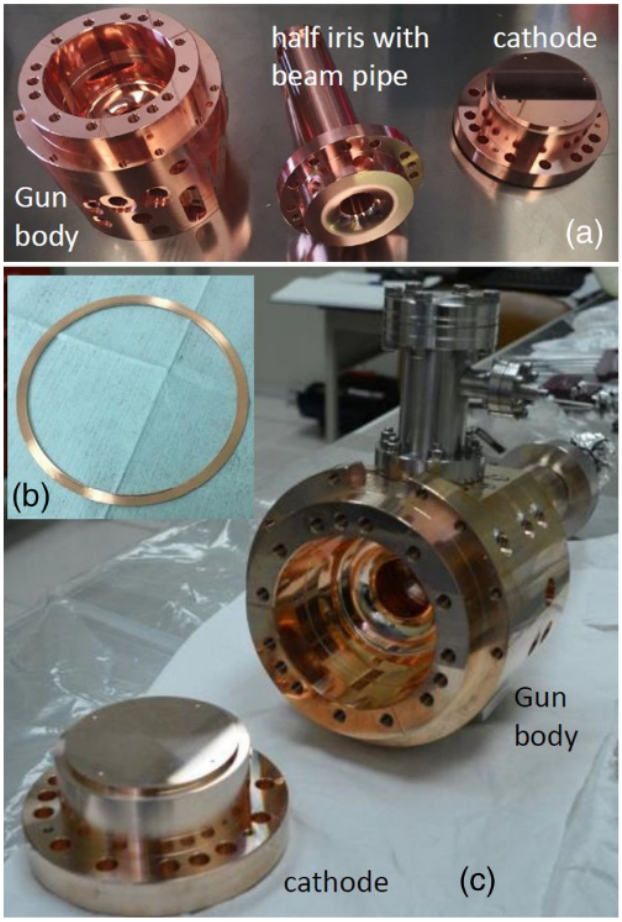

Figure 5.3. ELI-NP rf gun: a) Main gun components before clamping; (b) special gasket; (c) gun during assembly [33].

Chapter 6

RF pulse compressor design

6.1 BOC parameters

As already pointed out the present thesis work has been oriented to the design of the BOC pulse compressor system for the project EUPRAXIA@SPARC_LAB. To this purpose, the first step has been the definition of the BOC parameters in term of unloaded and external quality factors. As extensively discussed in [27], the pulse compressor system is a fundamental device in the accelerating module and the optimization of the accelerating structures in term of iris modulation, group velocity and structures length include this system. According to Eq.4.34, the quality factor of the TM modes in the BOC cavity is given by:

$$Q = \frac{a}{\delta} \tag{6.1}$$

Where $\delta = 1/\sqrt{2\pi\mu\sigma}$ is the skin depth and a is the large radius of the cavity. The unloaded quality factor is then fixed by the large radius a of the cavity. On the other hand, the radius a is related to the azimuthal index m of the mode and, as a consequence, it is possible to relate the Q factor to the azimuthal index m.

Fixing the copper conductivity equal to $\sigma = 5.81 \times 10^7/\Omega m$ at 20° [7] and $f = 11.9942\ GHz$ which gives skin depth equal to $\delta \approx 6.03^{-7}\ m$, we have calculated the quality factor as a function of the azimuthal index m. The result is given in Fig.6.1 where the values have been compared to HFSS simulations showing a very good agreement. The details of the simulations setup will be discussed in the next paragraphs.

The overall accelerating structure efficiency is described by a particular quantity called effective shunt impedance of the accelerating structure R_{sh} [110], which is defined as follows:

$$R_{sh} = \frac{G^2 L}{P_{kly}} \tag{6.2}$$

where G is the average accelerating gradient, L is structure length and P_{kly} is klystron power.

The effective shunt impedance is a function of the accelerating cavity parameters (length, iris diameter) and pulse compressor quality factor and coupling coefficient. The EUPRAXIA@SPARC_LAB accelerating structures are 0.9 m long structures

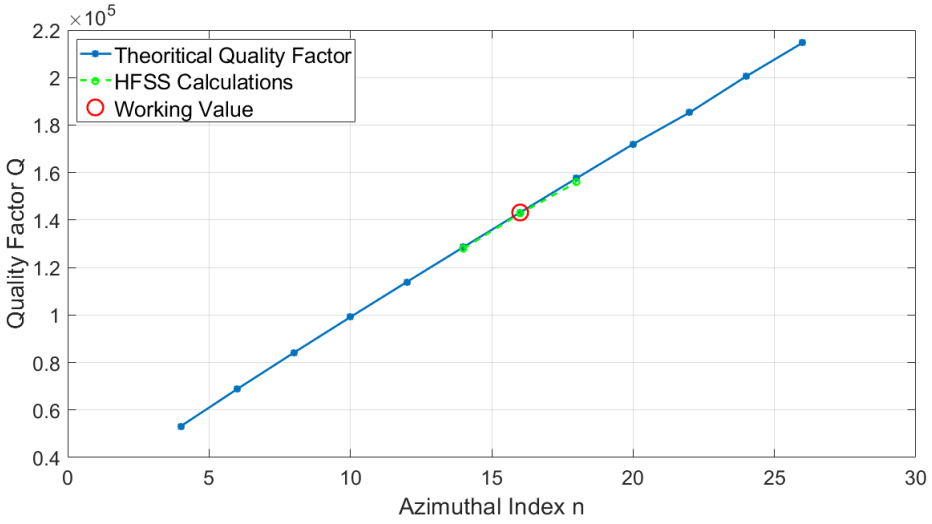

Figure 6.1. Quality factor Q as a function of the azimuthal index m.

with an average radius of the irises equal to 3.5 mm and a linear tapering of the irises themselves, as reported in Tab. 3.4 [27]. The structures have been optimized assuming a BOC quality factor equal to 150000. The effective shunt impedance as a function of the azimuthal index of the mode or mode's quality factor is given in Figs. 6.2 and 6.3. The results have been obtained using the approach well described in [27].

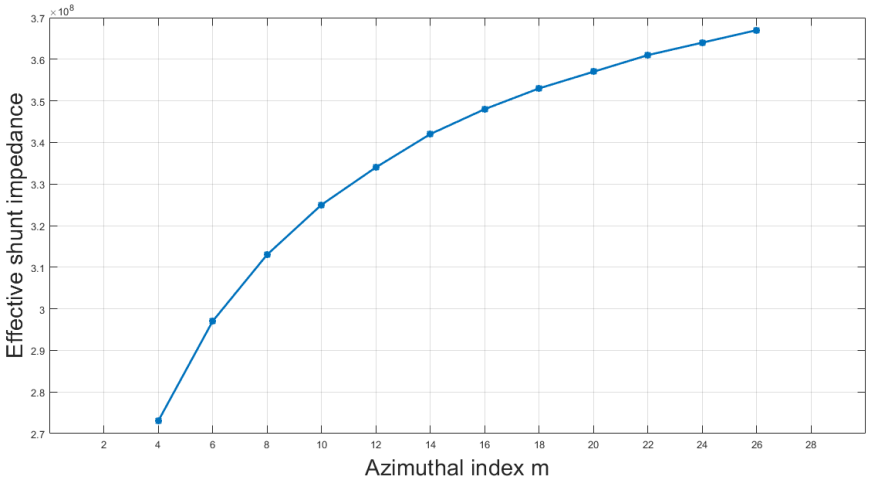

Figure 6.2. Effective shunt impedance versus mode's azimuthal index.

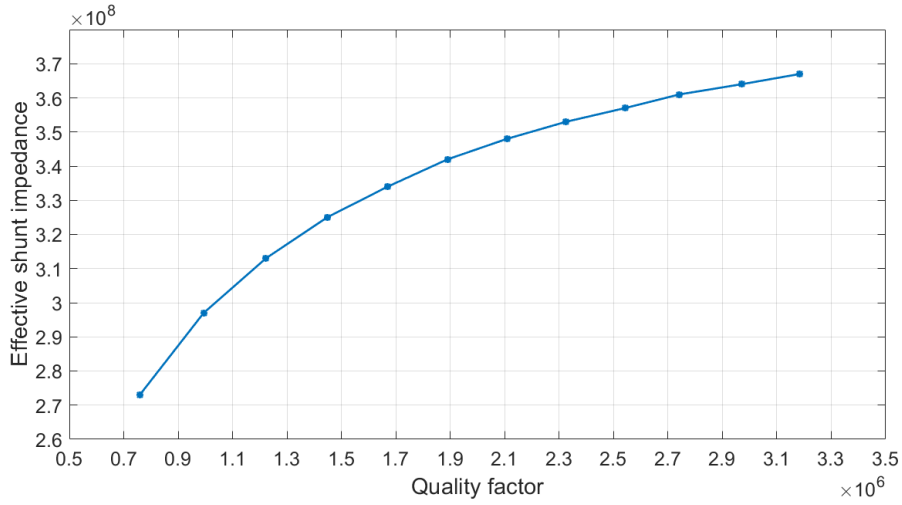

Figure 6.3. Effective shunt impedance versus mode's quality factor.

For a first design of the BOC pulse compressor, we decided to fix m equal to 16 ($TM_{16,1,1}$ mode) that give an unloaded quality factor $Q \approx 143\ 000$ 6.1.

The external quality factors of the BOC that optimize the effective shunt impedance are given in 6.4 where the external quality factors are reported for the different unloaded quality factors. As we can see for $Q_0 = 143000$ external

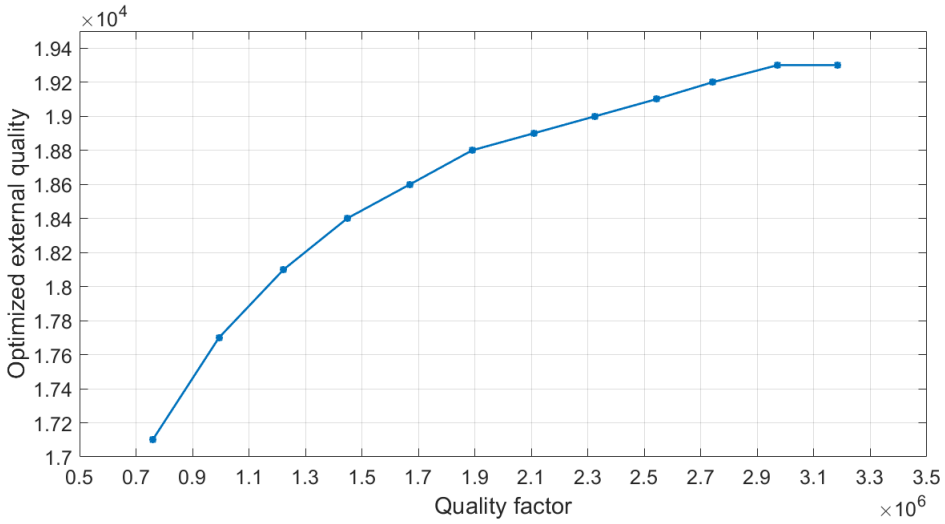

Figure 6.4. Optimized external quality factor versus unloaded quality factor of the BOC.

quality factor is equal to $Q_{ext} = 18400$ so coupling coefficient is $\beta = \dfrac{Q_0}{Q_{ext}} = 7.8$. Just as example we report in Fig.6.5 the theoretical output power after compression for two different quality factors of the BOC.

The final design BOC parameters are reported in Table 6.1:

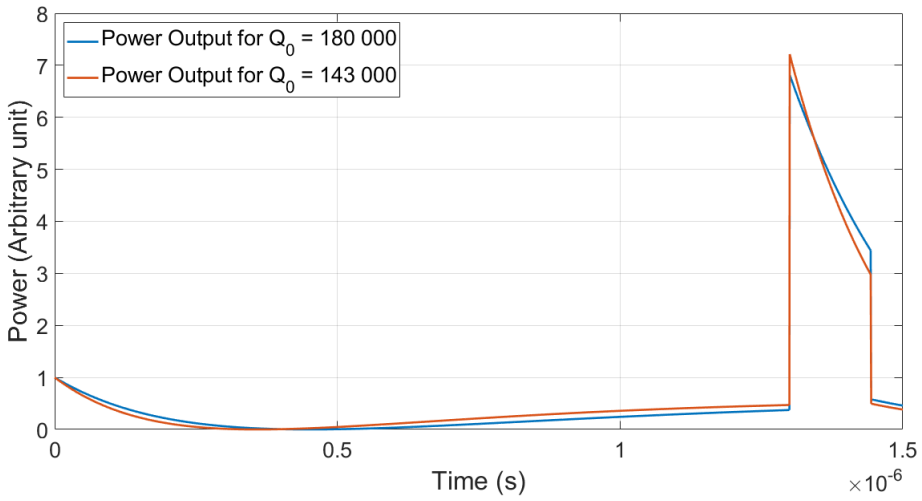

Figure 6.5. Power output for $Q_0 = 180\ 000$ and $Q_0 = 143\ 000$, $\beta = 7.8$ in both cases.

Table 6.1. Design parameters of the BOC pulse compressor.

Type	Barrel Open Cavity
Frequency	11.9942 GHz
Resonant Mode	$TM_{16,1,1}$
Coupling factor (β)	7.8
Q_0 quality factor	143 000

6.2 Electromagnetic design of the cavity

The design of the cavity has been performed by ANSYS HFSS [12].

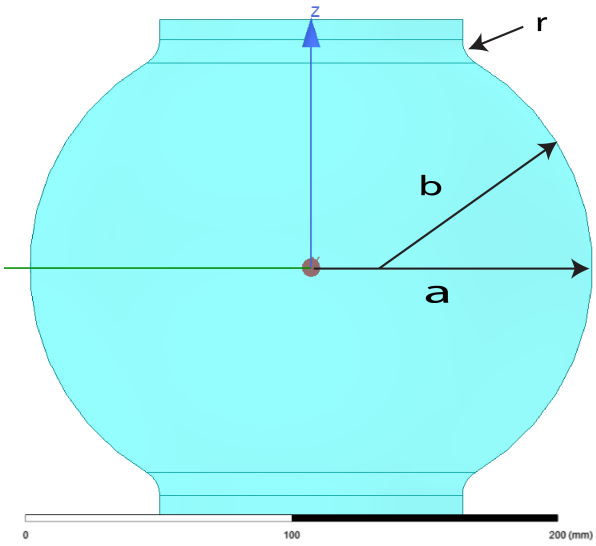

Figure 6.6. Sketch of the BOC geometry with main parameterized dimensions.

A sketch of the cavity geometry is shown in Fig. 6.6, where a is the cavity large radius, b is the transverse radius of curvature and r is the radius of the end's rounding. According to Eq. 4.31, for a working frequency of 11.9942 GHz and the $TM_{16,1,1}$ resonating mode, a is equal to 86.28 mm and b is equal to 73.19 mm. To validate this theoretical values HFSS eigen mode simulations have been carried out.

The simulated geometry is given in Fig. 6.6. Because of the azimuthal periodicity we have simulated just one slice of the cavity with the proper boundary conditions as given in Fig.6.7. The simulated quality factor has been already reported in Fig.6.1 for different azimuthal mode numbers and perfectly agrees with the theoretical expectations.

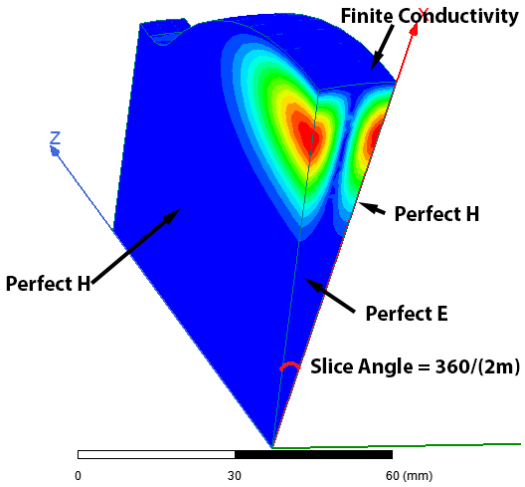

Figure 6.7. 'Slice' with angle value and boundary conditions.

Figure 6.8 shows the electric field magnitude in the complete simulated cavity. The final simulated unloaded quality factor has been 143 000 that is in quite good agreement with the theoretical calculated value. As a next step the coupling with

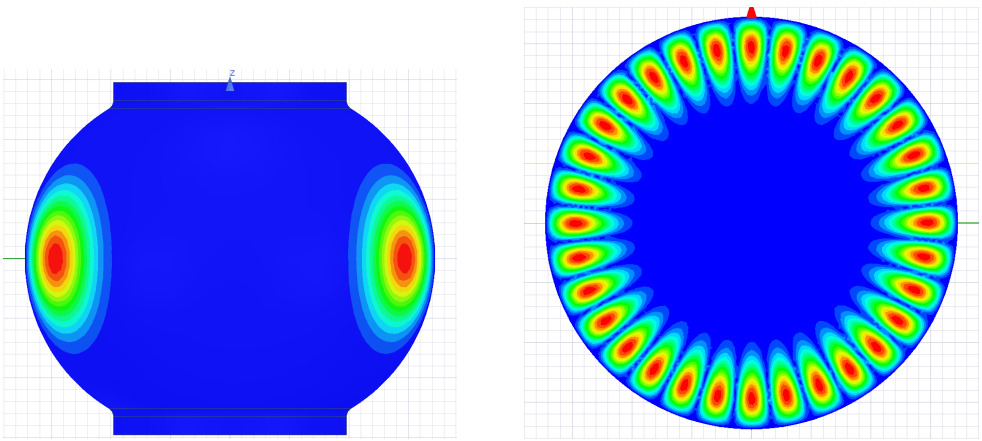

(a) Side view **(b)** Top view

Figure 6.8. Electric field amplitude for the $TM_{16,1,1}$ resonant mode

the feeding waveguide has been designed.

The overall BOC with the waveguide system is given in Fig.6.9.

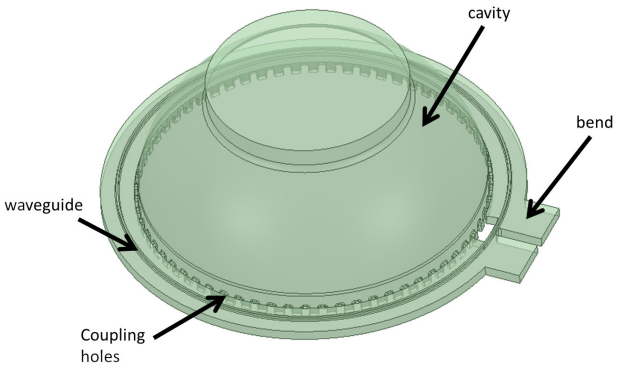

Figure 6.9. BOC with the waveguide.

The design has been divided in several phases: design of the surrounding waveguide with gap, design of the bend, tuning of the coupling slots and final waveguides dimension, sensitivity analysis with respect to the geometrical parameters to fix the mechanical tolerances. In the following the different phases are illustrated in detail.

6.2.1 Design of the surrounding waveguide with a gap

To allow a realization of the structure with the gaskets-clamping technique, a gap has been introduced in the center of the waveguide and bend as sketched in Fig.6.10. This gap, if properly designed, doesn't affect the TE_{01} field distribution in the waveguide, but gives the possibility to clamp the structure avoiding any brazing, as discussed in detail in Chapter5. Also, the increase of the electric field magnitude due to the presence of the gap itself can be taken under control by a proper design of the rounded corners.

Figures 6.10 show the geometry of the waveguide and bend with the gap.

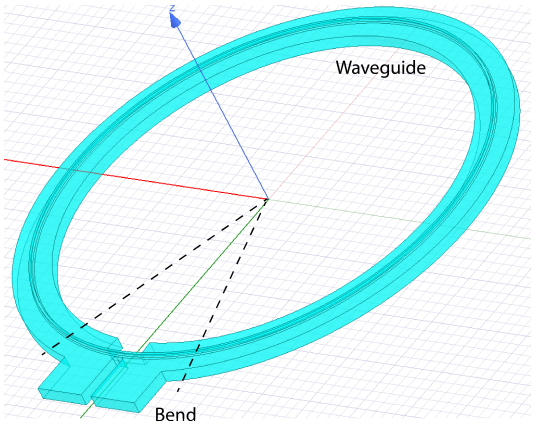

Figure 6.10. Waveguide with bends.

The gap's width w_{gap} has been reduced up to 1 mm in order to reduce the electric

field penetration in the gap itself and, at the same time, the electric field increase due to the gap itself. For this last reason also rounded corners of radius r equal to 0.5 mm have been introduced. This gives an increase of the surface electric field on the corner with respect to the unperturbed waveguide of the order of 40% if the gap is inserted exactly in the center of the waveguide. In the first design of the structure we decided to consider this central position of the gap, but it can be also shifted with respect to the central position without affecting consistently the mechanical drawing of the overall BOC, but with a consistent reduction of the peak electric field in the rounded corners. In a further implementation also this alternatives solutions can be implemented.

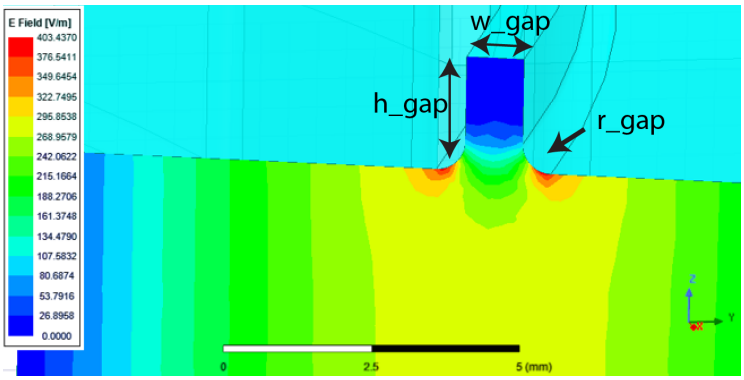

Figure 6.11. Waveguide transverse profile with parameterized dimensions and transverse electric field amplitude.

As an example in Fig.6.12 the field increase for different gap positions are considered putting in evidence the strong reduction if the gap is off-center. Also the increase in the magnetic field and attenuation have been considered. The magnetic field amplitude for two different position of the gap is given in Fig.6.12 and shows a negligible increase in the H field amplitude. Concerning the attenuation, the increase is a factor 1.2 with respect to the standard waveguide.

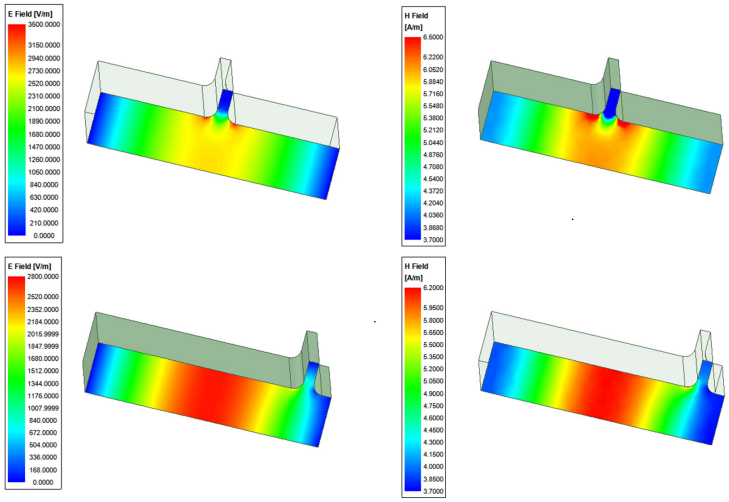

Figure 6.12. Electric and Magnetic fields inside the waveguide for different gap positions.

As already illustrated in the previous chapter, also the waveguide width has to be tuned to match the requirement in terms of perfect excitation in quadrature of the two modes when the waveguide width is correctly tuned also the reflections back to the input port are minimized, since the power that flows from the modes in the cavity into the waveguide propagate in the direction of the waveguide exciting mode and is canceled in the backward direction, as already illustrated.

The theoretical width w of the waveguide has been calculated according to the formula [76]

$$\frac{2\pi(a+\Delta+w)}{m} = \frac{\lambda_0}{\sqrt{1-(\lambda_0/2w)^2}} \tag{6.3}$$

where m is azimuthal index number, a is large radius of the cavity, Δ is the common wall thickness equal to 2 mm in our case, and λ_0 is wavelength in free space.

In our case we obtained $w = 15.6\ mm$. This formula allows to estimate the waveguide width, but, for its final dimension, e.m. simulations have been performed to take into account the perturbation of the holes and coupling effects between the waveguide and the cavity itself.

6.2.2 Design of the bend

In order to allow the feeding waveguide to surround the BOC a bend has been introduced. The bend has been designed to minimize the reflection at the waveguide input port. To this purpose, the geometrical parameters reported in 6.13 have been optimized and the final reflection coefficient of the bend input port is S_{11} < -36dB As given in Fig.6.14 where the reflection coefficient as a function of frequency has been reported.

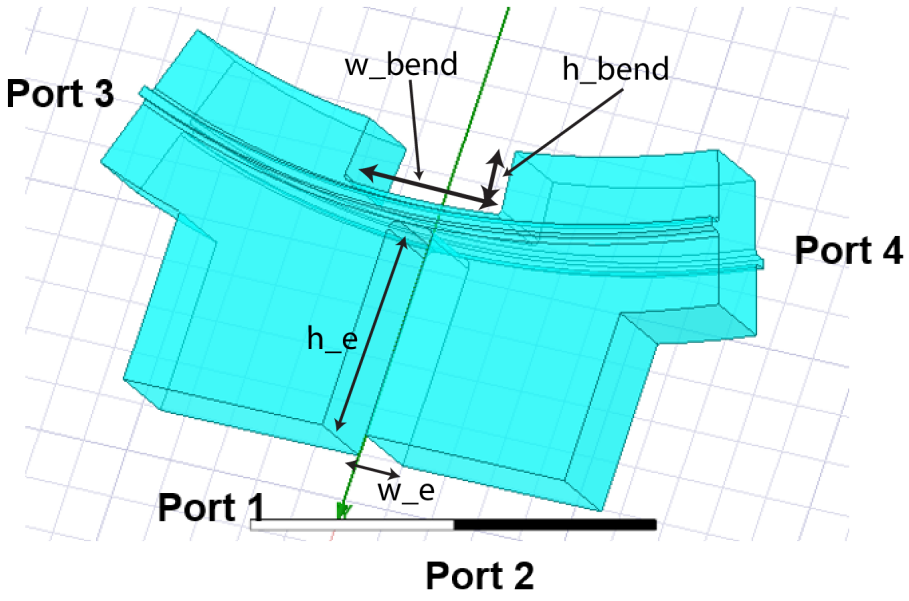

Figure 6.13. Bend geometry with main parameterized dimensions.

For the same purpose to fabricate the BOC with the clamping technology an aperture between the two waveguide in the bend has been inserted. Because of this,

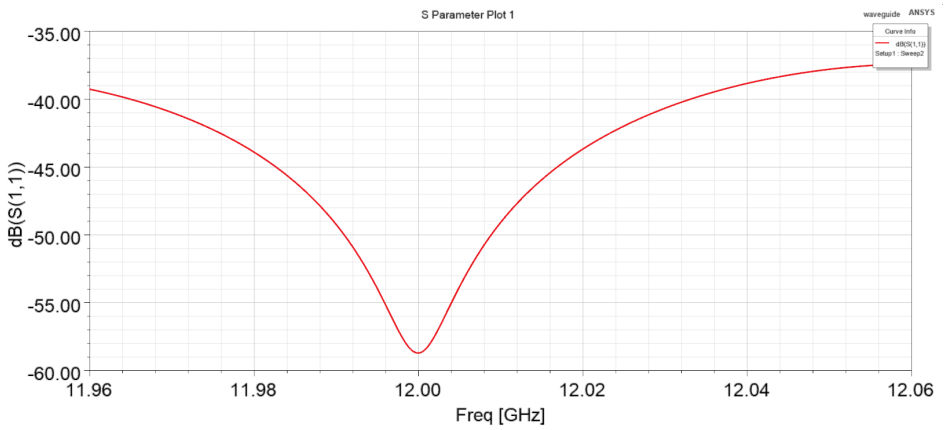

Figure 6.14. Reflection coefficient at the bend input port as function of frequency.

input and output ports are not completely separated, but the calculated transmission coefficients between ports is completely negligible since they are at the level of -87 dB as reported in Fig.6.15.

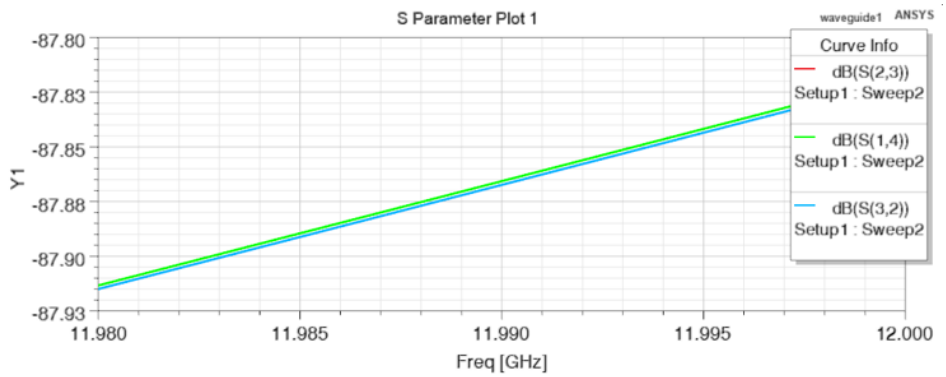

Figure 6.15. Scattering parameters S_{14}, S_{41}, S_{23}, S_{32} for the input and output ports of the bend.

6.2.3 Design of the coupling slots

The external quality factor is fixed by the coupling aperture and wall thickness between the cavity and waveguide. We used coupling slots as described in 4.2.1, which magnetically couple the cavity modes and the waveguide. The geometry of the holes is shown on Fig. 4.8. In particular, the wall thickness has to be kept large enough to avoid structural weakening of the cavity (2 mm). According to the design criteria described in 4.2.1, 62 coupling holes have been opened between the waveguide and the cavity. These slots allow to excite in the structure the two modes, in quadrature, that result in a rotating final mode if the waveguide width is properly tuned and if the field is monitored at the resonant frequency of the structure and in time domain. The slot width have been gradually increased up to 4 mm. In Fig.6.16 we report the coupling coeffciet as a function of the hole width. It is important to remark that each point has been obtained by an e.m. simulations of

the overhall structure retuning the widths of the waveguide to take into account the perturbation induced by the slots and maintaining a perfect synchronism between the final rotating mode and the waveguide propagating mode.

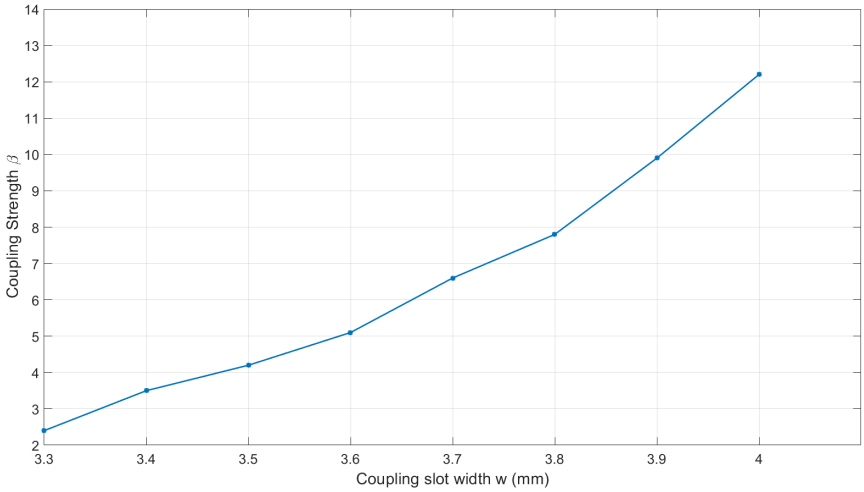

Figure 6.16. Coupling factor versus coupling width.

At the end, according to the optimal coupling coefficient that maximize the shunt impendace, we have chosen a slot width equal to 3.8 mm.

The final transmission and reflection coefficients between the waveguide ports are given in Fig.6.18 and 6.19. The final reflection coefficient at the resonant frequency has been finally less than -25 dB. In Fig.6.17 we've reported the amplitude of the electric field at a given instant in the middle plane of the cavity that put in evidence the matching between the final waveguide wavelength and the BOC rotating mode.

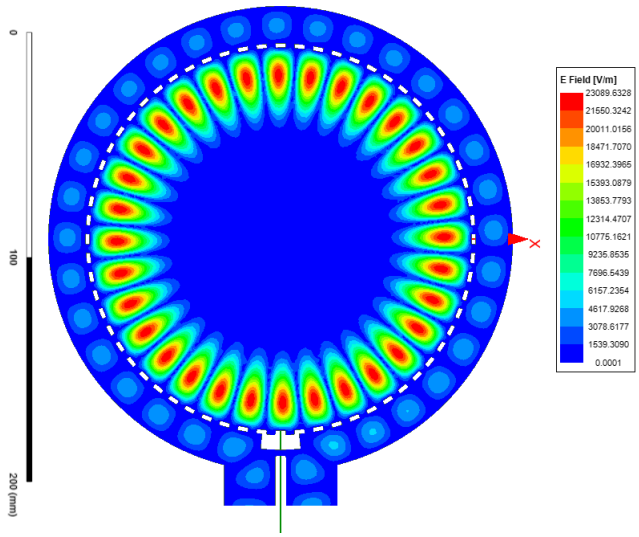

Figure 6.17. Electric field magnitude in the cavity and waveguide.

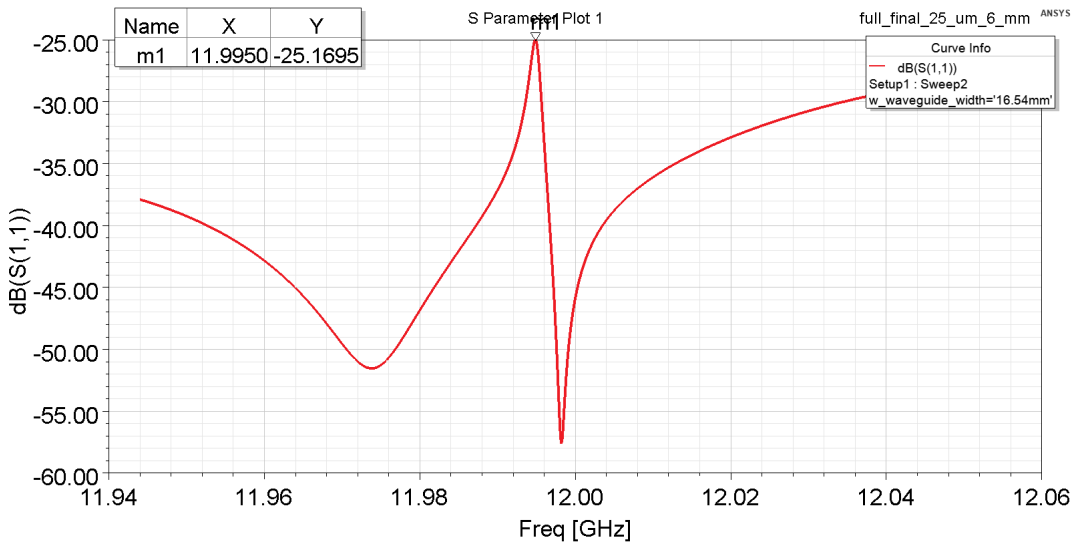

Figure 6.18. Reflection coefficient at the waveguide input port as a function of frequency for the final simulated structure.

To check presence of the parasitic modes near the working one, HFSS driven sweep simulation was performed in the +/- 50 MHz range. As clearly visible in Fig. a) 6.19 the only excited mode is our working mode $TM_{16,1,1}$ that is strongly overcoupled Fig. b) 6.19 and the β the coupling coefficient has been calculated according to the formula [46]:

$$\beta = \frac{(1 + S_{21})}{(1 - S_{21})} = 7.8 \tag{6.4}$$

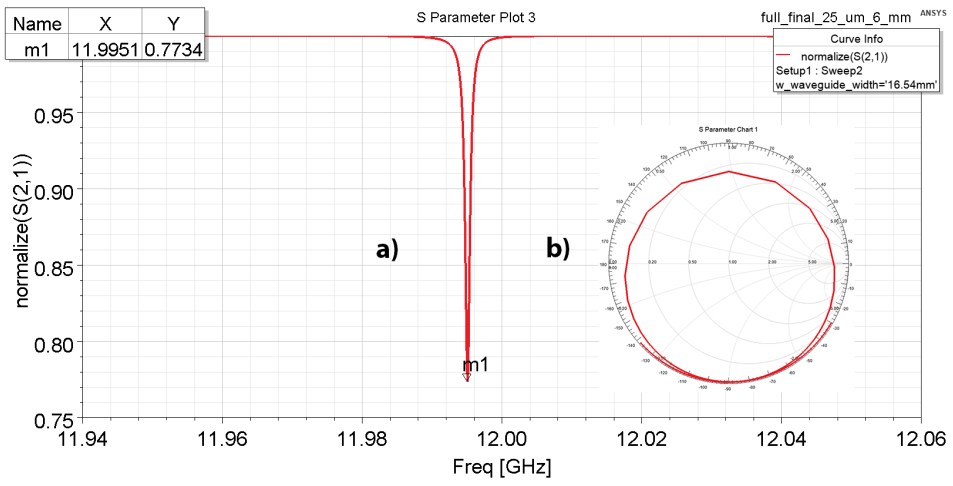

Figure 6.19. a) Magnitude of the S_{21} as a function of frequency, b) Smith chart of the transmission coefficient S_{21}.

The final parameters of the pulse compressor are summarized in the Tab. 6.2:

Table 6.2. Main parameters of the BOC pulse compressor.

Type	Barrel Open Cavity
Frequency	11.9951 GHz
Resonant Mode	$TM_{16,1,1}$
Diameter	171.3 mm
Number of coupling slots	62
Coupling factor (β)	7.8
Q_0	143000
Slot width	3.8 mm
Slot height	9.5 mm
Wall thickness	2 mm

6.3 Sensitivity calculations

Sensitivity studies allow to estimate which is the needed precision we need in the machining of the structure since the tuning is not possible (or difficult) in our case. More precisely, it is possible to tune the structure by changing the temperature of the cooling system within a reasonable range of few degrees that we fixed in the interval of $\pm 5°C$. Assuming that we can tune the resonance frequency of the cavity by changing the temperature by $+/-5\ °C$ and assuming a thermal expansion coefficient of the copper equal to $\alpha = 16.974 \times 10^{-06}$, we can calculate the frequency range of tunability with the simple formula:

$$\frac{\Delta f}{f} = \alpha \times \Delta T = 11.9942 \times 10^{9} \times 16.974 \times 10^{-06} \times 5 = 1\ MHz \tag{6.5}$$

In our case this give a range ± 1 MHz.

The most critical geometrical parameters in the sensitivity calculation is, obviously, the cavity large radius a. The resonant frequency as a function of the cavity radius a is given in 6.20 and gives a frequency sensitivity to the cavity radius of $\frac{\Delta f}{\Delta a} = 136$ MHz/mm.

According to the previous considerations on the cavity range of tunability with temperature, it is quite easy to note that, without any mechanism of tuning, the machining precision must be maintained at $\frac{\Delta f}{A} = \frac{1 \times 10^6}{136 \times 10^6} = 7/\mu m.$

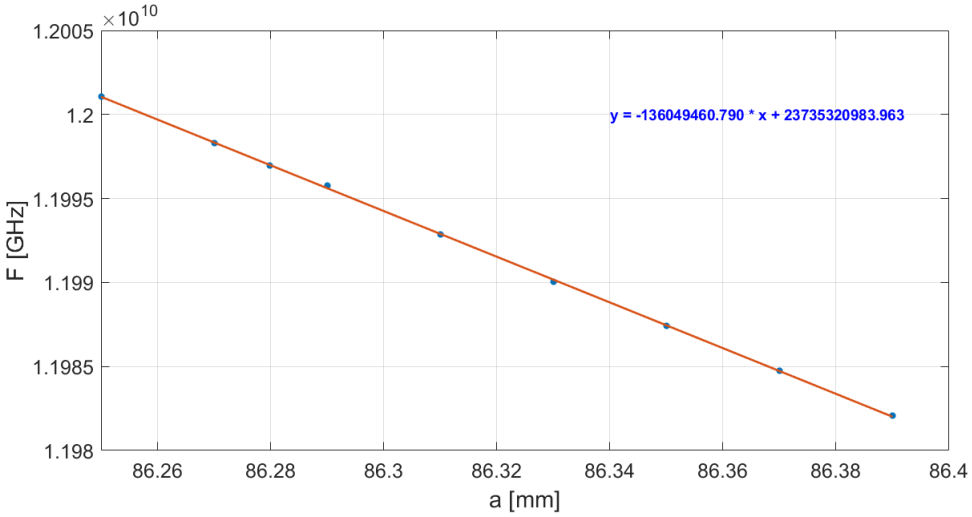

Figure 6.20. Cavity Resonant frequency as a function of the large radius.

The last geometrical parameter we have analyzed for the sensitivity analysis is the waveguide width. In Fig.6.21 the reflection coefficient S_{11} for proximity near final waveguide width value are presented. It can be seen that S_{11} has a minimum on nominal value.

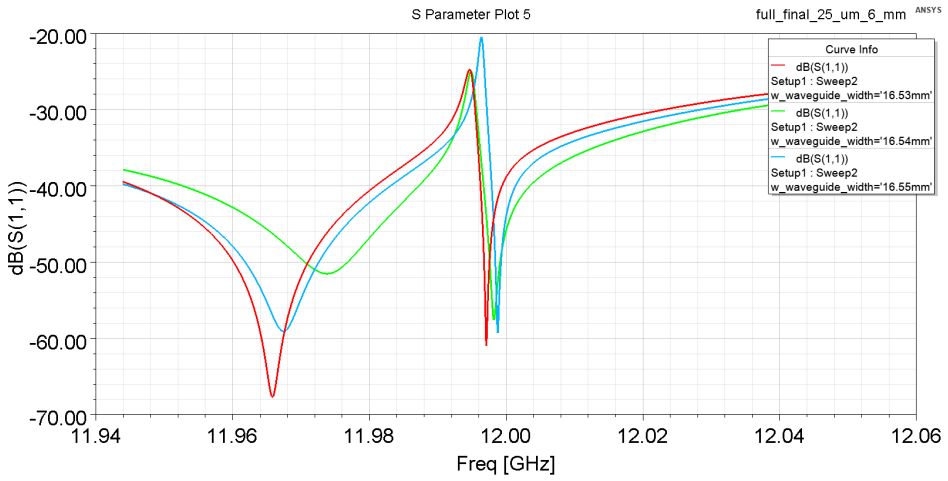

Figure 6.21. S_{11} in the proximity of nominal value.

6.4 Thermo-mechanical simulations

In order to properly design the cooling system, we have performed thermo-mechanical simulations. To this purpose a combined thermo-mechanical analysis has been performed using ANSYS Workbench[12]. It allows to combine an electromagnetic simulation with a thermo-mechanical analysis. In this platform, the calculated electromagnetic field heat load due to rf losses is sent to the thermal module and the temperature distribution is calculated. This temperature profile is then imported in the structural analysis module that calculates the deformations. The deformed

structure can be imported back in the ANSYS HFSS solver which calculates the perturbed resonant frequency and field distribution. The ANSYS Workbench ambient is shown in Fig.6.22.

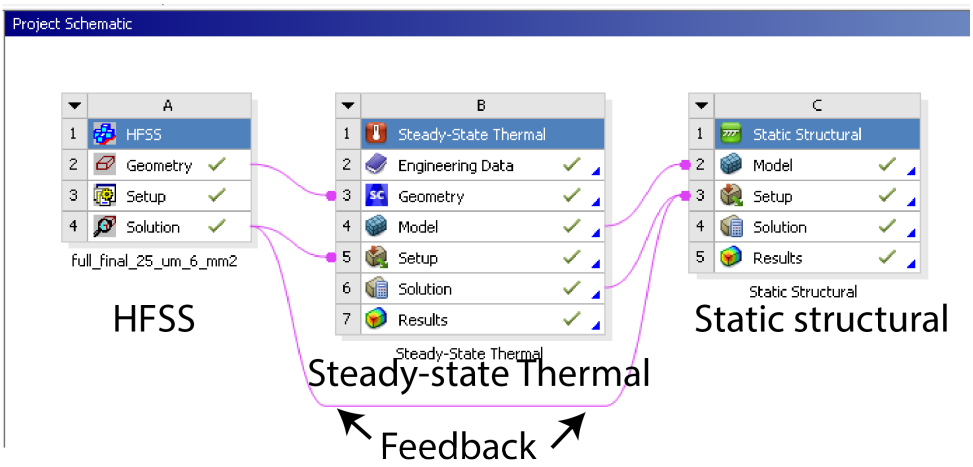

Figure 6.22. ANSYS Workbench Analyses Schematic.

In general, a coupled field analysis by a unique code is more efficient with respect to using different specialized software. In the case of multi-physics code, like ANSYS, exchange of the intermediate results between different modules is a built-in feature of the software, so that the model can be established by one single software and related data can be transferred more efficiently and easily between elements, which gives more exacts simulations and reduces errors [65].

In the BOC pulse compressor EM field is concentrated to the cavity surface in the equatorial plane, and also coupling to the waveguide occurs in the same area, so this is the region with larger rf losses. For this reason, two cooling channels have been designed above and below the waveguide, as one can see in Fig.6.24. In order to perform thermo-mechanical simulations, the rf average dissipated power has been calculated. The BOC will be powered by 50 MW Toshiba ET3702 klystron with pulse duration is 1.5 μs and repetition rate 100 Hz 3.2. So the average power from the klystron is equal to 7.5×10^3 W. The dissipated power is equal to the difference between the average klystron power and the output average power. Output power has been calculated numerically by the integration of the output rf pulse Fig.6.23. Total output power from the pulse compressor is $\approx 5.9 \times 10^3$ W, so dissipated power is equal to 1.6×10^3 W.

The ANSYS simulated structure is given in Fig.a)6.24. With respect to the mechanical drawing we have considered a simplified model of the structure with symmetric cooling channels with circular cross section. The cooling water temperature was set to 22° C. Maximum temperature increase occurred on coupling slots, as expected, with an increase up to $\approx$ 25.5° C 6.25.

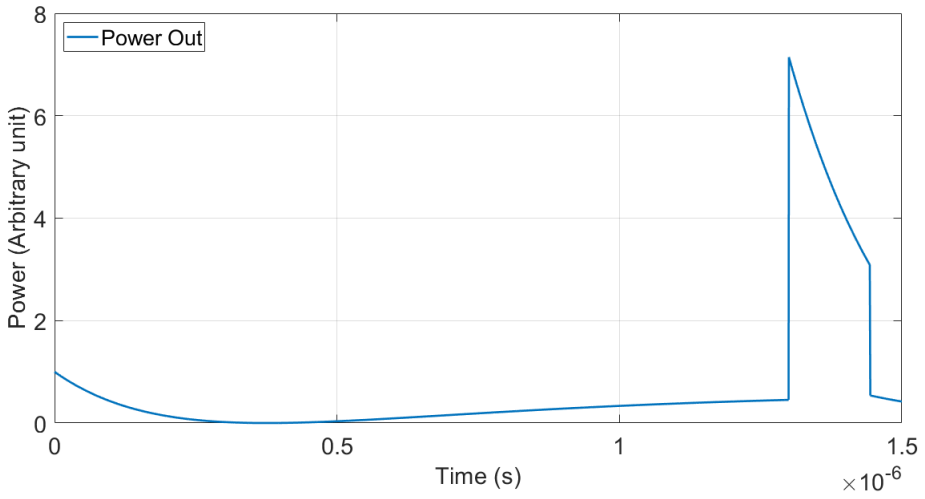

Figure 6.23. Output power from the BOC pulse compressor.

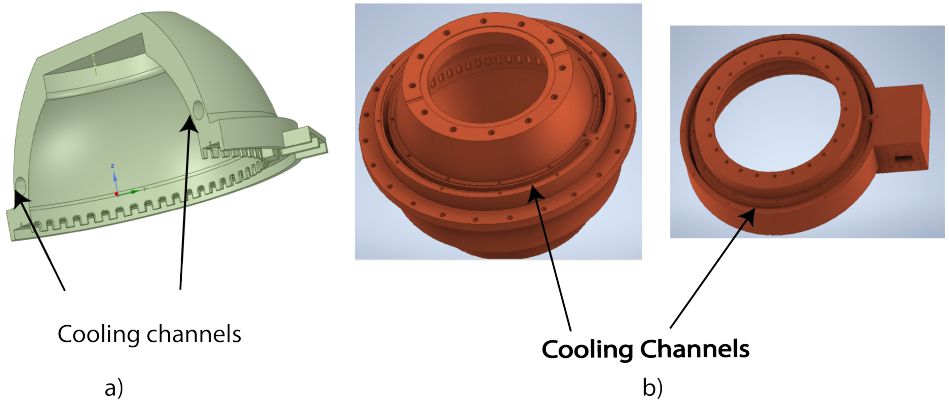

Figure 6.24. a) Cooling channel of the simplified simulation geometry, half symmetry, b) Cooling channels of final 3D mechanical drawing.

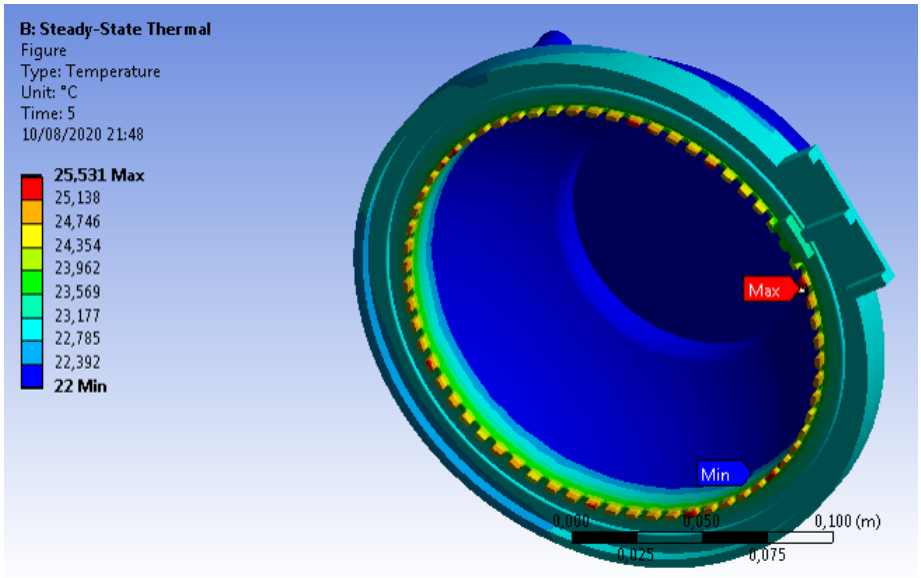

Figure 6.25. Temperature distribution on the BOC pulse compressor.

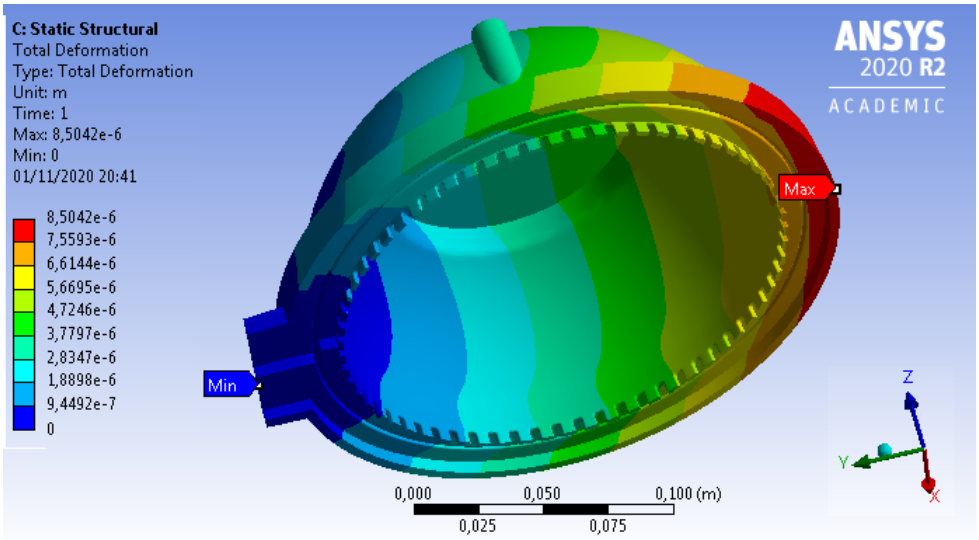

Figure 6.26. Deformation of the BOC pulse compressor due to heating.

The temperature distribution has then been imported in the structural analysis module and the deformations have been calculated. The results are given in Fig.6.26. From the plot it is possible to note that the deformations are within a range of $10\mu m$. This deformed structure has then been imported back in the ANSYS HFSS module to study the variation in the resonant frequency and cavity response. The results are given in Fig. 6.27 and 6.28 and put in evidence that, in our case, the shift of the resonant frequency and detuning is minimal and can be easily corrected with water cooling.

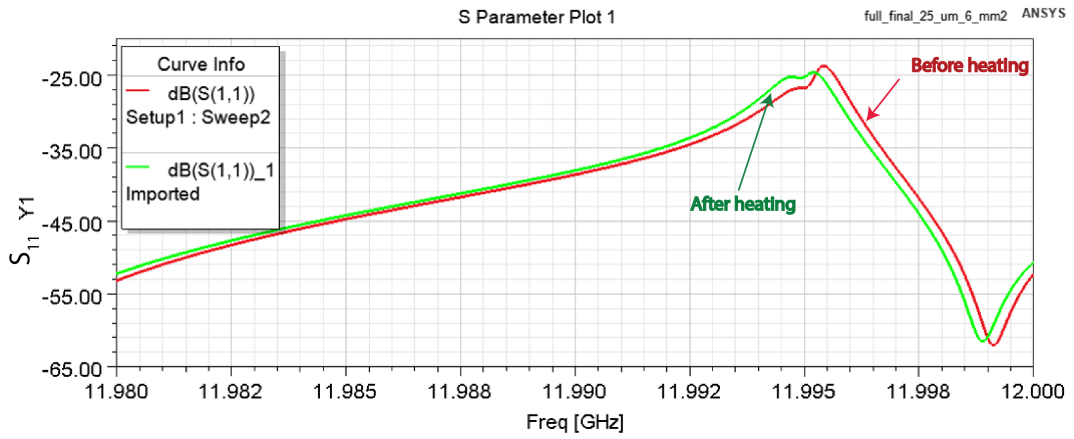

Figure 6.27. S_{11} without dissipated power and with rf dissipation.

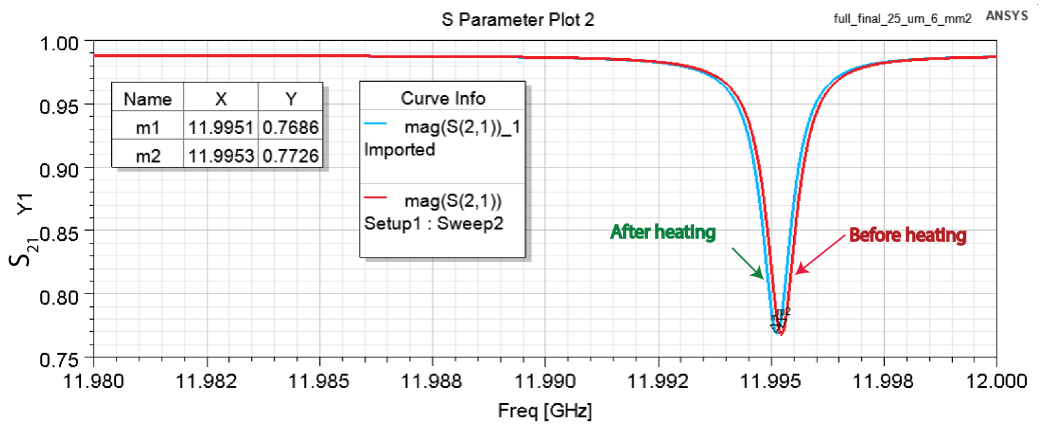

Figure 6.28. S_{21} without dissipated power and with rf dissipation.

6.5 Mechanical design

The mechanical design of the structure has been performed with the commercial CAD code Autodesk Inventor [13] and it is illustrated in Fig.6.32.

The structure consists from two main parts: the body of the cavity with half of the waveguide Fig. a)6.29 and waveguide with the bend Fig. b)6.29. Fig.6.10 shows the middle plane cut of the the bend and the waveguide.

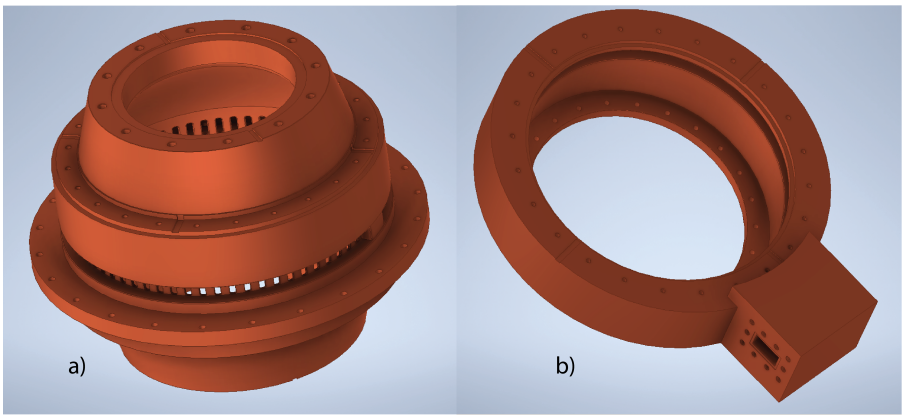

Figure 6.29. Middle plane cut: waveguide and bend.

These two parts are joined to each other with two aluminum gaskets and fasteners. Fig.6.31 shows the positions of the cooling channels, gaps, aluminum gaskets and fasteners. The aluminum gaskets are not exposed to RF.

The structure can be completely disassembled and assembled again changing the gaskets. Moreover, if necessary tuning rings can be inserted to precisely tune the resonant frequency with a progressive machining. The structure can be, in this case, disassembled, machined, cleaned, and assembled again. The vacuum sealing in the structure is assured by aluminum gaskets that are clamped between the different parts.

Fig.6.32 shows the full 3D model of the system.

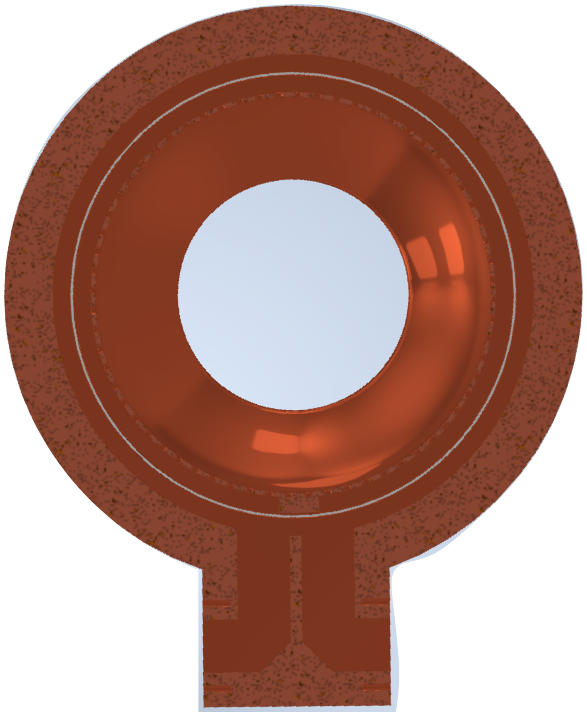

Figure 6.30. Middle plane cut: waveguide and bend.

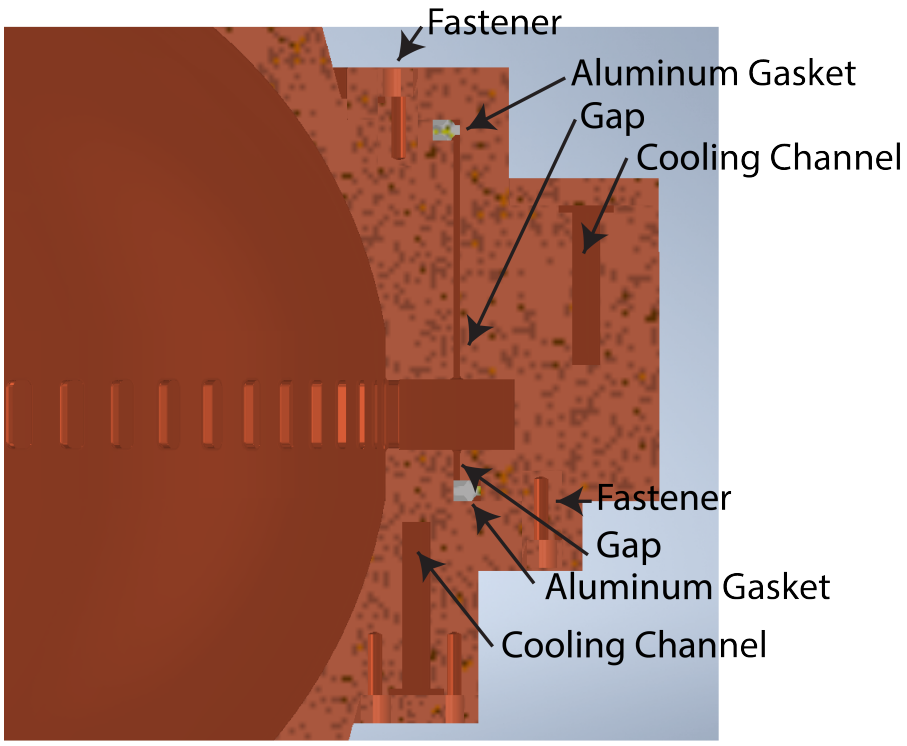

Figure 6.31. Transverse plane cut.

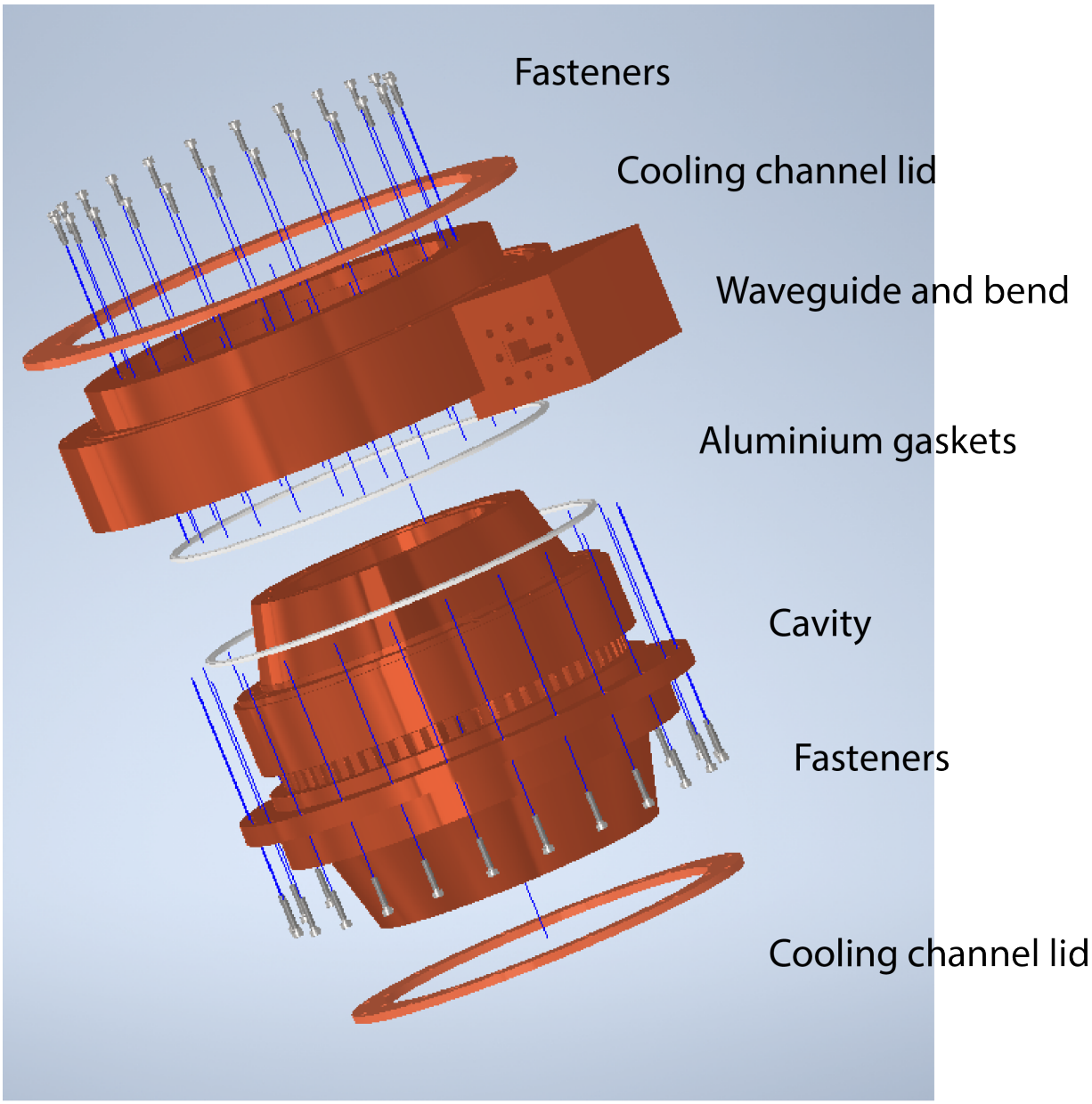

Figure 6.32. 3D mechanical model.

Chapter 7

BOC Pulse Compressor Design for Standing Wave RF structures

As already illustrated, pulse compressors are typically used to increase the RF peak power in TW accelerating structures. In the following we will illustrate another possible type of application related to the feeding of SW structures

7.1 Applications of BOC pulse compressors for feeding SW RF structures

SW cavities are typically feed through circulators (or isolators) in order to protect the klystron from the reflected power during RF transients (or even at regime in the case of coupling coefficient not equal to 1). Commercially, circulators are available at different frequencies, as example in L or S band, but they are not available at higher frequencies as in the case of C or X band because of the difficulties to use ferrites (typically used as non-reciprocal materials in such devices) at this high frequency (mainly due to their high dissipation and rf properties at this frequencies). A possible scheme to avoid the use of circulators for SW cavities powering is given in Fig.7.1.

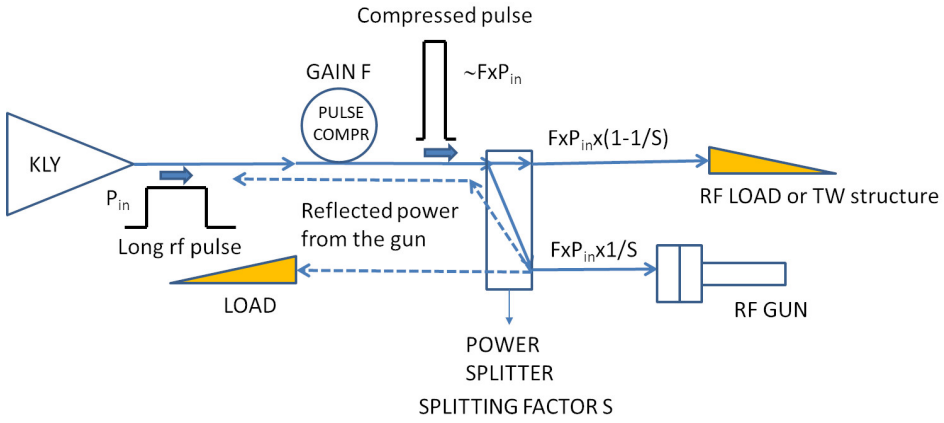

Figure 7.1. Possible scheme to avoid the use of circulators for SW cavities powering.

The rf pulse from the klystron is compressed through the use of a pulse compressor by a factor F and the power is then splitted by a power splitter by a factor S. The reflections from the SW structure back to the klystron are then reduced by a factor F/S^2 because of the presence of the power splitter itself. Moreover, the reflected pulse has a short time duration, resulting in an overall acceptable reflection back to the klystron itself if the system is properly designed. This scheme obviously works in the case of SW structures designed to be fed with short RF pulses, compatibly with the compressed RF pulse. The residual power from the splitter and more precisely a factor $(1 - 1/S)$ can be either dissipated into a rf load or, more conveniently, used to feed another TW cavity (that hasn't reflections). Another interesting application is in the possibility to use low peak power, long rf pulses klystrons to feed SW structures with short rf pulses. This can have also the advantage to reduce the required output power from the source keeping under control all the breakdown phenomena related to the use of long rf pulses (that scales at the fifth power of the rf pulse length [80]. In particular, as illustrated in the following, we have optimized the BOC pulse compressor system for a new RF gun working in C band (5.712 GHz).

7.2 RF photo-guns

RF Photo-guns[113] are electron sources widely used in modern facilities and find applications as injectors for FELs, THz and Compton sources and electron diffraction[29, 59, 63, 82, 112, 121] allowing reaching very high beam brightness. A laser pulse of a suitable wavelength extracts the electrons from a cathode embedded in an RF cavity called RF Gun. An external RF power source excites the cavity accelerating mode so that the photo-electrons are immediately accelerated by the RF electric field on the cathode and all along the gun beam axis [84, 95, 107, 149]. Under the combined action of the RF accelerating field and of an external solenoidal magnetic field the dynamics of the electron beam is guided and controlled, and low-emittance high-brightness bunches are produced and injected in the energy boosters placed downstream [83, 93]. Its basic layout is given in Fig.7.2

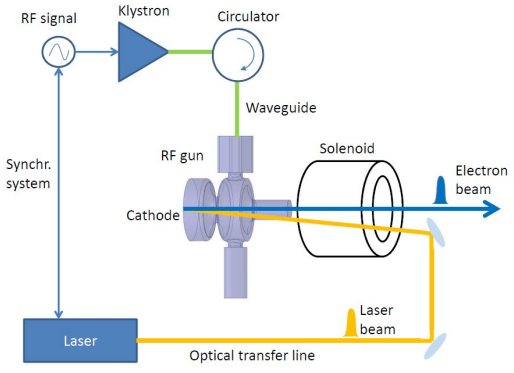

Figure 7.2. Basic layout of the RF gun injectors.

Presently, the RF technology mostly used for RF Guns is the S-band ($f_{RF} = 3\ GHz$). The S-band is used, in particular, for facilities operating at low rep rate ($f_{rep} \leqslant 120Hz$), while lower frequency technologies (L-band, VHF) are used for

higher rep rates. According to beam dynamics studies, the higher is the peak electric field on the cathode, the better is the quality of the beam emerging from the gun. In this respect the S-band represents the state-of-the-art, providing typical peak fields of $\approx$ 120 MV/m on the cathode. Even taught larger values would be very much desirable to further improve the beam quality, it was found experimentally to be very difficult to go beyond 120 MV/m in S-band based injectors. The limitation comes from the unacceptable increase of the RF breakdown rate (BDR) and required input power. Breakdown is a complex phenomenon which depends on many aspects, such as conditioning time and strategy, construction quality, surface cleanliness, residual pressure. However, dedicated studies pointed out that, at the best, the BDR depends ultimately on the operational peak values of the surface electric and magnetic fields and on the RF pulse duration[80].

Recently the idea to implement rf guns operating in C-band RF ($f_{RF} = 5.712$ GHz) have been developed. C band is a more recent technology whose reliability and effectiveness have been already fully demonstrated. Successful FEL radiation facilities such as SwissFEL[141] in Switzerland and SACLA [140] in Japan are based on linacs made of travelling wave C-band accelerating sections. The technology is also industrially mature, since power sources and the needed ancillary components (driver amplifiers, waveguides, ceramic windows, dummy loads, LLRFs, etc..) are all available on the market. However, beam injectors fully based on this technology have not been developed yet. There are solid reasons to believe that the frequency step-up from S-band to C-band can provide an improvement of the photo-injector beam quality. This is mainly related to the filling time reduction in case of standing wave cavities, corresponding to an RF pulse duration shortening, which scales as $f^{-3/2}$, and to the increase of the RF structure efficiency (the shunt impedance per unit length) which scales as $f^{1/2}$ and allows saving RF power to reach the design peak field. In particular in the framework of the XLS-Compact Light design study[58] and of the EuPRAXIA@SPARC_LAB proposal[71] a new SW gun has been proposed. The strategy for its design is reported in [36],[55]. The electromagnetic model of the gun is given in Fig.7.3.

It is a 2.5 cell rf device fed with short RF pulses ($\tau < 300ns$) at 18 MW and the coupling with the input waveguide is axial, through the last iris, with a mode launcher [108]. These two implementations (short RF pulses and mode launcher) allow to contemporary reduce the pulsed heating (that scale with the square root of the RF pulse length), the breakdown rate (that scales with τ^5), the average dissipated power and the surface magnetic field on the input coupler. The achievable cathode peak field at this level of power is 160 MV/m while the main gun parameters are reported in Tab7.1.

7.3 Optimization of the BOC to feed the C band gun

The C band gun is a SW cavity. As already pointed out there are two possible feeding. The typical system foresees the use of an isolator. Commercial isolator working in C band are produced by one company [5], but their reliability at this very high power (18 MW peak field) has to be experimentally demonstrated. As example the profiles of the input, reflected, dissipated power and cathode peak field

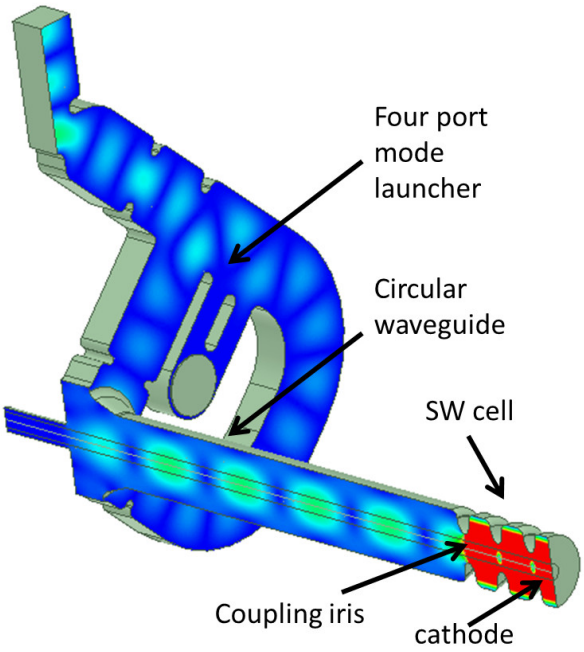

Figure 7.3. Gun geometry simulated by ANSYS-HFSS.

are given in Fig.7.4.

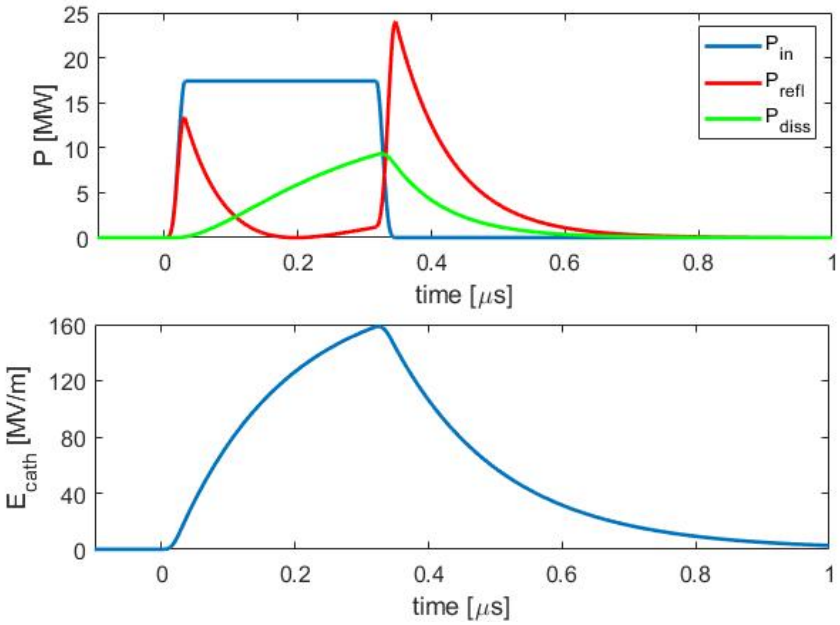

Figure 7.4. Input, reflected, dissipated power (upper plot) and cathode peak field (bottom plot) as a function of time for a 300 ns pulse length with 30 ns rise time.

The other possible solution is the use of a BOC system, as already discussed.

Table 7.1. Main parameters of the C-band gun.

Working frequency [GHz]	5.712
$E_{\text{cath}}/P_{\text{diss}}^{1/2}$ [MV/(mMW$^{1/2}$)]	52
RF input power [MW]	18
Cathode peak field [MV/m]	160
Cathode type	copper
Rep. rate [Hz]	100
Quality factor	11800
Filling time [ns]	164
Coupling coefficient	3
RF pulse length [ns]	300
$E_{\text{surf}}/E_{\text{cath}}$	0.9
Modified Poynting vector [W/μm^2]	2.5
Pulsed heating [°C]	<20
Average diss. Power [W]	230

The sketch of this feeding is given in Fig.7.5

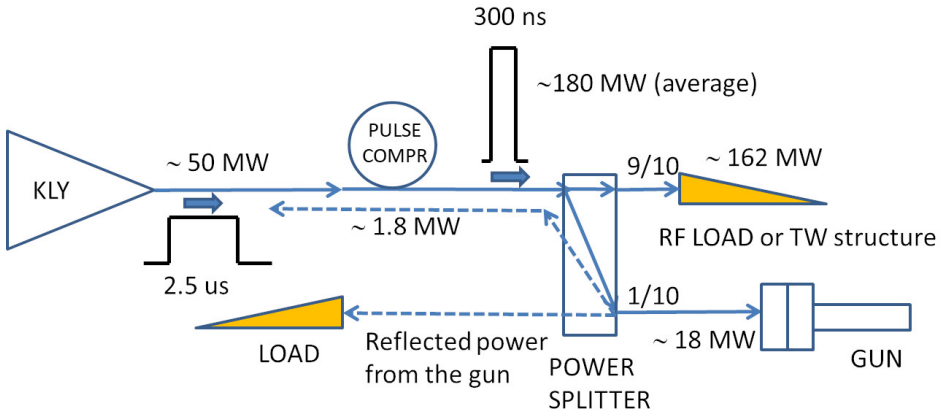

Figure 7.5. Scheme which avoid the use of circulators for SW cavities powering with the main parameters and values.

with few quantities reported in the figure just for reference. Commercial C band klystron and modulators with a 50 MW output power, 2.5 μs rf pulse length, 100 Hz, already exist and have been, as example used for all C band station in operational at SwissFEL[141]. The quality factor of a BOC pulse compressor that is possible to achieve is of the order of 210000. This BOC system has been already designed for the C band TW modules of the SwissFEL[150]. The power can be reasonably amplified by the BOC by a factor $F = 3 - 4$ (average power) in 300 ns rf pulses and then splitted by a factor $S = 10$, after the BOC. A fraction $1/S = 10\%$ of the power is then send to the rf gun and the other part $(1 - 1/S) = 90\%$ can be, as example, used to feed a C band TW accelerating structures. The reflected power back to the klystron has, in this case, an average value of $F/S^2 = (3 - 4)\%$ the klystron output power.

Our goal has been to optimize the BOC parameters in term of external quality factor (or coupling coefficient) and phase jump time (t_f) in order to achieve the maximum cathode peak field in the gun thus maximizing the factor F. A maximization of this factor F allow to increase the splitting factor S and then reduce the reflected power to the klystron that scales as S^2.

To this purpose a MATLAB code has been developed. Field reflected from the cavity is described be the following equation [67]:

$$T_c \frac{dE_e}{dt} + E_e = -\alpha E_i \tag{7.1}$$

Where T_c in this case a filling time for the SW structure, E_e reflected field from the coupling aperture of the structure, $\alpha = 2\beta/(1+\beta)$ where β is coupling of the structure and E_i is the field from the power source. In our case, E_i is the output field from the BOC pulse compressor 7.2, 7.3, 7.4.

$$E_{out}(0 \leqslant t < t_f) = \alpha \left(1 - e^{-t/T_c}\right) - 1 \tag{7.2}$$

$$E_{out}(t_f \leqslant t \leqslant t_e) = \alpha[(2 - e^{-t_f/T_c})e^{-(t-t_f)/T_c} - 1] + 1 \tag{7.3}$$

$$E_{out}(t > t_e) = \alpha[(2 - e^{-t_f/T_c})e^{-(t_e-t_f)/T_c} - 1]e^{-(t-t_e)/T_c} \tag{7.4}$$

Eq.7.1 has been solved numerically in MATLAB and E_e has been calculated. Once E_e is solved, we can calculate the dissipated power in the SW structure $P_{diss} = E_e^2/Q_0$, where Q_0 is the unloaded quality factor of the SW structure. On the other hand cathode peak field of the rf-gun is $E_{cath} = 52 * P_{diss}^{1/2}$. In this way cathode peak fields for different coupling coefficient and phase jump time have been calculated.

As an example in Fig.7.6 we report the behavior of the cathode peak field for six different coupling coefficient supposing t_f is kept the same and equal to $t_f = 2.3\ \mu s$. The cathode peak field normalized to the square root of the input power from the klystron as a function of the phase jump time (t_f) and for different coupling coefficients is given in Fig.7.7, while Fig.7.8 shows the rf power after the BOC.

From the plot it is clear that, the increase of the coupling coefficient of the BOC, allows to increase the cathode peak field. Considering extremely large coupling coefficients (> 12-14) mean that the coupling holes on the BOC have to be strongly increased with a consequent possible difficulty in BOC realization and structural problem in its construction. The plot clearly shows also that the cathode field saturate at larger coupling. Assuming a reasonable value of the BOC coupling coefficient equal to 12 with a phase jump time (t_f) at 2.2 μs we have that $E_{cath}/\sqrt{P_{in}}$ is equal to 80 MV/(m$MW^{1/2}$) and we can adopt, in the final feeding scheme, a splitter with a splitting factor $S = 12.5$ obtaining a cathode peak field exactly equal to 160 MV/m and a peak reflected power to the klystron equal to $\sim 340MW/S^2 \sim 2$ MW that can be considered a reasonable value of the reflected power also because of the very short pulse duration.

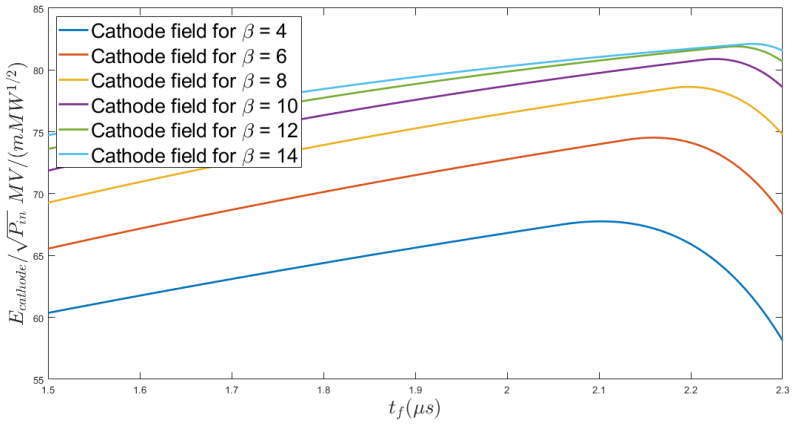

Figure 7.6. The cathode peak field as a function of the phase jump time (t_f) and for different coupling coefficients.

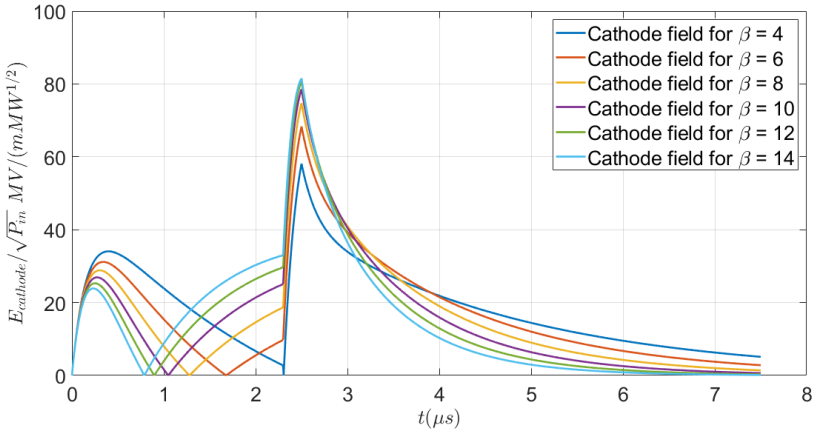

Figure 7.7. Cathode peak fields for six different coupling coefficient.

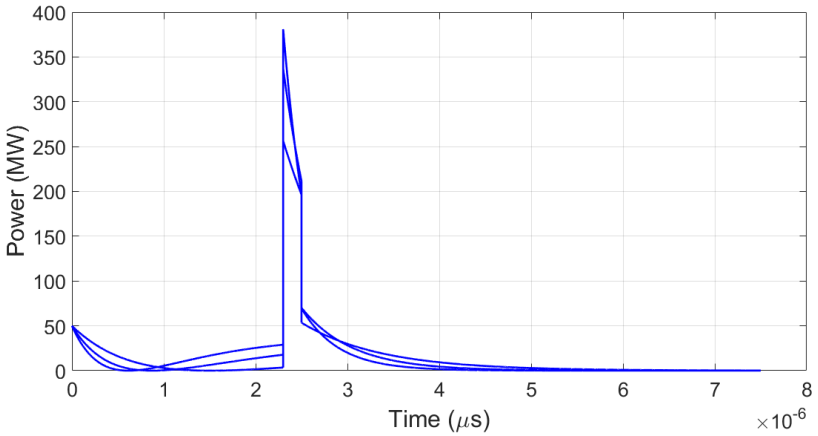

Figure 7.8. Power output from the BOC for $\beta = 6, 10, 14$.

7.4 Design of the C band BOC with large coupling coefficient

According to the final results of the optimized BOC parameters, we have performed an electromagnetic design of the cavity to investigate the possibility to obtain a cavity with a coupling coefficient larger than 12 and a quality factor $Q_0 \approx 210000$. To this purpose, following the results already obtained by [151], we have chosen the mode $TM_{18,1,1}$. As in the case of the X band cavity, the design of the BOC has been performed in ANSYS HFSS [12].

The first step has been the tuning of the resonant frequency by changing the dimensional parameters a and r_0 of Fig.4.3 following the same procedure already illustrated in the previous paragraphs for the X-band BOC. Because of the mode azimuthal dependence, we have simulated a small angle of the total structure (more precisely $360°/36 = 10°$) with perfect electric boundary conditions. The final result has been a Q_0 factor equal to 210500.

The coupling with the waveguide has been obtained with a procedure similar to those illustrated in the previous paragraph but now referred to the C band waveguide and BOC. The sketch of the structure with the waveguide and coupling holes is given in Fig.7.9. The waveguide height b has been fixed equal to the height of the

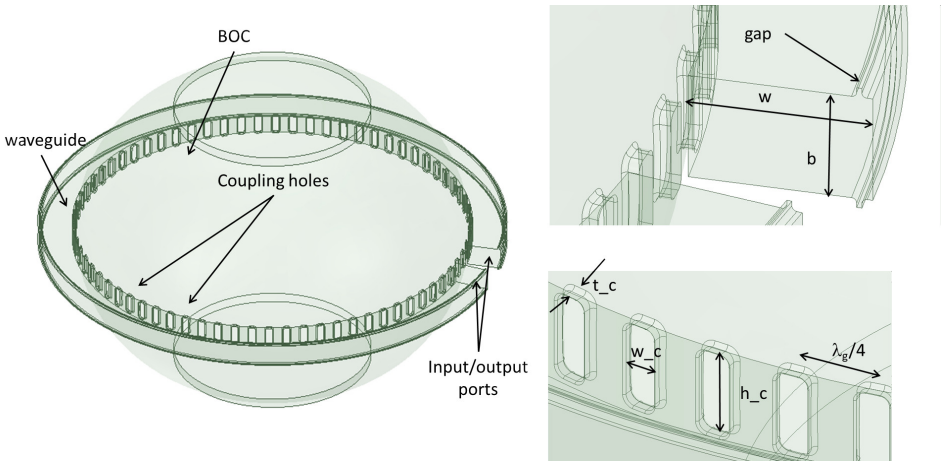

Figure 7.9. Full geometry of the BOC and it's main parameterized dimensions.

standard C band waveguide WR187 and equal to 22.15 mm while the waveguide width (w) has been tuned to have a waveguide wavelength (λ_g) equal to four times the distance between the coupling holes, as already has been illustrated in the X band case. The wall thickness between the waveguide and the cavity (t_c) has been fixed equal to 3 mm to have a reasonable structural consistency of this part of the cavity with coupling holes. According to what already discussed, to have the possibility to fabricate the structure without brazing, a gap has been opened on the surrounded waveguide.

The design has been oriented to contemporary obtain a coupling coefficient larger than 12 at the right resonant frequency of 5.712 GHz. To this purpose, as done for the X band case, for a given dimension of the holes w_c and h_c, the mode frequency has been re-tuned by acting on the parameters a and r_0 and simulating the geometry

given in Fig.7.10 with the HFSS eigenmode solver.

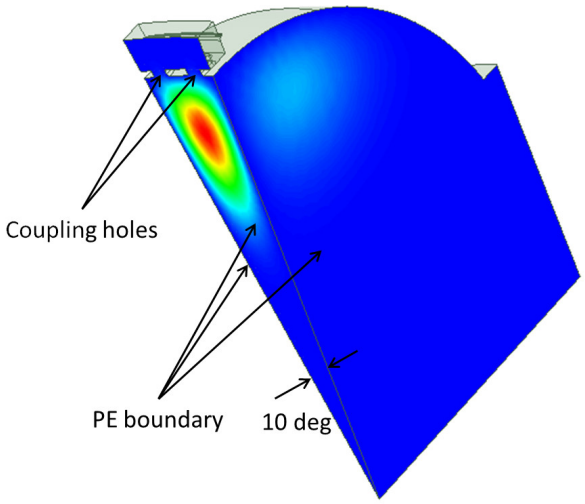

Figure 7.10. Eigen mode simulations of the slice, with slice angle and boundaries.

This geometry takes into account the frequency shift due to the holes. Then the waveguide width (w) has been calculated according to Eq.6.3. The complete structure reported in Fig.7.11 (without the input splitter) has then been simulated with the HFSS driven mode solver to calculate the reflection and transmission coefficients and, from this last one, the final coupling coefficient. Because of the symmetry of the mode we have simulated one half of the structure with a PE boundary condition.

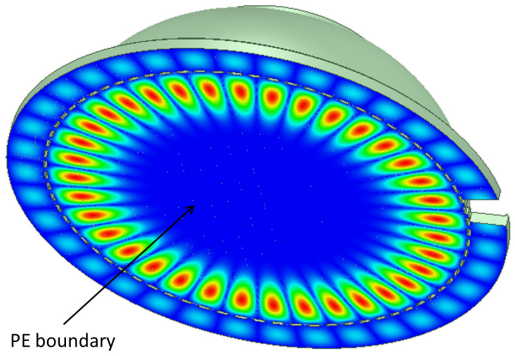

Figure 7.11. Electric field inside the simulated half geometry, bottom is perfect E boundary.

Simulations with different waveguide w widths starting from the theoretical value reported in Eq.6.3, have then be done to maximize the coupling coefficient and minimize the reflections back to the source, as already discussed in the previous chapter. The final obtained BOC dimensions and parameters are given in Tab. 7.2. The final magnitude of the electric field at the resonant frequency is shown Fig.7.11. The reflection and transmission coefficients are given in Fig.7.12 and Fig. a) 7.13

the transmission coefficient reported on the smith chart Fig. b) 7.13 clearly shows the overcoupling. From the transmission coefficient we have calculated a coupling coefficient $\beta = 13.3$.

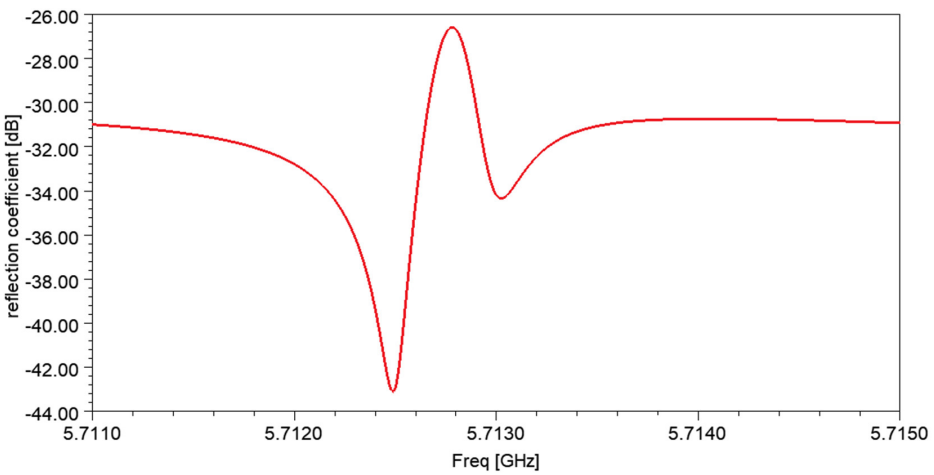

Figure 7.12. S_{11} reflection coefficient of the BOC.

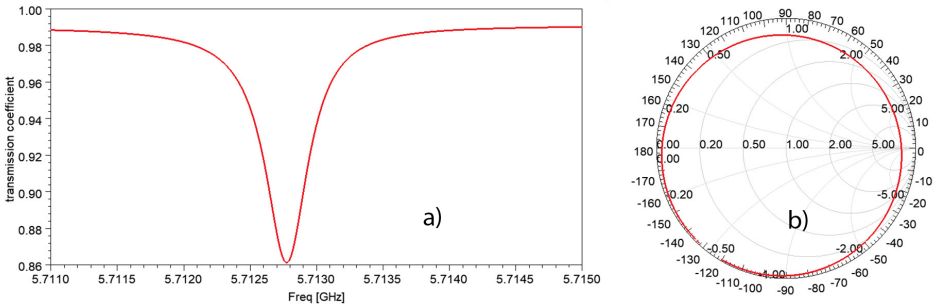

Figure 7.13. a) S_{21} transmission coefficient of the BOC, b) S_{21} smith chart.

Table 7.2. Final C band BOC parameters.

Working frequency	5.712 GHz
Q_0	210500
β	13.3
a	199.70 mm
r_0	147.00 mm
w	35.17 mm
b	22.15 mm
w_c	7 mm
h_c	19 mm
t_c	3 mm

Chapter 8

Conclusions and perspectives

In the present thesis work two different design of a BOC type pulse compressor system have been developed. They have been developed for the EuPRAXIA@SPARC_LAB and CompactLight-XLS projects. In the EuPRAXIA@SPARC_LAB project, the linac has to provide an energy gain of ≈ 1 GeV in 15 m of active length while, for CompactLight-XLS, the linac has to provide ≈ 5.2 GeV in 83 m of active length. The linacs are based on traveling wave structures operating on the $2\pi/3$ mode, fed by klystrons and pulse compressors systems.

The first BOC cavity has been designed, in particular, for the X band accelerating module of EuPRAXIA@SPARC_LAB. The design of the cavity has been done using analytical and finite element simulation codes. Considering the required parameters for the optimal performance of the linac, the BOC cavity operating mode has been the $TM_{16,1,1}$, with a theoretical $Q_0 = 143\ 000$ unloaded quality factor.

The electromagnetic coupling between the cavity and the waveguide has been obtained by means of 62 coupling slots. The coupling slot's dimensions have been optimized, to obtain an optimum coupling factor equal to 7.8. The wall thickness was set 2 mm, to avoid structural weakening of the cavity. To allow the realization of the structure with the LNF-INFN brazing free technology, a gap in the waveguide has been introduced. The gap has been optimized. Its width was reduced to 1mm, to reduce electric field penetration inside the gap itself and field magnification. Moreover, to overcome the electric field increase due to the gap, two roundings of 0.5 mm were added at the gap edges. Alternative solutions for the position of this gap have also been illustrated. As a final step waveguide width has been optimized analytically and numerically, together with the coupling slots and the bend. The system has been optimized to have reflections as low as $S_{11} < -25\ dB$.

Sensitivity studies have been carried out. If the temperature change of the cooling water of the BOC system is $+/-5$°C the range of tunability is 1 MHz. If there is no mechanical mechanism of tuning, the calculated required precision is $7/\mu m$.

A mechanical design of the structure has then been performed in combination with thermal analysis. Firstly, the total average dissipated power in the BOC has been evaluated to be equal 1.6×10^3 W. With this value structure's thermal expansion and deformations have been calculated by the simulation code ANSYS Workbench. The effect of thermal expansion on the scattering parameters of the

system has finally been studied. Simulations showed that two cooling channels above and bottom of the waveguide can efficiently remove the generated heat keeping under control the resonant frequency and compressor performances under powering.

Finally, mechanical drawings of the BOC have been done, the system consists of two main parts, the cavity body and the waveguide with the bend. The cooling channels will be covered with special lids and the whole structure was designed to be assembled only with gaskets and fasteners. The new design we proposed with the possibility to fabricate a clamped device has several advantages. First of all, the realization does not require expensive processes in vacuum furnaces with a potential reduction of the realization cost. The use of hard copper instead of annealed one allows to obtain, in principle, even better performances at high power. With this technology it is also possible to open the structure, machine it to reach the desired resonant frequency, and close it again with a reduction of the required precision in the fabrication of the device and cost.

The second BOC-type pulse compressor has been designed for a possible feeding system of a C band gun. Simulations showed that it is possible to optimize the BOC pulse compressor for feeding the C band rf-gun foreseen for the CompactLight-XLS project. Quality factor was fixed to 210000 as for SwissFEL's BOC, but in our case the β has to be be equal to (at least) 12. In particular, a dedicated code has been written to optimize the BOC cavity parameters in term of coupling coefficient and phase jump time. This code can be applied to all feeding systems that foresee the use of a pulse compressor to feed a SW cavity. In our case the optimum phase jump time was found to be $t_f = 2.2\ \mu$ with a β as large as 12. In the rf gun feeding system we have proposed, after the BOC a power splitter allow to feed the gun reaching the desired value of 160 MV/m on the cathode while reflections back to the klystron will be reduced at about ~ 2 MW, which is a reasonable value of the reflected power also because of the very short pulse duration (300 ns). The BOC e.m. design has been also done and a Q_0 factor of the BOC equal to 210500, with a $\beta = 13.3$ have been obtained. Also for this design brazeless geometry has been realized can be adopted.

This thesis work represents the first step toward the realization of two different type of BOC-type pulse compressors with the new brazeless technology developed at LNF-INFN. These devices are fundamental in the EuPRAXIA@SPARC_LAB project, with particular reference to the X-band BOC. In EuPRAXIA@SPARC_LAB up to 10 of this compressors will be necessary. Other working mode for the BOC cavity can be also considered (with $m > 16$) because the procedure to design this type of structures is now well identified and clear. Also the mechanical drawing we have implemented is completely parameterized and can be adapted to different working modes. The next step will be the realization, low and high power test of a first prototype.

Appendix A

The 3-dB directional Coupler

For operation of SLED, an essential element is 3-dB directional coupler, which directs power reflected from the resonant storage cavities away from the source and towards to a load. A directional coupler is a four-port microwave junction with the following characteristics: If power is incident on one port, that power is coupled out through two of other ports, but not through the remaining one. Furthermore, there is no reflection at any input port when the other ports are all terminated by their matching characteristics impedance [109] .

Figure A.1. The 3-dB coupler.

Power incident on port 1 or port 3 is equally distributed between ports 2 and 4. Likewise, power incident on port 2 or port 4 is equally distributed between ports 1 and 3. Ports 1 and 3 are uncoupled, as are ports 2 and 4, so we don't have energy flow between 1 and 3 and 2 and 4. Scattering matrix for a 3-dB coupler is:

$$S = \frac{1}{\sqrt{2}} \begin{pmatrix} 0 & 1 & 0 & i \\ 1 & 0 & i & 0 \\ 0 & i & 0 & 1 \\ i & 0 & 1 & 0 \end{pmatrix}$$

Lets assume power fed to the port one is scaled to 1, then output power is given

by

$$\frac{1}{\sqrt{2}}\begin{pmatrix}0 & 1 & 0 & i\\ 1 & 0 & i & 0\\ 0 & i & 0 & 1\\ i & 0 & 1 & 0\end{pmatrix}\begin{pmatrix}1\\0\\0\\0\end{pmatrix}=\frac{1}{\sqrt{2}}\begin{pmatrix}0\\1\\0\\i\end{pmatrix}$$

Now the load on each output port reflects the wave with a factor which is previously designated as E_{out}. These reflected waves become new inputs for ports 2 and 4. Assuming mechanical symmetry, so that they pick up no additional phase difference in this reflection, we finally get as output.

$$\frac{1}{\sqrt{2}}\begin{pmatrix}0 & 1 & 0 & i\\ 1 & 0 & i & 0\\ 0 & i & 0 & 1\\ i & 0 & 1 & 0\end{pmatrix}E_{out}\frac{1}{\sqrt{2}}\begin{pmatrix}1\\0\\0\\0\end{pmatrix}=E_{out}\frac{1}{\sqrt{2}}\begin{pmatrix}0\\0\\i\\0\end{pmatrix}$$

Thus reflected waves cancel at port 1 and combine at port 3, assumed matched to a transmission network, and the power directing function of the coupler is accomplished. It can be seen that if the two cavities are completely the same, the reflected waves will cancel at port 1 and combine in at port 3. The power is successfully directed away from the klystron source and directed to accelerating structure.

Appendix B

Equivalent Circuit Model

A resonant cavity is a non-matched load for a waveguide or a transmission line, and can be modeled as an RLC parallel circuit. The voltage source refers to the RF generator. The cavity impedance is equal to:

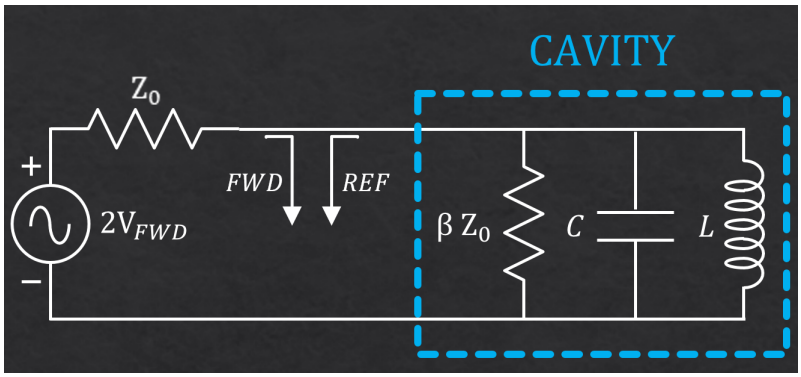

Figure B.1. An equivalent circuit model of the SLED.

$$\frac{1}{Z_{cav}} = \frac{1}{\beta Z_0} + \frac{1}{i\omega L} + i\omega C \tag{B.1}$$

After the simplification, we will have

$$Z_{cav} = \beta Z_0 \frac{i\omega LC}{(i\omega)^2 \beta Z_0 LC^2 + i\omega LC + \beta Z_0 C} \tag{B.2}$$

If we recall that

$$\omega^2 = \frac{1}{LC}, \quad Q_0 = \omega_0^2 \beta Z_0 C, \quad Q_L = \frac{Q_0}{1+\beta} \tag{B.3}$$

And after even more simplification, we will have

$$Z_{cav} = \beta Z_0 \frac{i\omega/Q_0\omega_0}{(i\omega)^2/\omega_0^2 + i\omega/Q_0\omega_0 + 1} \tag{B.4}$$

An RF wave travelling from the generator toward the cavity is always partially reflected at the cavity input. The reflected wave can be calculated according to [54]:

$$V_{REF} = V_{FWD} \frac{Z_{cav} - Z_0}{Z_{cav} + Z_0} \tag{B.5}$$

If we insert B.4 into B.5 we will have:

$$V_{REF} = V_{FWD}\left(\underbrace{\frac{2\beta}{\beta+1}}_{\text{coupl. coeff.}} \cdot \underbrace{\frac{(i\omega)/\omega^2 Q_L}{((i\omega)/\omega_0)^2 + (i\omega)/\omega_0 Q_L + 1} - 1}_{\text{network transfer function}}\right) \tag{B.6}$$

Depending on the value of β three different situations may occur: $\beta < 1$ under-coupling, $\beta = 1$ critical-coupling, $\beta > 1$ over-coupling.

Bibliography

[1] *APS website*. URL https://www.aps.anl.gov/.

[2] *BEPC II website*. URL http://english.ihep.cas.cn/doc/1840.html.

[3] *CHESS website*. URL https://www.chess.cornell.edu/.

[4] *CLEAR Website*. URL https://clear.cern/clear.

[5] *CML company website*. URL https://www.cmlengineering.com//.

[6] *CompactLight website*. URL https://www.compactlight.eu/Main/HomePage.

[7] URL http://hyperphysics.phy-astr.gsu.edu/hbase/Tables/rstiv.html.

[8] *DAΦNE website*. URL http://w3.lnf.infn.it/accelerators/dafne/?lang=en.

[9] *ELI-NP Website*. URL https://www.eli-np.ro/.

[10] *ESRF website*. URL https://www.esrf.eu/.

[11] *EuPRAXIA website*. URL http://www.eupraxia-project.eu/.

[12] *ANSYS HFSS website*. URL http://www.ansys.com/products/electronics/ansys-electronics-desktop.

[13] *Autodesk Inventor website*. URL https://www.autodesk.com/products/inventor/overview.

[14] *CPI Website*. URL https://www.cpii.com/.

[15] *LCLS website*. URL https://lcls.slac.stanford.edu/.

[16] *PETRA III website*. URL https://photon-science.desy.de/facilities/petra_iii/index_eng.html.

[17] *PAL-XFEL website*. URL http://pal.postech.ac.kr/paleng/.

[18] *SPARC_LAB Website*, . URL http://w3.lnf.infn.it/lab/sparc_lab/.

[19] *SPring-8 website*, . URL http://www.spring8.or.jp/en/.

[20] *SuperKEKB website*. URL http://www-superkekb.kek.jp/.

[21] *What is virtual leak?* URL https://www.mtm-inc.com/av-20100312-vacuum-chamber-design-what-is-a-virtual-leak.html.

[22] *Physics 575 – Accelerator Physics and Technologies for Linear Colliders* . URL https://hep.uchicago.edu/~kwangje/LectureNotes_WangPartI.pdf.

[23] *European XFEL website*. URL https://www.xfel.eu/index_eng.html.

[24] *Linac Coherent Light Source (LCLS) design study report*. SLAC, Stanford, CA, 1998. URL https://cds.cern.ch/record/361716.

[25] BEPC II: construction and commissioning. *Chinese Physics C*, 33(S2):60–64, jun 2009. doi: 10.1088/1674-1137/33/s2/016. URL https://doi.org/10.1088%2F1674-1137%2F33%2Fs2%2F016.

[26] Sparclab present and future. *Nuclear Instruments and Methods in Physics Research Section B: Beam Interactions with Materials and Atoms*, 309:183 – 188, 2013. The 5th International Conference.

[27] High-gradient structures and rf systems for high brightness-electron linacs. *PHD thesis*, 2020.

[28] R. Abela, A. Aghababyan, M. Altarelli, C. Altucci, G. Amatuni, P. Anfinrud, P. Audebert, V. Ayvazyan, N. Baboi, J. Bähr, V. Balandin, R. Bandelmann, J. Becker, B. Beutner, C. Blome, I. Bohnet, A. Bolzmann, C. Bostedt, Y. Bozhko, and R. Romaniuk. *XFEL: The European X-Ray Free-Electron Laser - Technical Design Report*. 07 2006. ISBN ISBN 978-3-935702-17-1. doi: 10.3204/DESY_06-097.

[29] R. Akre, D. Dowell, P. Emma, J. Frisch, S. Gilevich, G. Hays, P. Hering, R. Iverson, C. Limborg-Deprey, H. Loos, A. Miahnahri, J. Schmerge, J. Turner, J. Welch, W. White, and J. Wu. Commissioning the linac coherent light source injector. *Phys. Rev. ST Accel. Beams*, 11:030703, Mar 2008. doi: 10.1103/PhysRevSTAB.11.030703. URL https://link.aps.org/doi/10.1103/PhysRevSTAB.11.030703.

[30] D. Alesini, S. Bertolucci, M. Biagini, C. Biscari, R. Boni, M. Boscolo, M. Castellano, A. Clozza, G. D. Pirro, A. Drago, A. Esposito, M. Ferrario, V. Fusco, A. Gallo, A. Ghigo, S. Guiducci, M. Incurvati, P. Laurelli, C. Ligi, F. Marcellini, M. Migliorati, C. Milardi, L. Palumbo, L. Pellegrino, M. Preger, P. Raimondi, R. Ricci, C. Sanelli, F. Sgamma, B. Spataro, M. Serio, A. Stecchi, A. Stella, F. Tazzioli, C. Vaccarezza, M. Vescovi, C. Vicario, M. Zobov, E. Acerbi, F. Alessandria, D. Barni, G. Bellomo, I. Boscolo, F. Broggi, S. Cialdi, C. DeMartinis, D. Giove, C. Maroli, V. Petrillo, M. Rome', L. Serafini, E. Chiadroni, G. Felici, D. Levi, M. Mastrucci, M. Mattioli, G. Medici, G. Petrarca, L. Catani, A. Cianchi, A. D. Angelo, R. D. Salvo, A. Fantini, D. Moricciani, C. Schaerf, R. Bartolini, F. Ciocci, G. Dattoli, A. Doria, F. Flora, G. Gallerano, L. Giannessi, E. Giovenale, G. Messina, L. Mezi, P. Ottaviani, L. Picardi,

M. Quattromini, A. Renieri, C. Ronsivalle, L. Avaldi, C. Carbone. The sparc project: a high-brightness electron beam source at lnf to drive a sase-fel experiment. *Nuclear Instruments and Methods in Physics Research Section A: Accelerators, Spectrometers, Detectors and Associated Equipment*. ISSN 0168-9002. doi: https://doi.org/10.1016/S0168-9002(03)00943-4. URL `http://www.sciencedirect.com/science/article/pii/S0168900203009434`.

[31] D. Alesini, A. Battisti, M. Ferrario, L. Foggetta, V. Lollo, L. Ficcadenti, V. Pettinacci, S. Custodio, E. Pirez, P. Musumeci, and L. Palumbo. New technology based on clamping for high gradient radio frequency photogun. *Phys. Rev. ST Accel. Beams*, 18:092001, Sep 2015. doi: 10.1103/PhysRevSTAB.18.092001. URL `https://link.aps.org/doi/10.1103/PhysRevSTAB.18.092001`.

[32] D. Alesini, A. Battisti, M. Ferrario, L. Foggetta, V. Lollo, L. Ficcadenti, V. Pettinacci, S. Custodio, E. Pirez, P. Musumeci, and L. Palumbo. New technology based on clamping for high gradient radio frequency photogun. *Physical Review Special Topics - Accelerators and Beams*, 18, 09 2015. doi: 10.1103/PhysRevSTAB.18.092001.

[33] D. Alesini, A. Battisti, M. Bellaveglia, F. Cardelli, A. Falone, A. Gallo, V. Lollo, D. T. Palmer, L. Pellegrino, L. Piersanti, S. Pioli, A. Variola, V. Pettinacci, and L. Palumbo. Design, realization, and high power test of high gradient, high repetition rate brazing-free *s*-band photogun. *Phys. Rev. Accel. Beams*, 21:112001, Nov 2018. doi: 10.1103/PhysRevAccelBeams.21.112001. URL `https://link.aps.org/doi/10.1103/PhysRevAccelBeams.21.112001`.

[34] D. Alesini et al. New technology based on clamping for high gradient radio frequency photogun. *Phys. Rev. ST Accel. Beams*, 18(9):092001, 2015. doi: 10.1103/PhysRevSTAB.18.092001.

[35] D. Alesini et al. High Power Test Results of the Eli-NP S-Band Gun Fabricated with the New Clamping Technology Without Brazing. In *8th International Particle Accelerator Conference*, page THOBB1, 2017. doi: 10.18429/JACoW-IPAC2017-THOBB1.

[36] D. Alesini et al. Design of a Full C-Band Injector for Ultra-High Brightness Electron Beam. In *Proc. 10th International Particle Accelerator Conference (IPAC'19), Melbourne, Australia, 19-24 May 2019*, number 10 in International Particle Accelerator Conference, pages 1979–1982, Geneva, Switzerland, Jun. 2019. JACoW Publishing. ISBN 978-3-95450-208-0. doi: doi:10.18429/JACoW-IPAC2019-TUPTS024. URL `http://jacow.org/ipac2019/papers/tupts024.pdf`. https://doi.org/10.18429/JACoW-IPAC2019-TUPTS024.

[37] U. Amaldi. The importance of particle accelerators. *Europhysics News*, 31: 5–9, 11 2000. doi: 10.1051/epn:2000601.

[38] S. Antipov, R. Kostin, S. Kuzikov, and A. Vikharev. Inexpensive Brazeless Accelerator Prototype. In *Proc. 9th International Particle Accelerator Conference (IPAC'18), Vancouver, BC, Canada, April 29-May 4, 2018*, number 9 in International Particle Accelerator Conference, pages 2528–2530,

Geneva, Switzerland, June 2018. JACoW Publishing. ISBN 978-3-95450-184-7. doi: doi:10.18429/JACoW-IPAC2018-WEPMF068. URL http://jacow.org/ipac2018/papers/wepmf068.pdf. https://doi.org/10.18429/JACoW-IPAC2018-WEPMF068.

[39] J. Arthur, G. Materlik, R. Tatchyn, and H. Winick. The lcls: A fourth generation light source using the slac linac. *Review of Scientific Instruments*, 66(2):1987–1989, 1995. doi: 10.1063/1.1145778. URL https://doi.org/10.1063/1.1145778.

[40] V. Balakin and I. Syrachev. Status VLEPP RF power multiplier (VPM). *Conf. Proc. C*, 920324:1173–1175, 1992.

[41] K. Balewski, R. Rohlsberger, H. Franz, E. Weckert, W. Decking, and W. Brefeld. Petra iii: A low emittance synchrotron radiation source. technical design report. Technical report, 2004.

[42] S. Bartocci et al. Ex-trim. a proposal for a coherent imaging xuv-fel users endstation. Technical report, Tech. rep., INFN-17-18/LNF, 2017.

[43] B. W. Batterman and N. W. Ashcroft. Chess: The new synchrotron radiation facility at cornell. *Science*, 206(4415):157–161, 1979. ISSN 0036-8075. doi: 10.1126/science.206.4415.157. URL https://science.sciencemag.org/content/206/4415/157.

[44] F. Bisesto, M. Anania, M. Bellaveglia, E. Chiadroni, A. Cianchi, G. Costa, A. Curcio, D. Di Giovenale, G. Di Pirro, M. Ferrario, et al. The flame laser at sparc_lab. *Nuclear Instruments and Methods in Physics Research Section A: Accelerators, Spectrometers, Detectors and Associated Equipment*, 909:452–455, 2018.

[45] R. Bonifacio, C. Pellegrini, and L. Narducci. Collective instabilities and high-gain regime in a free electron laser. *Optics Communications*, 50(6):373–378, 1984. doi: 10.1016/0030-4018(84)90105-6. URL https://www.scopus.com/inward/record.uri?eid=2-s2.0-0021464515&doi=10.1016%2f0030-4018%2884%2990105-6&partnerID=40&md5=c8d6dea8f852eaaf64c5728521113235. cited By 1238.

[46] R. Bossart, P. Brown, J. Mourier, I. V. Syratchev, and L. Tanner. High-power microwave pulse compression of klystrons by phase-modulation of high-q storage cavities. Jun 2004. URL https://cds.cern.ch/record/741401.

[47] E. Brentegani, M. P. Anania, S. Atzeni, A. Biagioni, E. Chiadroni, M. Croia, M. Ferrario, F. Filippi, A. Marocchino, A. Mostacci, et al. Numerical studies on capillary discharges as focusing elements for electron beams. *Nuclear Instruments and Methods in Physics Research Section A: Accelerators, Spectrometers, Detectors and Associated Equipment*, 909:404–407, 2018.

[48] P. Brown and I. Syratchev. 3 ghz barrel open cavity (boc) rf pulse compressor for ctf3. In *2004 IEEE MTT-S International Microwave Symposium Digest*

(IEEE Cat. No.04CH37535), volume 2, pages 1009–1012 Vol.2, June 2004. doi: 10.1109/MWSYM.2004.1339152.

[49] *CAS - CERN Accelerator School : 5th Advanced Accelerator Physics Course. "High-field electron linacs,"*, Geneva, 1995. CERN, CERN. doi: 10.5170/CERN-1995-006. URL http://cds.cern.ch/record/254747.

[50] T. Charles et al. The Compact Linear Collider (CLIC) - 2018 Summary Report. 2/2018, 12 2018. doi: 10.23731/CYRM-2018-002.

[51] E. Chiadroni, D. Alesini, M. Anania, A. Bacci, M. Bellaveglia, A. Biagioni, F. Bisesto, F. Cardelli, G. Castorina, A. Cianchi, M. Croia, A. Gallo, D. Di Giovenale, G. Di Pirro, M. Ferrario, F. Filippi, A. Giribono, A. Marocchino, A. Mostacci, M. Petrarca, L. Piersanti, S. Pioli, R. Pompili, S. Romeo, A. Rossi, J. Scifo, V. Shpakov, B. Spataro, A. Stella, C. Vaccarezza, and F. Villa. Beam manipulation for resonant plasma wakefield acceleration. *Nuclear Instruments and Methods in Physics Research Section A: Accelerators, Spectrometers, Detectors and Associated Equipment*, 865:139 – 143, 2017. ISSN 0168-9002. doi: https://doi.org/10.1016/j.nima.2017.01.017. URL http://www.sciencedirect.com/science/article/pii/S0168900217300165. Physics and Applications of High Brightness Beams 2016.

[52] E. Chiadroni et al. Overview of plasma lens experiments and recent results. these proceedings.

[53] A. Cianchi, D. Alesini, M. Anania, F. Biagioni, F. Bisesto, E. Chiadroni, A. Curcio, M. Ferrario, F. Filippi, A. Ghigo, et al. Conceptual design of electron beam diagnostics for high brightness plasma accelerator. *Nuclear Instruments and Methods in Physics Research Section A: Accelerators, Spectrometers, Detectors and Associated Equipment*, 909:350–354, 2018.

[54] R. Collin. *Foundations for Microwave Engineering*. IEEE Press Series on Electromagnetic Wave Theory. Wiley, 2001. ISBN 9780780360310. URL https://www.wiley.com/en-us/Foundations+for+Microwave+Engineering%2C+2nd+Edition-p-9780780360310.

[55] M. Croia, D. Alesini, F. Cardelli, M. Diomede, M. Ferrario, A. Giribono, S. Romeo, C. Vaccarezza, and A. Vannozzi. High gradient ultra-high brightness C-band photoinjector optimization. In *Journal of Physics: Conference Series*, volume 1596, 2020. doi: 10.1088/1742-6596/1596/1/012031.

[56] Y. Y. Danilov and M. I. Petelin. On the theory of a microwave pulse compressor based on a barrel-shaped cavity. *Radiophysics and Quantum Electronics*, 42 (10):859–863, Oct 1999. ISSN 1573-9120. doi: 10.1007/BF02677098. URL https://doi.org/10.1007/BF02677098.

[57] G. D'Auria et al. The CompactLight Design Study Project. In *Proc. 10th International Particle Accelerator Conference (IPAC'19), Melbourne, Australia, 19-24 May 2019*, number 10 in International Particle Accelerator Conference, pages 1756–1759, Geneva, Switzerland, Jun.

2019. JACoW Publishing. ISBN 978-3-95450-208-0. doi: doi:10.18429/JACoW-IPAC2019-TUPRB032. URL http://jacow.org/ipac2019/papers/tuprb032.pdf. https://doi.org/10.18429/JACoW-IPAC2019-TUPRB032.

[58] M. D. David Alesini. Layout and optimization of the linac rf system. *WP4 progress meeting*. URL https://indico.cern.ch/event/967809/.

[59] R. Dei-Cas, P. Balleyguier, A. Bertin, M. Beuve, A. Binet, A. Bloquet, R. Bois, C. Bonetti, J. De Brion, F. Coçu, J. Di Crescenzo, P. Fourdin, J. Fréhaut, M. Guilloud, G. Haouat, A. Herscovici, D. Iracane, R. Joly, S. Joly, J. Jouys, J. Laget, C. Laspalles, H. Leboutet, J. Marmouget, D. Masseron, Y. De Penquer, Y. Pranal, J. Sigaud, S. Striby, D. Véron, J. Vouillarmet, J. Aucouturier, A. Bensussan, M. Simon, A. Dubrovin, G. Le Meur, J. Adam, and A. Héron. Status report on the low-frequency photoinjector and on the infrared fel experiment (elsa). *Nuclear Instruments and Methods in Physics Research Section A: Accelerators, Spectrometers, Detectors and Associated Equipment*, 296(1):209–216, 1990. ISSN 0168-9002. doi: https://doi.org/10.1016/0168-9002(90)91211-S. URL https://www.sciencedirect.com/science/article/pii/016890029091211S.

[60] M. Diomede, D. Alesini, M. Bellaveglia, B. Buonomo, F. Cardelli, N. C. Lasheras, E. Chiadroni, G. Di Pirro, M. Ferrario, A. Gallo, et al. Preliminary rf design of an x-band linac for the eupraxia@ sparc_lab project. *Nuclear Instruments and Methods in Physics Research Section A: Accelerators, Spectrometers, Detectors and Associated Equipment*, 909:243–246, 2018.

[61] V. Dolgashev, L. Faillace, B. Spataro, and R. Bonifazi. Innovative compact braze-free accelerating cavity. *Journal of Instrumentation*, 13(09):P09017–P09017, sep 2018. doi: 10.1088/1748-0221/13/09/p09017. URL https://doi.org/10.1088%2F1748-0221%2F13%2F09%2Fp09017.

[62] V. A. Dolgashev. Progress on high-gradient structures. *AIP Conference Proceedings*, 1507(1):76–84, 2012. doi: 10.1063/1.4773679. URL https://aip.scitation.org/doi/abs/10.1063/1.4773679.

[63] D. H. Dowell, K. J. Davis, K. D. Friddell, E. L. Tyson, C. A. Lancaster, L. Milliman, R. E. Rodenburg, T. Aas, M. Bemes, S. Z. Bethel, P. E. Johnson, K. Murphy, C. Whelen, G. E. Busch, and D. K. Remelius. First operation of a photocathode radio frequency gun injector at high duty factor. *Applied Physics Letters*, 63(15):2035–2037, 1993. doi: 10.1063/1.110583. URL https://doi.org/10.1063/1.110583.

[64] D. H. Dowell, E. Jongewaard, C. Limborg-Deprey, J. Schmerge, Z. Li, L. Xiao, J. Wang, J. Lewandowski, and A. Vlieks. Results of the slac lcls gun high-power rf tests. In *2007 IEEE Particle Accelerator Conference (PAC)*, pages 1296–1298, 2007. doi: 10.1109/PAC.2007.4441061.

[65] M. El Khaldi, J. Bonis, A. Camara, L. Garolfi, and A. Gonnin. Electromagnetic, Thermal, and Structural Analysis of a THOMX RF Gun Using ANSYS. In *7th*

International Particle Accelerator Conference, page THPOW002, 2016. doi: 10.18429/JACoW-IPAC2016-THPOW002.

[66] V. K. et al. Particle and Accelerator Physics at the VEPP-4M Collider. 2014. URL `https://accelconf.web.cern.ch/rupac2014/papers/thcb01.pdf`.

[67] Z. Farkas. Sled: A method of doubling slac's energy. pages 576–583, 01 1974.

[68] Z. Farkas. Binary Peak Power Multiplier and Its Application to Linear Accelerator Design. *IEEE Trans. Microwave Theor. Tech.*, 34:1036, 1986. doi: 10.1109/TMTT.1986.1133493.

[69] M. Ferrario. Low emittance photoinjectors, 2001.

[70] M. Ferrario, D. Alesini, A. Bacci, M. Bellaveglia, R. Boni, M. Boscolo, M. Castellano, E. Chiadroni, A. Cianchi, L. Cultrera, G. Di Pirro, L. Ficcadenti, D. Filippetto, V. Fusco, A. Gallo, G. Gatti, L. Giannessi, M. Labat, B. Marchetti, C. Marrelli, M. Migliorati, A. Mostacci, E. Pace, L. Palumbo, M. Quattromini, C. Ronsivalle, A. R. Rossi, J. Rosenzweig, L. Serafini, M. Serluca, B. Spataro, C. Vaccarezza, and C. Vicario. Experimental demonstration of emittance compensation with velocity bunching. *Phys. Rev. Lett.*, 104:054801, Feb 2010. doi: 10.1103/PhysRevLett.104.054801. URL `https://link.aps.org/doi/10.1103/PhysRevLett.104.054801`.

[71] M. Ferrario, D. Alesini, M. Anania, M. Artioli, A. Bacci, S. Bartocci, R. Bedogni, M. Bellaveglia, A. Biagioni, F. Bisesto, F. Brandi, E. Brentegani, F. Broggi, B. Buonomo, P. Campana, G. Campogiani, C. Cannaos, S. Cantarella, F. Cardelli, M. Carpanese, M. Castellano, G. Castorina, N. C. Lasheras, E. Chiadroni, A. Cianchi, R. Cimino, F. Ciocci, D. Cirrincione, G. Cirrone, R. Clementi, M. Coreno, R. Corsini, M. Croia, A. Curcio, G. Costa, C. Curatolo, G. Cuttone, S. Dabagov, G. Dattoli, G. Auria, I. Debrot, M. Diomede, A. Drago, D. DiÂ Giovenale, S. D. Mitri, G. DiÂ Pirro, A. Esposito, M. Faiferri, L. Ficcadenti, F. Filippi, O. Frasciello, A. Gallo, A. Ghigo, L. Giannessi, A. Giribono, L. Gizzi, A. Grudiev, S. Guiducci, P. Koester, S. Incremona, F. Iungo, L. Labate, A. Latina, S. Licciardi, V. Lollo, S. Lupi, R. Manca, A. Marcelli, M. Marini, A. Marocchino, M. Marongiu, V. Martinelli, C. Masciovecchio, C. Mastino, A. Michelotti, C. Milardi, V. Minicozzi, F. Mira, S. Morante, A. Most. Eupraxiasparclab design study towards a compact fel facility at lnf. *Nuclear Instruments and Methods in Physics Research Section A: Accelerators, Spectrometers, Detectors and Associated Equipment*, 909:134 – 138, 2018. ISSN 0168-9002. doi: https://doi.org/10.1016/j.nima.2018.01.094. URL `http://www.sciencedirect.com/science/article/pii/S0168900218301414`. 3rd European Advanced Accelerator Concepts workshop (EAAC2017).

[72] A. Fiebig and R. Hohbach. Study of Peak Power Doublers with Spherical Resonators. *IEEE Trans. Nucl. Sci.*, 30:3563–3565, 1983. doi: 10.1109/TNS.1983.4336726.

[73] A. Fiebig and C. Schieblich. A sled type pulse compressor with rectangular pulse shape. In *Conf. Proc.*, volume 900612, pages 937–939, 1990.

[74] H. Franz, O. Leupold, R. Röhlsberger, S. Roth, O. Seeck, J. Spengler, J. Strempfer, M. Tischer, J. Viefhaus, E. Weckert, et al. Technical report: Petra iii: Desy's new high brilliance third generation synchrotron radiation source. *Synchrotron Radiation News*, 19(6):25–29, 2006.

[75] A. V. Gaponov-Grekhov and V. L. Granatstein. *Applications of high-power microwaves*. Artech House Publishers, 1994.

[76] G. Geschonke and A. Ghigo. Ctf3 design report. Technical Report CERN-PS-2002-008-RF. CTF3-NOTE-2002-047. LNF-2002-008-IR, CERN, Geneva, May 2002. URL `https://cds.cern.ch/record/559331`. revised version number 1 submitted on 2002-06-19 12:11:29.

[77] A. Giribono, A. Bacci, E. Chiadroni, A. Cianchi, M. Croia, M. Ferrario, A. Marocchino, V. Petrillo, R. Pompili, S. Romeo, et al. Eupraxia@ sparc_lab: the high-brightness rf photo-injector layout proposal. *Nuclear Instruments and Methods in Physics Research Section A: Accelerators, Spectrometers, Detectors and Associated Equipment*, 909:282–285, 2018.

[78] A. Giribono, A. Bacci, E. Chiadroni, A. Cianchi, M. Croia, M. Ferrario, A. Marocchino, V. Petrillo, R. Pompili, S. Romeo, M. R. Conti, A. Rossi, and C. Vaccarezza. Eupraxia@sparc_lab: The high-brightness rf photo-injector layout proposal. 909:282–285, 2018.

[79] M. Groover. *Fundamentals of Modern Manufacturing: Materials, Processes and Systems, 7e Enhanced eText with Abridged Print Companion*. Wiley, 2019. ISBN 9781119592792. URL `https://www.wiley.com/en-us/Fundamentals+of+Modern+Manufacturing%3A+Materials%2C+Processes%2C+and+Systems%2C+7th+Edition-p-9781119475217`.

[80] A. Grudiev, S. Calatroni, and W. Wuensch. New local field quantity describing the high gradient limit of accelerating structures. *Physical Review Special Topics - Accelerators and Beams*, 2009. doi: 10.1103/physrevstab.12.102001.

[81] R. Haensel. European synchrotron radiation facility (esrf). *Review of Scientific Instruments*, 63(1):1571–1572, 1992. doi: 10.1063/1.1143024. URL `https://doi.org/10.1063/1.1143024`.

[82] J. Han, H.-S. Kang, and I. Ko. Status of the PAL-XFEL Project. *Conf. Proc. C*, 1205201:1735–1737, 2012.

[83] J.-H. Han. Production of a sub-10 fs electron beam with 10^7 electrons. *Phys. Rev. ST Accel. Beams*, 14:050101, May 2011. doi: 10.1103/PhysRevSTAB.14.050101. URL `https://link.aps.org/doi/10.1103/PhysRevSTAB.14.050101`.

[84] J. B. Hastings, F. M. Rudakov, D. H. Dowell, J. F. Schmerge, J. D. Cardoza, J. M. Castro, S. M. Gierman, H. Loos, and P. M. Weber. Ultrafast time-resolved electron diffraction with megavolt electron beams. *Applied Physics Letters*, 89(18):184109, 2006. doi: 10.1063/1.2372697. URL `https://doi.org/10.1063/1.2372697`.

[85] J. Hirshfield, S. V. Kuzikov, M. I. Petelin, and V. G. Pavelyev. Whispering gallery pulse compressor. *AIP Conference Proceedings*, 737(1):637–642, 2004. doi: 10.1063/1.1842602. URL https://aip.scitation.org/doi/abs/10.1063/1.1842602.

[86] T. Inagaki, C. Kondo, H. Maesaka, T. Ohshima, Y. Otake, T. Sakurai, K. Shirasawa, and T. Shintake. High-gradient *c*-band linac for a compact x-ray free-electron laser facility. *Phys. Rev. ST Accel. Beams*, 17: 080702, Aug 2014. doi: 10.1103/PhysRevSTAB.17.080702. URL https://link.aps.org/doi/10.1103/PhysRevSTAB.17.080702.

[87] D. A. Jaroszynski, R. Prazeres, F. Glotin, and J. M. Ortega. Two-color free-electron laser operation. *Phys. Rev. Lett.*, 72:2387–2390, Apr 1994. doi: 10.1103/PhysRevLett.72.2387. URL https://link.aps.org/doi/10.1103/PhysRevLett.72.2387.

[88] E. JENSEN. *FABRICATION AND TESTING OF RF STRUCTURES*, pages 130–154. doi: 10.1142/9789812703064_0005. URL https://www.worldscientific.com/doi/abs/10.1142/9789812703064_0005.

[89] N. Kazakov. *Diffusion bonding of materials*.

[90] V. Kiselev, V. Anachin, O. Anchugov, A. Bondar, A. Dubrovin, P. Durnov, Y. Gluhovchenko, E. Gorniker, A. Kalinin, S. Karnaev, G. Y. Kezerashvili, E. Kuper, G. Kurkin, Y. Levashow, B. Levichev, A. Medvedko, L. Mironenko, S. Mishnev, N. Y. Muchnoi, A. P. Onuchin, S. Petrov, V. M. Petrov, V. V. Petrov, V. Popov, I. V. Protopopov, Y. Pupkov, D. Shatilov, E. Simonov, A. N. Skrinsky, V. Smaluk, N. I. Zinevich, E. I. Zinin, M. Formin, A. Naumenkov, V. Nenukov, S. Nikitin, Y. A. Tikhonov, and G. Tumaikin. VEPP-4M Collider: Status and Plans. 1998. URL https://cds.cern.ch/record/858636.

[91] I. Ko, H.-S. Kang, H. Heo, C. Kim, G. Kim, C.-K. Min, H. Yang, S. Baek, H.-J. Choi, G. Mun, B. Park, Y. Suh, D. Shin, J. Hu, J. Hong, S. Jung, S.-H. Kim, K. Kim, D. Na, and K. Lee. Construction and commissioning of pal-xfel facility. *Applied Sciences*, 7:479, 05 2017. doi: 10.3390/app7050479.

[92] G. Kube. Specific diagnostics needs for different machines. 2009. doi: 10.5170/CERN-2009-005.1. URL https://cds.cern.ch/record/1213273.

[93] R. Kuroda, H. Toyokawa, M. Yasumoto, H. Ikeura-Sekiguchi, M. Koike, K. Yamada, T. Yanagida, T. Nakajyo, F. Sakai, and K. Mori. Quasi-monochromatic hard x-ray source via laser compton scattering and its application. *Nuclear Instruments and Methods in Physics Research Section A: Accelerators, Spectrometers, Detectors and Associated Equipment*, 637(1, Supplement):S183–S186, 2011. ISSN 0168-9002. doi: https://doi.org/10.1016/j.nima.2010.04.001. URL https://www.sciencedirect.com/science/article/pii/S016890021000793X. The International Workshop on Ultrashort Electron and Photon Beams: Techniques and Applications.

[94] P. M. Lapostolle and A. L. Septier. Linear accelerators. 1970.

[95] R. Li, C. Tang, Y. Du, W. Huang, Q. Du, J. Shi, L. Yan, and X. Wang. Experimental demonstration of high quality mev ultrafast electron diffraction. *Review of Scientific Instruments*, 80(8):083303, 2009. doi: 10.1063/1.3194047. URL https://doi.org/10.1063/1.3194047.

[96] Z. Li, W. Fang, Q. Gu, and Z. Zhao. Rf design of a c-band compact spherical rf pulse compressor for sxfel. *Nuclear Instruments and Methods in Physics Research Section A: Accelerators, Spectrometers, Detectors and Associated Equipment*, 863:7 – 14, 2017. ISSN 0168-9002. doi: https://doi.org/10.1016/j.nima.2017.05.017. URL http://www.sciencedirect.com/science/article/pii/S0168900217305569.

[97] Z. Li, W. Fang, A. Grudiev, Q. Gu, and Z. Zhao. A New Spherical Pulse Compressor Working with Degenerated "Whispering Gallery" Mode. In *Proc. 29th Linear Accelerator Conference (LINAC'18), Beijing, China, 16-21 September 2018*, number 29 in Linear Accelerator Conference, pages 928–930, Geneva, Switzerland, Jan. 2019. JACoW Publishing. ISBN 978-3-95450-194-6. doi: doi:10.18429/JACoW-LINAC2018-THPO109. URL http://jacow.org/linac2018/papers/thpo109.pdf. https://doi.org/10.18429/JACoW-LINAC2018-THPO109.

[98] D. Liu, Y. He, B. Zhang, and L. Shen. Formulation of toupin–mindlin strain gradient theory in prolate and oblate spheroidal coordinates. *European Journal of Mechanics - A/Solids*, 49:227–241, 2015. ISSN 0997-7538. doi: https://doi.org/10.1016/j.euromechsol.2014.07.015. URL https://www.sciencedirect.com/science/article/pii/S0997753814001119.

[99] A. Lunin, V. Yakovlev, and A. Grudiev. Analytical solutions for transient and steady state beam loading in arbitrary traveling wave accelerating structures. *Phys. Rev. ST Accel. Beams*, 14:052001, May 2011. doi: 10.1103/PhysRevSTAB.14.052001. URL https://link.aps.org/doi/10.1103/PhysRevSTAB.14.052001.

[100] A. Mak, P. Salén, V. Goryashko, and J. Clarke. Science requirements and performance specification forthe compactlight x-ray free-electron laser, 2019.

[101] A. Marocchino, E. Chiadroni, M. Ferrario, F. Mira, and A. Rossi. Design of high brightness plasma wakefield acceleration experiment at SPARC LAB test facility with particle-in-cell simulations. *Nuclear Instruments and Methods in Physics Research Section A: Accelerators, Spectrometers, Detectors and Associated Equipment*, 909:408 – 413, 2018. ISSN 0168-9002. doi: https://doi.org/10.1016/j.nima.2018.02.068. URL http://www.sciencedirect.com/science/article/pii/S0168900218302225. 3rd European Advanced Accelerator Concepts workshop (EAAC2017).

[102] A. Marocchino, E. Chiadroni, M. Ferrario, F. Mira, and A. R. Rossi. Design of high brightness plasma wakefield acceleration experiment at sparc_lab test facility with particle-in-cell simulations. *Nuclear Instruments and Methods in Physics Research Section A: Accelerators, Spectrometers, Detectors and Associated Equipment*, 909:408–413, 2018.

[103] M. Marongiu, M. Castellano, E. Chiadroni, A. Cianchi, G. Franzini, A. Giribono, A. Mostacci, L. Palumbo, V. Shpakov, A. Stella, et al. Energy measurements by means of transition radiation in novel linacs. *Nuclear Instruments and Methods in Physics Research Section A: Accelerators, Spectrometers, Detectors and Associated Equipment*, 909:355–358, 2018.

[104] C. Milardi, D. Alesini, M. E. Biagini, R. Boni, M. Boscolo, F. Bossi, B. Buonomo, A. Clozza, G. Delle Monache, T. Demma, E. Di Pasquale, G. Di Pirro, A. Drago, A. Gallo, A. Ghigo, S. Guiducci, C. Ligi, F. Marcellini, G. Mazzitelli, F. Murtas, L. Pellegrino, and C. I. R. K. T. O. L. R. U. P. U. I. P. I. R. S. /Frascati /Novosibirsk, IYF /CERN /INFN. Crab waist collision at dafne. *ICFA Beam Dynamics Newsletter*.

[105] R. H. Miller. Comparison of Standing Wave and Traveling Wave Structures. In *13th International Linear Accelerator Conference*, pages TU2–4, 1986.

[106] C. Milne, T. Schietinger, M. Aiba, A. Alarcon, J. Alex, A. Anghel, V. Arsov, C. Beard, P. Beaud, S. Bettoni, and et al. Swissfel: The swiss x-ray free electron laser. *Applied Sciences*, 7(7):720, Jul 2017. ISSN 2076-3417. doi: 10.3390/app7070720. URL `http://dx.doi.org/10.3390/app7070720`.

[107] P. Musumeci, J. T. Moody, C. M. Scoby, M. S. Gutierrez, H. A. Bender, and N. S. Wilcox. High quality single shot diffraction patterns using ultrashort megaelectron volt electron beams from a radio frequency photoinjector. *Review of Scientific Instruments*, 81(1):013306, 2010. doi: 10.1063/1.3292683. URL `https://doi.org/10.1063/1.3292683`.

[108] C. Nantista, S. Tantawi, and V. Dolgashev. Low-field accelerator structure couplers and design techniques. *Physical Review Special Topics - Accelerators and Beams*, 2004. ISSN 10984402. doi: 10.1103/PhysRevSTAB.7.072001.

[109] C. D. Nantista. Radiofrequency pulse compression for linear accelerators. 1995.

[110] R. B. Neal. Design of linear electron accelerators with beam loading. *Journal of Applied Physics*, 29(7):1019–1024, 1958.

[111] Y. Ohnishi, T. Abe, T. Adachi, K. Akai, Y. Arimoto, K. Ebihara, K. Egawa, J. Flanagan, H. Fukuma, Y. Funakoshi, K. Furukawa, T. Furuya, N. Iida, H. Iinuma, H. Ikeda, T. Ishibashi, M. Iwasaki, T. Kageyama, S. Kamada, T. Kamitani, K.-i. Kanazawa, M. Kikuchi, H. Koiso, M. Masuzawa, T. Mimashi, T. Miura, T. Mori, A. Morita, T. Nakamura, K. Nakanishi, H. Nakayama, M. Nishiwaki, Y. Ogawa, K. Ohmi, N. Ohuchi, K. Oide, T. Oki, M. Ono, M. Satoh, K. Shibata, M. Suetake, Y. Suetsugu, R. Sugahara, H. Sugimoto, T. Suwada, M. Tawada, M. Tobiyama, N. Tokuda, K. Tsuchiya, H. Yamaoka, Y. Yano, M. Yoshida, S.-i. Yoshimoto, D. Zhou, and Z. Zong. Accelerator design at SuperKEKB. *Progress of Theoretical and Experimental Physics*, 2013(3), 03 2013. ISSN 2050-3911. doi: 10.1093/ptep/pts083. URL `https://doi.org/10.1093/ptep/pts083`. 03A011.

[112] P. G. O'Shea, S. C. Bender, B. E. Carlsten, J. W. Early, D. W. Feldman, R. B. Feldman, W. J. Johnson, A. H. Lumpkin, R. L. Sheffield, R. W. Springer, W. E. Stein, and L. M. Young. Performance of the photoinjector accelerator for the los alamos free-electron laser. URL https://www.osti.gov/biblio/5740304.

[113] D. T. Palmer. The next generation photoinjector. 1998.

[114] V. Petrillo, A. Bacci, E. Chiadroni, G. Dattoli, M. Ferrario, A. Giribono, A. Marocchino, A. Petralia, M. R. Conti, A. Rossi, et al. Free electron laser in the water window with plasma driven electron beams. *Nuclear Instruments and Methods in Physics Research Section A: Accelerators, Spectrometers, Detectors and Associated Equipment*, 909:303–308, 2018.

[115] J. G. Power. Overview of photoinjectors. *AIP Conference Proceedings*, 1299 (1):20–28, 2010. doi: 10.1063/1.3520316. URL https://aip.scitation.org/doi/abs/10.1063/1.3520316.

[116] T. Rao and D. H. Dowell. An engineering guide to photoinjectors, 2014.

[117] T. Raubenheimer. Overview of nlc/jlc collaboration. 08 2003. doi: 10.2172/815261.

[118] S. Romeo, E. Chiadroni, M. Croia, M. Ferrario, A. Giribono, A. Marocchino, F. Mira, R. Pompili, A. Rossi, and C. Vaccarezza. Simulation design for forthcoming high quality plasma wakefield acceleration experiment in linear regime at SPARC LAB. *Nuclear Instruments and Methods in Physics Research Section A: Accelerators, Spectrometers, Detectors and Associated Equipment*, 909:71 – 75, 2018. ISSN 0168-9002. doi: https://doi.org/10.1016/j.nima.2018.02.081. URL http://www.sciencedirect.com/science/article/pii/S0168900218302614. 3rd European Advanced Accelerator Concepts workshop (EAAC2017).

[119] A. Rossi, V. Petrillo, A. Bacci, E. Chiadroni, A. Cianchi, M. Ferrario, A. Giribono, A. Marocchino, M. R. Conti, L. Serafini, et al. Plasma boosted electron beams for driving free electron lasers. *Nuclear Instruments and Methods in Physics Research Section A: Accelerators, Spectrometers, Detectors and Associated Equipment*, 909:54–57, 2018.

[120] M. Satoh et al. Commissioning Status of SuperKEKB Injector Linac. In *Proc. of International Particle Accelerator Conference (IPAC'16), Busan, Korea, May 8-13, 2016*, number 7 in International Particle Accelerator Conference, pages 4152–4154, Geneva, Switzerland, June 2016. JACoW. ISBN 978-3-95450-147-2. doi: doi:10.18429/JACoW-IPAC2016-THPOY027. URL http://jacow.org/ipac2016/papers/thpoy027.pdf. doi:10.18429/JACoW-IPAC2016-THPOY027.

[121] S. Schreiber. Performance status of the rf-gun based injector of the tesla test facility linac. 2000. URL https://accelconf.web.cern.ch/e00/PAPERS/THOAF203.pdf.

[122] J. Schwinger. On the classical radiation of accelerated electrons. *Phys. Rev.*, 75:1912–1925, Jun 1949. doi: 10.1103/PhysRev.75.1912. URL `https://link.aps.org/doi/10.1103/PhysRev.75.1912`.

[123] L. Serafini and M. Ferrario. Velocity bunching in photo-injectors. In *AIP conference proceedings*, volume 581, pages 87–106. American Institute of Physics, 2001.

[124] G. Shenoy and D. Moncton. An overview of the advanced photon source. *Nuclear Instruments and Methods in Physics Research Section A: Accelerators, Spectrometers, Detectors and Associated Equipment*, 266(1):38 – 43, 1988. ISSN 0168-9002. doi: https://doi.org/10.1016/0168-9002(88)90356-7. URL `http://www.sciencedirect.com/science/article/pii/0168900288903567`.

[125] D. Shin. Study of electron bunching in vacuum devices: Electron gun, linear accelerator. 2015.

[126] G. Shu, M. Hou, S. Pei, N. Song, J. Zhang, and F. Zhao. Design, Fabrication and Cold Test of a C-Band Barrel Open Cavity Pulse Compressor. In *8th International Particle Accelerator Conference*, page THPIK046, 2017. doi: 10.18429/JACoW-IPAC2017-THPIK046.

[127] I. V. Syrachev. The progress of x-band "Open" cavity rf pulse compression systems. In *Proceeding of 4-th European Particle Accelerator Conference, London, UK*, pages 375–379, 1994.

[128] C. Travier. Review of microwave guns. *Part. Accel.*, 36:33–74, 1991.

[129] W. Utsumi, K.-I. Funakoshi, S. Urakawa, M. Yamakata, K. Tsuji, H. Konishi, and O. Shimomura. Spring-8 beamlines for high pressure science with multi-anvil apparatus. *The Review of High Pressure Science and Technology*, 7: 1484–1486, 1998.

[130] C. Vaccarezza, D. Alesini, A. Bacci, A. Cianchi, E. Chiadroni, M. Croia, M. Diomede, M. Ferrario, A. Gallo, A. Giribono, A. Latina, A. Marocchino, V. Petrillo, R. Pompili, S. Romeo, M. R. Conti, A. Rossi, L. Serafini, and B. Spataro. EUPRAXIA@SPARC_LAB: Beam dynamics studies for the X-band Linac. *Nuclear Instruments and Methods in Physics Research Section A: Accelerators, Spectrometers, Detectors and Associated Equipment*, 909:314 – 317, 2018. ISSN 0168-9002. doi: https://doi.org/10.1016/j.nima.2018.01.100. URL `http://www.sciencedirect.com/science/article/pii/S0168900218301475`. 3rd European Advanced Accelerator Concepts workshop (EAAC2017).

[131] C. Vaccarezza, D. Alesini, A. Bacci, A. Cianchi, E. Chiadroni, M. Croia, M. Diomede, M. Ferrario, A. Gallo, A. Giribono, et al. Eupraxia@ sparc_lab: Beam dynamics studies for the x-band linac. *Nuclear Instruments and Methods in Physics Research Section A: Accelerators, Spectrometers, Detectors and Associated Equipment*, 909:314–317, 2018.

[132] I. A. Vainstein. *Open Cavities and Open Waveguides*. Moscow: Sov. Radio. (in russian), 1966.

[133] A. L. Vikharev, A. M. Gorbachev, O. A. Ivanov, M. A. Lobaev, V. A. Isaev, S. V. Kuzikov, V. A. Koldanov, and J. L. Hirshfield. Plasma switch for x-band active sled-ii rf pulse compressor. *AIP Conference Proceedings*, 737(1):790–796, 2004. doi: 10.1063/1.1842624. URL https://aip.scitation.org/doi/abs/10.1063/1.1842624.

[134] A. L. Vikharev, A. M. Gorbachev, O. A. Ivanov, V. A. Isaev, S. V. Kuzikov, M. A. Lobaev, J. L. Hirshfield, S. H. Gold, and A. K. Kinkead. High power active x-band pulse compressor using plasma switches. *Phys. Rev. ST Accel. Beams*, 12:062003, Jun 2009. doi: 10.1103/PhysRevSTAB.12.062003. URL https://link.aps.org/doi/10.1103/PhysRevSTAB.12.062003.

[135] F. Villa, A. Cianchi, M. Coreno, S. Dabagov, A. Marcelli, V. Minicozzi, S. Morante, and F. Stellato. Design study of a photon beamline for a soft x-ray fel driven by high gradient acceleration at eupraxia@ sparc_lab. *Nuclear Instruments and Methods in Physics Research Section A: Accelerators, Spectrometers, Detectors and Associated Equipment*, 909:294–297, 2018.

[136] P. Walker et al. HORIZON 2020 EuPRAXIA Design Study. In *Proc. of International Particle Accelerator Conference (IPAC'17), Copenhagen, Denmark, 14 - 19 May, 2017*, number 8 in International Particle Accelerator Conference, pages 1265–1268, Geneva, Switzerland, May 2017. JACoW. ISBN 978-3-95450-182-3. doi: https://doi.org/10.18429/JACoW-IPAC2017-TUOBB3. URL http://jacow.org/ipac2017/papers/tuobb3.pdf. https://doi.org/10.18429/JACoW-IPAC2017-TUOBB3.

[137] P. Wang, H. Zha, I. Syratchev, J. Shi, and H. Chen. rf design of a pulse compressor with correction cavity chain for klystron-based compact linear collider. *Phys. Rev. Accel. Beams*, 20:112001, Nov 2017. doi: 10.1103/PhysRevAccelBeams.20.112001. URL https://link.aps.org/doi/10.1103/PhysRevAccelBeams.20.112001.

[138] T. P. Wangler. Introduction to linear accelerators. *Los Alamos Nat'l Lab report*, 1993.

[139] T. P. Wangler. *RF linear accelerators*. Wiley-VCH, Germany, 2008. ISBN 978-3-527-40680-7. URL http://inis.iaea.org/search/search.aspx?orig_q=RN:39102345. PARTICLE ACCELERATORS.

[140] S. website. . URL http://xfel.riken.jp/eng/.

[141] S. website. . URL https://www.psi.ch/de/swissfel.

[142] M. White, N. Arnold, and W. Berg. Construction, commissioning and operational experience of the advanced photon source (aps) linear accelerator. Technical report, Argonne National Lab., 1996.

[143] H. Wiedemann. *Particle Accelerator Physics I: Vol. 1-*. Springer. ISBN 9783540646716. URL https://books.google.it/books?id=nTJOUx5oQQ0C.

[144] I. H. Wilson. Cavity construction techniques. 1992. doi: 10.5170/CERN-1992-003.375. URL https://cds.cern.ch/record/245417.

[145] P. B. Wilson, Z. Farkas, and R. D. Ruth. Sled ii: A new method of rf pulse compression. Technical report, Stanford Linear Accelerator Center, Menlo Park, CA (USA), 1990.

[146] B. J. Woolley. *High Power X-band RF Test Stand Development and High Power Testing of the CLIC Crab Cavity*. PhD thesis, Lancaster U., 2015. URL http://eprints.lancs.ac.uk/76926.

[147] W. Wuensch. High-gradient breakdown in normal-conducting rf cavities. Technical report, 2002.

[148] M. Yabashi, H. Tanaka, and T. Ishikawa. Overview of the sacla facility. *Journal of Synchrotron Radiation*, 22, 05 2015. doi: 10.1107/S1600577515004658.

[149] J. Yang, K. Kan, N. Naruse, Y. Yoshida, K. Tanimura, and J. Urakawa. 100-femtosecond mev electron source for ultrafast electron diffraction. *Radiation Physics and Chemistry*, 78(12):1106–1111, 2009.

[150] R. Zennaro, M. Bopp, A. Citterio, R. Reiser, and T. Stapf. C-band rf pulse compressor for swissfel. In *Proceedings, 4th International Particle Accelerator Conference (IPAC 2013): Shanghai, China, May 12-17, 2013*, page WEPFI059, 2013. URL http://JACoW.org/IPAC2013/papers/wepfi059.pdf.

[151] R. Zennaro, J. Alex, A. Citterio, and J.-Y. Raguin. Measurements and high power test of the first c-band accelerating structure for swissfel. 09 2014.